Magnetic Flux Transport on the Sun

Dissertation
zur Erlangung des Doktorgrades
der Mathematisch-Naturwissenschaftlichen Fakultäten
der Georg-August-Universität zu Göttingen

vorgelegt von
Ingo Jens Baumann
aus Lauf an der Pegnitz

Göttingen 2005

Bibliografische Information Der Deutschen Bibliothek

Die Deutsche Bibliothek verzeichnet diese Publikation in der Deutschen Nationalbibliografie; detaillierte bibliografische Daten sind im Internet über `http://dnb.ddb.de` abrufbar.

D7
Referent: Prof. Dr. Franz Kneer
Korreferent: Prof. Dr. Sami K. Solanki
Tag der mündlichen Prüfung: 21. März 2005

Copyright © Copernicus GmbH 2005

ISBN 3-936586-36-5

Copernicus GmbH, Katlenburg-Lindau
Druck: Schaltungsdienst Lange, Berlin

Printed in Germany

FÜR MEINE ELTERN

Contents

Summary **1**

1 Introduction **3**

2 Basics of MHD **7**
2.1 Magnetohydrodynamic approximation 7
2.2 Induction equation and frozen field lines 8
2.3 MHD equations 10
2.4 Force-free fields 11

3 The surface flux transport code **13**
3.1 Decomposition in spherical harmonics 13
3.2 Treatment of new sources 17

4 Evolution of the large-scale magnetic field on the solar surface: A parameter study **19**
4.1 Introduction 19
4.2 Flux transport model 20
4.2.1 Transport equation 20
4.2.2 Transport parameters 20
4.2.3 Numerical treatment 21
4.2.4 Simulating solar cycles 21
4.2.5 Initial field configuration 22
4.3 Reference cycle model 23
4.3.1 Reference cycle parameters 23
4.3.2 Unsigned magnetic flux 25
4.3.3 Polar fields 26
4.4 Parameter study: results and discussion 29
4.4.1 Magnetic diffusivity 29
4.4.2 Poleward meridional flow 29
4.4.3 Differential rotation 32
4.4.4 Activity level 32
4.4.5 Overlap time of successive cycles 35
4.4.6 Cycle length 37
4.4.7 Size distribution of BMRs 38
4.4.8 Tilt angle 40

4.4.9 Emergence latitudes . . . 42
4.4.10 Asymmetric activity cycles . . . 43
4.4.11 Shape of activity profile . . . 46
4.4.12 Phase relation between the activity cycle and polar fields . . . 46
4.5 Conclusion . . . 48

5 A necessary extension of the surface flux transport model 49
5.1 Introduction . . . 49
5.2 Decay modes of a poloidal field in a spherical shell . . . 50
5.3 Extension of the surface flux transport model . . . 53
5.4 Applications . . . 55
5.4.1 Cycles of varying strength . . . 55
5.4.2 Polar reversal times . . . 56
5.4.3 Comparison with observations . . . 56
5.5 Conclusion . . . 59

6 Modelling the open magnetic flux from the Greenwich sunspot group record 61
6.1 Introduction . . . 61
6.2 The source surface model . . . 62
6.3 Results for synthetic data . . . 64
6.3.1 Influence of η on the open flux . . . 64
6.3.2 Time-dependent source surface . . . 66
6.3.3 High- and low-latitude open flux . . . 67
6.3.4 Variation of $R_{\rm ss}$ . . . 67
6.4 Dipole tilt angle . . . 71
6.5 The current-sheet source surface model . . . 72
6.6 Simulation of the open flux on the basis of the RGO sunspot data . . . 77
6.6.1 Method of transforming the sunspot record into an active region sequence . . . 77
6.6.2 Surface magnetic field . . . 79
6.6.3 Comparison with IMF observations . . . 80
6.7 Conclusion . . . 82

7 On the size distribution of sunspot groups in the Greenwich sunspot record 1874-1976 85
7.1 Introduction . . . 85
7.2 Dataset and analysis procedure . . . 86
7.3 Results for RGO spot group areas . . . 88
7.3.1 Umbrae . . . 88
7.3.2 Total areas . . . 89
7.3.3 Total area of single spots . . . 90
7.3.4 Umbral areas of single spots . . . 90
7.4 Modeling the snapshot distribution . . . 92
7.4.1 Model description . . . 92
7.4.2 Results from the model . . . 92
7.5 Conclusion . . . 96

8 Comments and outlook **97**

Bibliography **98**

Acknowledgements **105**

Curriculum Vitae **107**

Summary

In this thesis, numerical simulations on a spherical surface were carried out in order to study the evolution of the photospheric large-scale magnetic field due to magnetic flux transport processes.

- A numerical code has been developed in order to simulate the time evolution of the global magnetic field under the influence of supergranular diffusion, differential rotation and a meridional flow.
- An extensive parameter study has been done in order to investigate the influence of a variety of solar cycle parameters on the solar magnetic field with focus on the Sun's total surface field and the polar field.
- The existing flux transport model has been extended by a term parametrising radial decay processes. The necessity of this extension follows from comparing numerical simulations with observations. The extended model improves especially the modelling of long-term trends, like the polar field evolution.
- The Sun's surface magnetic field has been simulated with the extended surface flux transport model using the RGO/USAF sunspot data. The simulation is in good agreement with the observed solar magnetic field.
- A source surface model is used in order to calculate the Sun's open magnetic flux. Attempts to model the historic IMF record on the basis of the Greenwich sunspot database are unsatisfying because of insufficient open flux resulting from the low latitudes during activity maximum. Adding the open flux contribution of ephemeral regions improves the results.
- The size distribution of sunspot groups has been investigated. Both, the maximum areas and the instantaneous areas are found to be log-normally distributed. This result is confirmed by a simple decay model.

1 Introduction

Activity phenomena on the Sun are known since a long time. The most striking indicators of solar activity are sunspots, visible in brightness. Since the beginning of the last century it is known that the dark spots on the solar disk are related to strong magnetic field concentrations. The cyclic behaviour of solar activity with a period of about 11 years was first remarked by Heinrich Schwabe (1844). Later it was found that the magnetic field reverses after 11 years and thus the duration of the magnetic activity cycle is 22 years (Hale et al. 1919). It is believed that the driver of the polarity reversal of the solar magnetic field is the solar dynamo. Up to now, many theories in explaining the solar dynamo mechanism have been developed, however, there are still a lot of unresolved questions (Ossendrijver 2003).

Dark sunspots and bright faculae can be observed in continuum light on the photosphere (Fig. 1.1 a). The extended areas where spots, faculae, plages and filaments occur are called active regions. Typically a well-developed active region has a single sunspot group. The part of an active region outside sunspots, the facular region, usually contains a mean magnetic field of a few hundred Gauss, resulting in a total magnetic flux of 10^{22} Mx for a medium size region (Priest 1982). The magnetic structure of an active region can be derived from magnetograms (Fig. 1.1 b). Magnetic regions on the Sun have in general bipolar structure, although the individual polarities can be fragmented. The orientation of the magnetic polarities of the same activity complex follows on average Hales' polarity law (Hale and Nicholson 1925). In the layer above the photosphere, the chromosphere, solar activity becomes evident in plages. These are chromospheric faculae and are best observed in the Ca II K-line.

Besides the active regions with large magnetic flux concentrations, there's a magnetic background network, called the quiet Sun network. This network is formed by granular motions which confine the flux concentrations along the downflow boundaries of the photospheric granules.

The solar cycle

The emergence of sunspots appears to happen in a systematic way in two latitudinal bands. At the beginning of a cycle, sunspots emerge at mid-latitudes around $\pm 35^\circ$ and at the end of a cycle sunspots emerge closer to the equator at around $\pm 5^\circ$. A time-latitude plot representing this cyclic decline of the emergence latitudes is commonly denoted as *butterfly diagram* (Fig. 1.2).

The daily sunspot presence is recorded in the *sunspot number* R. The daily *Boulder Sunspot Number*, is computed by the NOAA Space Environment Center using a formula

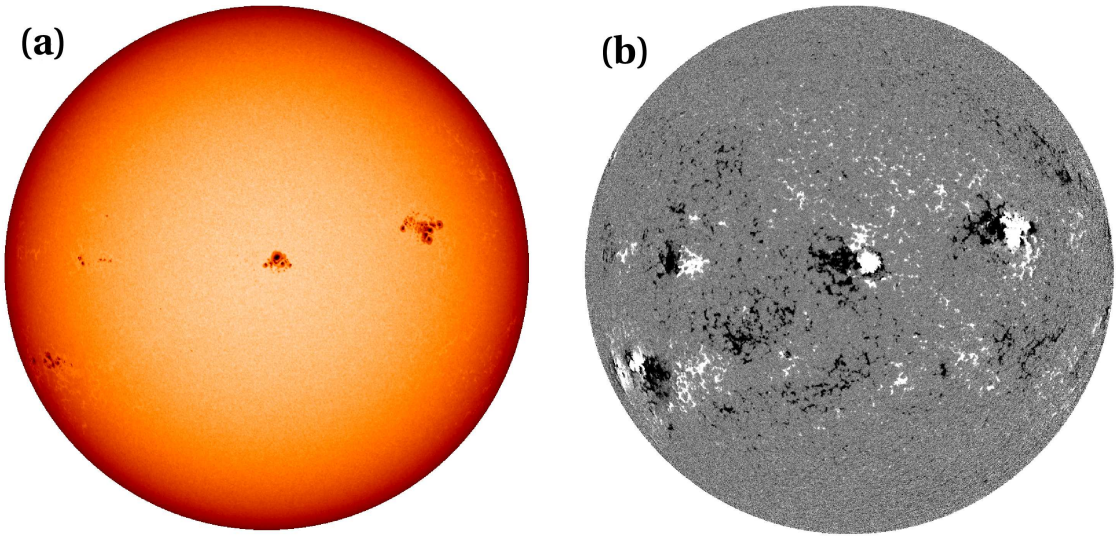

Figure 1.1: (a) White light image of the Sun showing several sunspot groups and (b) the corresponding magnetogram. Source: Solar and Heliospheric Observatory, SOHO.

devised by Rudolph Wolf in 1848

$$R = k(10g + s)\,, \tag{1.1}$$

where g is the number of sunspot groups on the solar disk, s is the total number of individual spots in all the groups and k is a variable scaling factor (usually < 1) that accounts for observing conditions and the type of telescope (binoculars, space telescopes, etc.). Today, scientists combine data from lots of observatories – each with its own k factor – to arrive at a daily value. It was found only recently by extrapolating the sunspot number back in time from radiocarbon concentrations, that the Sun is currently in a period of unusual high activity (Solanki et al. 2004).

Active stars

The Sun is our nearest star and thus its activity phenomena are known much better than on other stars. Activity phenomena similar to the ones observed on the Sun are also expected to occur on other stars. Most of the stars appear only as point-like light sources which makes it difficult or even impossible to observe starspots directly. The most common technique used for detecting starspots is Doppler-Imaging. Brightness inhomogeneities on the stellar disk, i.e. dark spots, deform the spectral line profiles of the star as they rotate with the star. From a time-series of this deformed line profiles one can conclude about the brightness distribution on the stellar surface.

All spotted stars are chromospherically active and show strong Ca II H and K emission lines. Another characteristic of active stars is the strong X-ray emission of their coronae.

At present star spots have been indirectly detected on several tens of stars. In general, stellar spots are much bigger than sunspots and emerge mainly in the polar regions, in contrast to the Sun, where the spots emerge in an activity band around the equator.

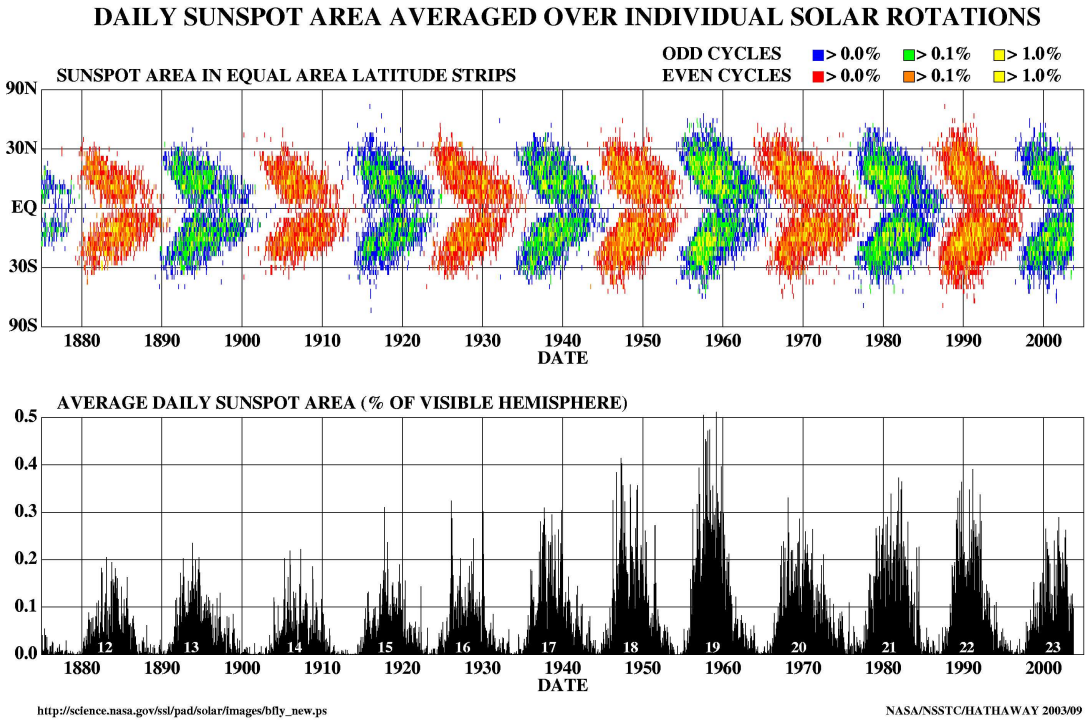

Figure 1.2: *Top:* Sunspot butterfly diagram. *Bottom:* Average daily sunspot area. Source: D. Hathaway, NASA, Marshall Space Flight Center.

The Sun-Earth connection

The Sun's total irradiance has been found to vary slightly with the solar cycle ($\sim 0.1\%$). Although the dark sunspots block solar irradiance partly, the isochronic bright faculae and plages enhance irradiance leading to a net effect of increased solar irradiance during high solar activity (Foukal and Lean 1988). The Sun is by far the Earth's main energy supplier and thus any change in the solar radiative output affects the Earth's energy budget.

Understanding the possible influence of solar activity on the Earth's climate remains an interesting and important scientific task. So far, the main mechanisms which have been suggested are that the Sun's varying total irradiance changes the total energy input into the Earth's atmosphere. The Sun‘s varying ultraviolet emissions affect the production of ozone in the Earth‘s atmosphere, thus leading to a change of the ozone layer. A weak solar wind and heliospheric magnetic field, as is the case during solar minimum, enables galactic cosmic rays to enter the Earth‘s atmosphere which may enhance the formation of low-altitude clouds. The solar wind affects the electrical properties of the Earth‘s upper atmosphere which affects in a second step the lower atmospheric layers. The significance of each of these mechanisms is yet unknown.

About this work

The main goal of this PhD project was to investigate theoretically the evolution of the global solar magnetic field. To this aim a 2-dimensional numerical code has been devel-

oped in order to simulate the evolution of the surface magnetic field as it evolves owing to photospheric transport processes.

A brief introduction to magnetohydrodynamics which forms the theoretical background of this work is presented in Chap. 2. The numerical treatment of the surface flux transport code is given in Chap. 3. The influence of a variety of solar cycle parameters on the Sun's large-scale magnetic field is discussed in Chap. 4. In Chap. 5 we present an extension of the flux transport model describing the surface magnetic field evolution by including radial flux decay. In Chap. 6 we model the magnetic field of the historic Sun on the basis of sunspot observations and discuss the relation of the surface magnetic field and the Sun's open flux. The work on the size distribution of sunspot groups grew out of the use of RGO sunspot areas in Chap. 6 and is presented in Chap. 7.

2 Basics of MHD

2.1 Magnetohydrodynamic approximation

MHD (Magnetohydrodynamics) describes the dynamics of a macroscopic plasma. The MHD equations are based on two assumptions. The plasma motion is assumed to be nonrelativistic, i.e. plasma velocities are small compared to the speed of light

$$\frac{v}{c} \ll 1\,, \tag{2.1}$$

and the plasma is supposed to be quasineutral. The Maxwell equations in the cgs system are

$$\nabla \cdot \mathbf{B} = 0 \tag{2.2}$$

$$\nabla \cdot \mathbf{E} = 4\pi\rho \tag{2.3}$$

$$\nabla \times \mathbf{E} = -\frac{1}{c}\frac{\partial \mathbf{B}}{\partial t} \tag{2.4}$$

$$\nabla \times \mathbf{B} = \frac{4\pi}{c}\mathbf{j} + \frac{1}{c}\frac{\partial \mathbf{E}}{\partial t}\,, \tag{2.5}$$

where $\mathbf{E}$ is the electric field, $\mathbf{B}$ is the magnetic field, $\mathbf{j}$ is the current density and ρ is the charge density. When $\mathbf{E}$ and $\mathbf{B}$ are given in a coordinate system K, then their transformation into a coordinate system K' moving with a velocity $\mathbf{v}$ relative to K is

$$\mathbf{E}' = \mathbf{E} + \frac{1}{c}\mathbf{v} \times \mathbf{B} \tag{2.6}$$

$$\mathbf{B}' = \mathbf{B} - \frac{1}{c}\mathbf{v} \times \mathbf{E} \tag{2.7}$$

Let L be a characteristic length scale and τ a characteristic time where $\mathbf{E}$ and $\mathbf{B}$ change. Then the spatial and temporal derivatives can be estimated as

$$|\nabla \times \mathbf{B}| \approx \frac{B}{L} \tag{2.8}$$

$$\left|\frac{\partial \mathbf{E}}{\partial t}\right| \approx \frac{E}{\tau} \tag{2.9}$$

It follows from

$$\frac{L/\tau}{c} \approx \frac{v_{\mathrm{ph}}}{c} \ll 1 \tag{2.10}$$

that the phase velocities $v_{\rm ph}$ of the field quantities are small compared to the speed of light. This implies that no electromagnetic waves occur in this approximation.

From Eq. (2.4) we can estimate

$$\frac{E}{L} \approx \frac{B}{c\,\tau}\,. \tag{2.11}$$

Combining Eq. (2.11) with Eq. (2.10) one obtains

$$\frac{E}{B} \approx \frac{L/\tau}{c} \ll 1\,. \tag{2.12}$$

This is especially true for the photospheric plasma, where the spatial and temporal scales exceed the Debye length $\lambda_D = (kT/8\pi n_e e^2)^{1/2}$ and the inverse plasma frequency $\omega_p^{-1} = (m_e/4\pi e^2 n_e)^{1/2}$, respectively, by many orders of magnitude. Typical photospheric values are $T = 5 \cdot 10^3$ K and $n_e = 10^{14}$ cm^{-3} leading to $\lambda_D = 10^{-4}$ cm and $\omega_p^{-1} = 10^{-11}$ s. The

displacement current in the Maxwell equation Eq. (2.5) is negligible because

$$\frac{\left|\dot{\mathbf{E}}/c\right|}{|\nabla \times \mathbf{B}|} \approx \frac{E/\tau}{cB/L} \approx \frac{E}{B}\frac{L}{c\tau} \approx \left(\frac{E}{B}\right)^2 \ll 1\,. \tag{2.13}$$

With the MHD-approximations above, Eq. (2.5) becomes

$$\nabla \times \mathbf{B} \;=\; \frac{4\pi}{c}\mathbf{j}\,, \tag{2.14}$$

and the transformation Eq. (2.7)

$$\mathbf{B}' \;=\; \mathbf{B}\,. \tag{2.15}$$

The transformation of the electric field (Eq. 2.6) remains unchanged.

Equations (2.14) and (2.15) imply the transformation of the current density

$$\mathbf{j}' \;=\; \mathbf{j}\,. \tag{2.16}$$

2.2 Induction equation and frozen field lines

If the motion of the plasma in the frame of references is described by the velocity field $\mathbf{v}$ and the conductivity of the plasma is σ then Ohm's law becomes the form

$$\mathbf{j} = \sigma\mathbf{E}' = \sigma(\mathbf{E} + \frac{\mathbf{1}}{\mathbf{c}}\mathbf{v} \times \mathbf{B})\,. \tag{2.17}$$

Combining Eq. (2.4) with the curl of Eqs. (2.5) and (2.17) leads to the induction equation

$$\frac{\partial \mathbf{B}}{\partial t} = \underbrace{\nabla \times (\mathbf{v} \times \mathbf{B})}_{\text{induction}} - \underbrace{\nabla \times (\eta_m\, \nabla \times \mathbf{B})}_{\text{diffusion}} \tag{2.18}$$

where the magnetic diffusivity is defined as

$$\eta_m = \frac{c^2}{4\pi\sigma}\,. \tag{2.19}$$

The first term on the right side of (2.18) is the induction term and the second term is the diffusion term. The induction term describes the temporal evolution of the magnetic field due to the plasma motion, while the diffusion term describes the ohmic decay due to the finite conductivity in the plasma. The ratio of the induction term to the diffusion term in Eq. (2.18) is expressed by the dimensionless magnetic Reynolds number

$$R_m = \frac{vL}{\eta_m}\,. \tag{2.20}$$

The quantities v and L are characteristic values of the flow velocity and the length scale. For the solar plasma one has to deal with very big Reynolds numbers $R_m \gg 1$. Typical values for granular convection cells on the solar photosphere are $L \approx 10^8\,\mathrm{cm}$, $v \approx 10^5\,\mathrm{cm\ s^{-1}}$ and a magnetic diffusivity of $\eta_m \approx 10^7\,\mathrm{cm^2\ s^{-1}}$ leading to a Reynolds number of $R_m \approx 10^6$.

For large Reynolds numbers, as is the case for the solar plasma, the flow term in Eq. (2.18) dominates. Neglecting the diffusion term on the right side of Eq. (2.18) and integrating over an arbitrary surface moving with the local fluid velocity $\mathbf{v}$ yields

$$\int \frac{\partial \mathbf{B}}{\partial t}\cdot d\,\mathbf{S} = \int \nabla\times(\mathbf{v}\times\mathbf{B})\cdot d\,\mathbf{S} = \oint (\mathbf{v}\times\mathbf{B})\cdot d\,\mathbf{l}\,, \tag{2.21}$$

where on the right side Stokes's theorem has been applied. It can be shown (e.g. Tannenbaum 1967) that for a surface moving with velocity $\mathbf{v}$ follows

$$\frac{d}{dt}\left(\int \mathbf{B}\cdot d\,\mathbf{S}\right) = \int \frac{\partial \mathbf{B}}{\partial t}\cdot d\,\mathbf{S} + \oint \mathbf{B}\cdot(\mathbf{v}\times d\,\mathbf{l}) \tag{2.22}$$

and thus together with Eq. (2.21) and the vector identity $(\mathbf{A}\times\mathbf{B})\cdot\mathbf{C} = -\mathbf{B}\cdot(\mathbf{A}\times\mathbf{C})$

$$\frac{d}{dt}\int \mathbf{B}\cdot d\,\mathbf{S} = 0\,. \tag{2.23}$$

The flux passing through a moving surface stays constant, meaning that the field lines move along with the fluid. The field lines behave as if being *frozen* in the fluid. This result is known as *Alfvén's theorem*.

2.3 MHD equations

The basic set of equations of ideal MHD results from combining the hydrodynamic continuity equation, the Navier-Stokes equation, the Maxwell equations in the MHD approximation and the thermodynamic energy equation.

The continuity equation expresses the conservation of mass

$$\frac{\partial \rho}{\partial t} + \nabla \cdot (\rho \, \mathbf{v}) = 0 \,, \tag{2.24}$$

where ρ is the density and $\mathbf{v}$ is the flow velocity.
The equation of motion is given by the Navier-Stokes equation extended by the Lorentz force

$$\rho \frac{\partial \, \mathbf{v}}{\partial t} + \rho \, (\mathbf{v} \cdot \nabla)\mathbf{v} = -\nabla P + \frac{1}{c} \, \mathbf{j} \times \mathbf{B} + \rho \, \mathbf{g} + \rho \, \nu \, \triangle \mathbf{v} \,. \tag{2.25}$$

Here, ν is the kinematic viscosity, $\mathbf{g}$ is the gravitational acceleration and $\mathbf{B}$ the magnetic field.

The equation of state describes the dependence of the gas pressure P from the density ρ and the temperature T. For the Sun's interior a reasonable approximation is the perfect gas law (Stix 1989)

$$P = \frac{\rho \, \mathcal{R} \, T}{\mu} \,. \tag{2.26}$$

$\mathcal{R}$ is the gas constant and μ is the mean molecular weight.

The set of equations is completed by the induction equation (Eq. 2.18) and the energy equation

$$\rho T \frac{ds}{dt} = -\mathcal{L} \,. \tag{2.27}$$

In Eq. (2.27) s is the entropy per unit mass and $\mathcal{L}$ is the energy loss function which can be written as

$$\mathcal{L} = \nabla \cdot \mathbf{q} + L_r - \frac{j^2}{\sigma} - H \,, \tag{2.28}$$

where $\mathbf{q}$ is the heat flux due to particle conduction, L_r is the net radiation, j^2/σ is the ohmic dissipation and H represents the sum of all other heating sources. For an ideal polytropic gas Eq. (2.28) can be written as

$$\mathcal{L} = -\frac{\rho^\gamma}{(\gamma - 1)} \frac{d}{dt} \left(\frac{P}{\rho^\gamma} \right) \tag{2.29}$$

with the adiabatic exponent γ. For a detailed derivation of the MHD equations see for example Kippenhahn and Möllenhoff (1975) or Priest (1982).

Substituting $\mathbf{j}$ in Eq. (2.25) by Eq. (2.14) and using the vector identity

$$(\nabla \times \mathbf{B}) \times \mathbf{B} = (\mathbf{B} \cdot \nabla) \, \mathbf{B} - \nabla \left(\frac{B^2}{2} \right) \tag{2.30}$$

one gets an additional pressure term resulting from the magnetic field called the magnetic pressure

$$P_m = \frac{B^2}{8\pi} \,. \tag{2.31}$$

2.4 Force-free fields

In the magnetostatic case, i.e. when all quantities are time independent and no flows are present, equation (2.25) simplifies to

$$\nabla P = \frac{1}{4\pi}(\nabla \times \mathbf{B}) \times \mathbf{B} + \rho\,\mathbf{g}\,. \tag{2.32}$$

The ratio of gas pressure to magnetic pressure is called the *plasma* β

$$\beta = \frac{P}{B^2/8\pi}\,. \tag{2.33}$$

For strong magnetic fields and a dilute plasma the plasma β is very small and the gas pressure as well as its gradient can be neglected. The weight of a dilute plasma can also be neglected. Thus Eq. (2.32) reduces to

$$(\nabla \times \mathbf{B}) \times \mathbf{B} = 0\,. \tag{2.34}$$

A magnetic field satisfying Eq. (2.34) is called *force-free*. An example where the force-free condition is applicable is the lower solar corona. Above the photosphere the plasma density diminishes exponentially, i.e. very rapidly, while the magnetic field decreases with a power-law (Schatten et al. 1969). This leads to a low plasma β in the solar corona and thus the force-free approximation can be applied.

Eq. (2.34) implies that the curl of the magnetic field and thus the current density is in the direction of the magnetic field

$$\nabla \times \mathbf{B} = \alpha\mathbf{B}\,, \tag{2.35}$$

where α is a scalar function of space. α cannot vary along a magnetic field line because of

$$\nabla \cdot (\alpha\mathbf{B}) = \mathbf{B} \cdot \nabla\alpha = 0\,. \tag{2.36}$$

A second class of solutions of Eq. (2.34) are *potential fields*. Potential fields describe the situation of current free plasmas

$$\nabla \times \mathbf{B} = 0\,. \tag{2.37}$$

From Eq. (2.37) it follows that the magnetic field can be represented by a scalar potential

$$\mathbf{B} = -\nabla\psi\,. \tag{2.38}$$

Because of the solenoidality of magnetic fields, Eq. (2.2), the scalar potential ψ has to satisfy the Laplace equation

$$\nabla^2\psi = 0\,. \tag{2.39}$$

The current-free approximation is often applied in the Sun's chromosphere and lower corona (Sakurai 1982). In the case that significant electrical currents are present in the solar atmosphere, the difference between potential field calculations and observed coronal structures yields information about the coronal currents (Altschuler 1974).

3 The surface flux transport code

Part of the thesis work was to develop a numerical code to solve the surface flux transport equation for the radial magnetic field component in spherical coordinates. The flux transport equation originates from the radial component of the induction equation (Eq. 2.18) under the assumption that the magnetic field is purely radial at the surface, i.e. $B_\theta(R_\odot, \theta, \phi) = B_\phi(R_\odot, \theta, \phi) = 0$

$$\begin{aligned} \frac{\partial B_r}{\partial t} &= -\omega(\theta)\frac{\partial B_r}{\partial \phi} - \frac{1}{R_\odot \sin(\theta)}\frac{\partial}{\partial \theta}\left[v(\theta) B_r \sin(\theta)\right] \\ &+ \frac{\eta_h}{R_\odot^2}\left[\frac{1}{\sin(\theta)}\frac{\partial}{\partial \theta}\left(\sin(\theta)\frac{\partial B_r}{\partial \theta}\right) + \frac{1}{\sin^2(\theta)}\frac{\partial^2 B_r}{\partial \phi^2}\right] \\ &- D_r(\eta) + S(\theta, \phi, t)\,. \end{aligned} \tag{3.1}$$

In Eq. (3.1), $\omega(\theta)$ is the differential rotation, $v(\theta)$ the meridional flow and η_h the magnetic surface diffusivity. $S(\theta, \phi, t)$ is an additional source term describing the emergence of new magnetic flux. $D_r(\eta)$ is an additional decay term parametrising the radial loss of magnetic flux (specified in detail in Chap. 5).

In the following, the numerical method of the surface flux transport code (SFTC) is described.

3.1 Decomposition in spherical harmonics

Since we wish to solve the flux transport equation (Eq. 3.1) on the surface of a sphere, it is advantageous to express the radial magnetic field component in terms of spherical harmonics

$$B_r(\theta, \phi, t) = \sum_{l=0}^{\infty} \sum_{m=-l}^{l} a_{lm}(t)\, Y_{lm}(\theta, \phi)\,. \tag{3.2}$$

The spherical harmonics are defined as

$$Y_{lm}(\theta, \phi) = \sqrt{\frac{2l+1}{4\pi}\frac{(l-m)!}{(l+m)!}}\; P_l^m(\cos(\theta))\; e^{im\phi}\,, \tag{3.3}$$

where $P_l^m(\cos(\theta))$ are the associated Legendre polynomials of order m and degree l. The coefficients in (3.2) are given by

$$a_{lm}(t) = \int_0^{2\pi} \int_{-1}^{1} B_r(\theta, \phi, t)\; Y_{lm}^*(\theta, \phi)\; d\phi\; d(\cos(\theta))\,. \tag{3.4}$$

The asterisk in Eq. (3.4) denotes the complex conjugate. The decomposition of the magnetic field in the spherical transport equation into spherical harmonics simplifies the diffusion term because the spherical harmonics are eigenfunctions of the diffusion operator

$$\triangle_h \, Y_{lm}(\theta,\phi) = -l \, (l+1) \, Y_{lm}(\theta,\phi) \tag{3.5}$$

where $-l(l+1)$ are the respective eigenvalues. $\triangle_h$ is the angular part of the Laplace operator. Eq. (3.1) transforms with the decomposition Eq. (3.2) into a system of first-order differential equations where the spherical Laplacian is replaced by the eigenvalues Eq. (3.5). Inserting Eqs. (3.2)$-$ (3.5) in Eq. (3.1) leads to

$$\begin{aligned}
\sum_{l=0}^{\infty}\sum_{m=-l}^{l} \dot{a}_{lm}(t)\, Y_{lm}(\theta,\phi) \;=\; & \underbrace{-\omega(\theta)\sum_{l=0}^{\infty}\sum_{m=-l}^{l} a_{lm}(t)\,\frac{\partial\, Y_{lm}(\theta,\phi)}{\partial\phi}}_{\text{differential rotation term}} \\
& \underbrace{-\sum_{l=0}^{\infty}\sum_{m=-l}^{l}\frac{1}{R_\odot \sin(\theta)}\,\frac{\partial}{\partial\theta}\Big[v(\theta)\,\sin(\theta)\, a_{lm}(t)\, Y_{lm}(\theta,\phi)\Big]}_{\text{meridional flow term}} \\
& \underbrace{-\sum_{l=0}^{\infty}\sum_{m=-l}^{l}\eta_h\,\frac{l(l+1)}{R_\odot^2}\, a_{lm}(t)\, Y_{lm}(\theta,\phi)}_{\text{diffusion term}} \\
& \underbrace{-\sum_{l=0}^{\infty}\sum_{m=-l}^{l}\frac{a_{lm}(t)}{\tau_l}\, Y_{lm}(\theta,\phi)}_{\text{global decay term}} \\
& \underbrace{+\sum_{l=0}^{\infty}\sum_{m=-l}^{l} s_{lm}(t)\, Y_{lm}(\theta,\phi)}_{\text{newly emerging sources}}
\end{aligned} \tag{3.6}$$

In the global decay term in Eq. (3.6), τ_l are the individual decay times derived from the decay modes in a spherical shell (see Chap. 5 for details). Newly emerging bipolar magnetic regions are decomposed in its harmonic components, s_{lm}, which add then to the coefficients of the total surface field, $a_{lm}(t)$.

The task is now to determine the coefficients $a_{lm}(t)$. To this end, we use the orthogonality relation of the Legendre polynomials

$$\int_{-1}^{1} d(\cos(\theta))\, P_l^m(\cos(\theta)) P_{l'}^m(\cos(\theta)) = \frac{2}{2l+1}\frac{(l+m)!}{(l-m)!}\,\delta_{ll'} \tag{3.7}$$

and the relation

$$\int_0^{2\pi} e^{i(m-m')\phi}\, d\phi = 2\pi\delta_{mm'}\,. \tag{3.8}$$

Multiplying Eq. (3.6) with $Y^*_{l'm'}(\theta,\phi)$, where the asterisk denotes the complex conjugate, and integrating over $\int_{-1}^{1}\int_0^{2\pi} d(\cos(\theta))\,d\phi$ yields

$$\begin{aligned}
\dot{a}_{lm}(t) &= -\sum_{l'=0}^{\infty} 2\pi\, i\, m\, a_{l'm}(t)\, Q_{l'm}\, Q_{lm} \underbrace{\int_0^{\pi} \omega(\theta)\, P^m_{l'}(\cos(\theta)) P^m_l(\cos(\theta))\, \sin(\theta)\, d\theta}_{=:D_{l'lm}} \\
&\quad -\frac{2\pi}{R_\odot} Q_{lm} \sum_{l'=0}^{\infty} a_{l'm}(t)\, Q_{l'm} \int_0^{\pi} \Big[(l'+1)\, v(\theta)\, \cos(\theta) P^m_{l'}(\cos(\theta)) P^m_l(\cos(\theta)) \\
&\quad + \sin(\theta)\, \frac{\partial\, v(\theta)}{\partial\, \theta}\, P^m_{l'}(\cos(\theta)) P^m_l(\cos(\theta)) \\
&\quad -(l'+m)\, v(\theta)\, P^m_{l'-1}(\cos(\theta)) P^m_l(\cos(\theta))\Big]\, d\theta \\
&\quad -\eta_h\, \frac{l(l+1)}{R_\odot^2}\, a_{lm}(t) - \frac{a_{lm}(t)}{\tau_l} + s_{lm}(t)\,, \qquad (3.9)
\end{aligned}$$

where

$$Q_{lm} = \sqrt{\frac{2l+1}{4\pi}\frac{(l-m)!}{(l+m)!}}\,. \qquad (3.10)$$

In the following, we abbreviate the second integral in Eq. (3.9) with $C_{l'lm}$

$$\begin{aligned}
\dot{a}_{lm}(t) &= -2\pi\, Q_{lm} \sum_{l'=0}^{\infty} Q_{l'm} \left[\frac{1}{R_\odot}\, C_{l'lm} + i\, m\, D_{l'lm}\right] a_{l'm}(t) \\
&\quad -\frac{\eta_h}{R_\odot^2}\, l(l+1)\, a_{lm}(t) - \frac{a_{lm}(t)}{\tau_l} + s_{lm}(t)\,. \qquad (3.11)
\end{aligned}$$

If the meridional flow profile is antisymmetric with respect to the equator, some elements in Eq. (3.9) vanish

$$\begin{aligned}
C_{l'lm} &= \int_0^{\pi} \Big[(l'+1)\, \underbrace{v(\theta)\, \cos(\theta)}_{\text{sym.}} P^m_{l'}(\cos(\theta)) P^m_l(\cos(\theta)) \\
&\quad + \underbrace{\sin(\theta)\, \frac{\partial v(\theta)}{\partial\, \theta}}_{\text{sym.}}\, P^m_{l'}(\cos(\theta)) P^m_l(\cos(\theta)) \\
&\quad -(l'+m)\, \underbrace{v(\theta)}_{\text{antisym.}}\, P^m_{l'-1}(\cos(\theta)) P^m_l(\cos(\theta))\Big]\, d\theta \qquad (3.12)
\end{aligned}$$

$$D_{l'lm} = \int_0^{\pi} \underbrace{w(\theta)\, \sin(\theta)}_{\text{sym.}} P^m_{l'}(\cos(\theta)) P^m_l(\cos(\theta))\, d\theta\,. \qquad (3.13)$$

It can be easily seen that $C_{l'lm}$ and $D_{l'lm}$ vanish if $l + l'$ is odd. Another simplification in calculating the coefficients a_{lm} are the relations

$$C_{l'l(-m)} = \frac{(l'-m)!}{(l'+m)!}\frac{(l-m)!}{(l+m)!} C_{l'lm} \tag{3.14}$$

$$D_{l'l(-m)} = \frac{(l'-m)!}{(l'+m)!}\frac{(l-m)!}{(l+m)!} D_{l'lm}\,. \tag{3.15}$$

The non-zero integrals $C_{l'lm}$ and $D_{l'lm}$ are time-independent and thus have to be calculated only once. This is done using the composite Simpson rule (see for example Pozrikidis 1998).

The evolution of the magnetic field in Eq. (3.1) has been reduced to the solution of a system of

$$\sum_{n=0}^{l_{\max}+1} n = \frac{(l_{\max}+1)(l_{\max}+2)}{2} \tag{3.16}$$

first-order differential equations for the coefficients a_{lm}, where $l_{\max}$ is the truncation of the expansion in Eq. (3.2).

The contribution $s_{lm}(t)$ in Eq. (3.11) results from the appearance of new magnetic flux in the photosphere. The treatment of the new sources is described in Sect. 3.2. From Eq. (3.11) the remaining system of differential equations can be written as

$$\dot{a}_{lm} = M_{ll'm}\, a_{l'm}\,. \tag{3.17}$$

Only coefficients with the same value of m are coupled. The system Eq. (3.17) splits into parts when a suitable ordering of the equations is applied. We illustrate this ordering for the case $l_{\max} = 3$ where the above described symmetries are taken into account.

$$\begin{pmatrix} \dot{a}_{03} \\ \dot{a}_{13} \\ \dot{a}_{23} \\ \dot{a}_{33} \\ \hdashline \dot{a}_{02} \\ \dot{a}_{12} \\ \dot{a}_{22} \\ \hdashline \dot{a}_{01} \\ \dot{a}_{11} \\ \hdashline \dot{a}_{00} \end{pmatrix} = \begin{pmatrix} M_{003} & 0 & M_{023} & 0 & & & & & & \\ 0 & M_{113} & 0 & M_{133} & & & & & & \\ M_{203} & 0 & M_{223} & 0 & & & & & & \\ 0 & M_{313} & 0 & M_{333} & & & & & & \\ & & & & M_{002} & 0 & M_{022} & & & \\ & & & & 0 & M_{112} & 0 & & & \\ & & & & M_{202} & 0 & M_{222} & & & \\ & & & & & & & M_{001} & 0 & \\ & & & & & & & 0 & M_{111} & \\ & & & & & & & & & M_{000} \end{pmatrix} \begin{pmatrix} a_{03} \\ a_{13} \\ a_{23} \\ a_{33} \\ \hdashline a_{02} \\ a_{12} \\ a_{22} \\ \hdashline a_{01} \\ a_{11} \\ \hdashline a_{00} \end{pmatrix}$$

Every block in the above matrix corresponding to a certain value of m can be solved separately. The largest system of differential equations that is left consists of $2(l_{\max}+1)$ equations, where the factor 2 originates from the complex nature of the a_{lm}. The above system hast to be solved for the real and for the imaginary part of a_{lm}. Owing to the 0-components in (3.17), the number of equations reduces by a factor of two.

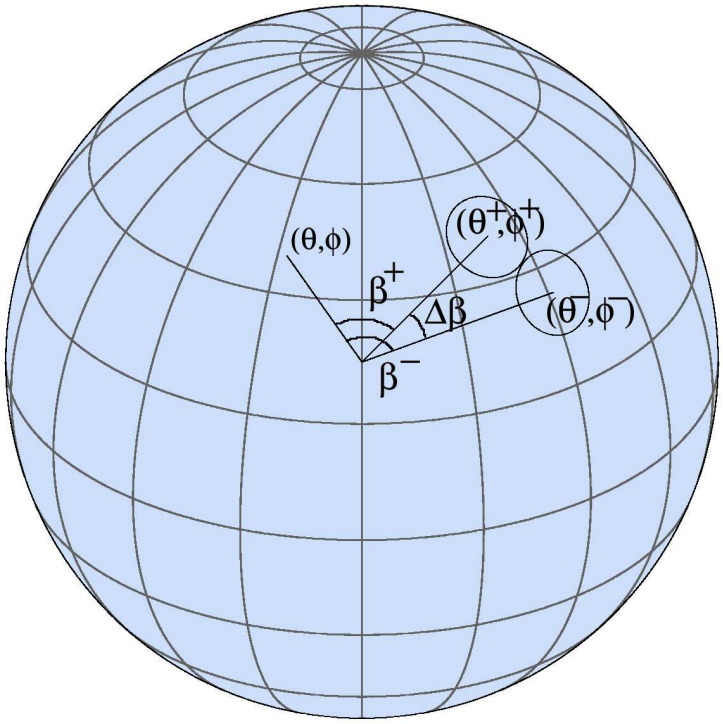

Figure 3.1: Illustration of the geometry of a bipolar magnetic region.

The individual block matrices in Eq. (3.17) are integrated using the fourth-order Runge-Kutta method. Here, the routine `rk4` from Numerical Recipes (Press et al. 1992) has been used.

3.2 Treatment of new sources

A new bipolar magnetic region (BMR) adds its magnetic flux to the surface field. The initial distribution of the corresponding radial field is written

$$\Delta B_r(R_\odot, \theta, \phi) = B_r^+(R_\odot, \theta, \phi) - B_r^-(R_\odot, \theta, \phi)\,, \tag{3.18}$$

where $B_r^\pm(R_\odot, \theta, \phi)$ are the unsigned distributions of the positive and negative polarity, respectively. Following van Ballegooijen et al. (1998), we represent a new BMR by two circular areas,

$$B_r^\pm(R_\odot, \theta, \phi) = B_{\max} \exp\left\{-\frac{2[1-\cos\beta_\pm(\theta,\phi)]}{\delta_{\rm in}^2}\right\}\,, \tag{3.19}$$

where $\beta_\pm(\theta, \phi)$ are the heliocentric angles between (θ, ϕ) and the central coordinates of the positive and negative polarity, $(\theta_\pm, \phi_\pm)$, respectively (Fig.3.1). For small values of $\beta_\pm$, Eq. (3.19) approximates a Gaussian. $\delta_{\rm in}$ is the initial angular width of the Gaussian, which is assumed to be proportional to the angular separation, $\Delta\beta$, of the centers of the two polarities: $\delta_{\rm in} = 0.4\,\Delta\beta$. The largest BMRs in our simulations have an angular separation

of $\Delta\beta = 10^\circ$. B_{max} is set to 250 G. Note that in this way the only free parameters describing a newborn BMR are $\theta_\pm$ and $\phi_\pm$. They determine the size and hence the total magnetic flux of the BMR. This description ensures that the fluxes in the positive and negative polarities of the newly emerged active region are always balanced.

Owing to the limited spatial resolution given by the numerical treatment very small BMRs cannot be resolved. We include the flux of such BMRs by considering them at a later stage of their development when they have already diffused to a width $\delta_0 = 4^\circ$. This treatment means that we assume such regions not to cancel with magnetic flux from other sources prior to this time. The final description of the two polarities in the flux contribution of a newly emerged BMR to the photospheric magnetic field is therefore given by

$$B_r^{\pm}(R_\odot, \theta, \phi) \;=\; B_{\text{max}} \left(\frac{\delta_{\text{in}}}{\delta_0}\right)^2 \exp\left\{-\frac{2[1-\cos\beta_\pm(\theta,\phi)]}{\delta_0^2}\right\}. \tag{3.20}$$

The contribution Eq. (3.18) of a new magnetic source is decomposed into spherical harmonics

$$\Delta B_r = \sum_{l=0}^{\infty} \sum_{m=-l}^{l} s_{lm}\, Y_{lm}(\theta,\phi)\,, \tag{3.21}$$

and the coefficients s_{lm} are added to the coefficients of the global magnetic field (Eq. 3.11) at the time of emergence of the BMR.

4 Evolution of the large-scale magnetic field on the solar surface: A parameter study

4.1 Introduction

The production and dissipation of the Sun's magnetic field is a complex process spanning the whole convection zone from the location of the solar dynamo at the tachocline near the base of the convection zone, over the transport of flux to the surface through buoyancy, to the evolution, dispersal and final cancellation of flux there. Of this combined problem we only consider the final part here, the evolution of the magnetic field at the Sun's surface.

New magnetic flux emerges at the solar photosphere in the form of bipolar magnetic regions (BMR) spanning a wide range of sizes (Harvey 1993). Statistical studies of the emergence patterns of BMRs show that new regions emerge at mid-latitudes at the beginning of a solar cycle and at low latitudes at the end of the cycle, leading to time-latitude plots that are commonly denoted as *butterfly diagrams*.

The dispersal of the magnetic flux of active regions was first considered by Leighton (1964) as a random-walk process of magnetic flux elements under the influence of the supergranular flow pattern. Flux transport models including differential rotation, diffusion (to account for this random walk) and a meridional flow have been developed by DeVore et al. (1985a), DeVore and Sheeley (1987) and Wang et al. (1989a) to describe the large-scale magnetic field by using observed source regions. More recently, flux transport models have been used to simulate the spreading of single bipoles (Mackay et al. 2002a, Wang et al. 2000b) and whole activity cycles (Schrijver 2001, Mackay et al. 2002b). The latter authors used synthetic records of active regions. In most of the simulations, the model parameters, i.e. diffusivity, meridional flow and differential rotation rate, have been adjusted in order to reproduce the observed surface magnetic field. Here we investigate the influence of the transport parameters and also of the parameters governing the magnetic flux sources, i.e. location and strength of the emerging BMRs, on the evolution of the surface magnetic field with particular emphasis on the resulting total unsigned magnetic flux and the polar flux. The aim of the investigation is to understand how various parameters affect the transport of magnetic flux at the solar surface. This has applications for reconstructions of solar magnetic flux distributions over many cycles and will provide a guide for similar studies of surface fields on other late-type stars.

This chapter is structured as follows. In Sect. 4.2 the flux transport model and its numerical realization is briefly described. In Sect. 4.3 the reference model (for the parameter

study) and the analysing techniques for the large-scale magnetic field are presented. In Sect. 4.4 a wide range of parameters governing the flux transport model and their influence on the photospheric large-scale magnetic field are discussed. Finally, in Sect. 4.5 the conclusions drawn from the performed study are summarized.

4.2 Flux transport model

4.2.1 Transport equation

The magnetic field concentrated in the network and in active region plages is only weakly inclined relative to the vertical (Solanki 1993, Martinez Pillet et al. 1997), so that the photospheric magnetic field can be taken as radially oriented (Wang and Sheeley 1992). Thus the flux transport of the large-scale magnetic field on the solar surface is described by the induction equation for the radial magnetic field component $B_r(\theta, \phi, t)$ (Leighton 1964, DeVore et al. 1984, Sheeley et al. 1985). In spherical coordinates we have

$$\begin{aligned} \frac{\partial B_r}{\partial t} &= -\omega(\theta)\frac{\partial B_r}{\partial \phi} - \frac{1}{R_\odot \sin\theta}\frac{\partial}{\partial \theta}\left(v(\theta) B_r \sin\theta\right) \\ &+ \frac{\eta_h}{R_\odot^2}\left[\frac{1}{\sin\theta}\frac{\partial}{\partial\theta}\left(\sin\theta\frac{\partial B_r}{\partial\theta}\right) + \frac{1}{\sin^2\theta}\frac{\partial^2 B_r}{\partial\phi^2}\right] \\ &+ S(\theta,\phi,t)\,. \end{aligned} \tag{4.1}$$

Here θ is the colatitude, ϕ is the longitude, $R_\odot$ is the solar radius, $\omega(\theta)$ is the angular velocity of the photospheric plasma, $v(\theta)$ is the meridional flow velocity, η_h is the effective diffusion coefficient associated with the non-stationary supergranular motions and $S(\theta, \phi, t)$ is a source term describing the emergence of new BMRs.

4.2.2 Transport parameters

One of the key ingredients in models of the type considered here is the diffusion coefficient. The model of Leighton (1964) required a diffusion coefficient in the range of $770 - 1540\,\mathrm{km^2\ s^{-1}}$ in order to reproduce the reversal of the polar fields during the sunspot cycle. Later, Mosher (1977) estimated the diffusion coefficient to lie in the range of $200 - 400\,\mathrm{km^2\ s^{-1}}$ by tracing the area covered by the magnetic field in active regions. This is roughly three times lower than the rate determined by Leighton. DeVore et al. (1985b) found the same range for the diffusion coefficient from simulations of the evolution of several observed active regions. Applying an average meridional flow with a flow amplitude of $10 \pm 3\,\mathrm{ms^{-1}}$ Wang et al. (1989b) constrained the diffusion coefficient to $600 \pm 200\,\mathrm{km^2\ s^{-1}}$ with the help of comparisons of numerical simulations with low-resolution, synoptic magnetic data. As the meridional flow speed they included is reasonable, the value of $600\,\mathrm{km^2\ s^{-1}}$ is adopted as reference value for the diffusion rate in the present study.

In the late 1970s first observational evidence for a poleward bulk flow was found. The highly concentrated polar fields during solar minimum supported the presence of a large-scale flow transporting magnetic field poleward. Duvall (1979) determined a flow amplitude of $20\,\mathrm{ms^{-1}}$ using observations of spectral line shifts. Topka et al. (1982) found an

amplitude of $10\,\mathrm{ms}^{-1}$. Due to possible interference between magnetic and Doppler signals large uncertainties remain Bogart (1987). For our simulations we use the meridional flow profile determined by Snodgrass and Dailey (1996) and Hathaway (1996),

$$v(\lambda) = \begin{cases} -v_0 \sin(\pi\lambda/\lambda_0) & : \quad \text{if} \quad |\lambda < \lambda_0| \\ 0 & : \quad \text{otherwise}\,, \end{cases} \tag{4.2}$$

where λ is the latitude in degrees ($\lambda \equiv \pi/2 - \theta$) and λ_0 is the latitude above which the meridional flow vanishes. We assume $v_0 = 11\,\mathrm{ms}^{-1}$ and $\lambda_0 = 75^\circ$ as the *standard case*. This profile was also used by van Ballegooijen et al. (1998).

For the latitude-dependent differential rotation we assume the empirical profile of Snodgrass (1983)

$$\omega(\theta) = 13.38 - 2.30\cos^2\theta - 1.62\cos^4\theta \tag{4.3}$$

in units of $\mathrm{deg\,day}^{-1}$.

4.2.3 Numerical treatment

For simulations of the photospheric magnetic field we have developed a two-dimensional code, denoted as SFTC (Surface Flux Transport Code, for details see Chap. 3). In order to integrate the flux transport equation (Eq. 4.1), the radial magnetic field is expressed in terms of spherical harmonics. This simplifies the numerical treatment of the diffusion term to the well-known eigenvalue problem of the spherical Laplace operator. Furthermore, this method gives direct information on the evolution of the magnetic multipoles, especially the dipole component.

We consider all spherical harmonics between $l = 0$ and $l = 63$ for the expansion (l is the order of the spherical harmonics). This corresponds to a spatial resolution element roughly of the size of a supergranule (≈ 30 Mm). A higher spatial resolution would not be consistent with the model of turbulent diffusion.

We validated our code by reproducing previous results in the literature, including the evolution of a single bipole (Wang et al. 2000b, Mackay et al. 2002b) and whole cycle simulations (Mackay et al. 2002b).

4.2.4 Simulating solar cycles

Simulations are carried out with a time step of one day. A weighted random number generator determines after every time step whether new BMRs appear on the model solar surface, where they appear, and which properties they have (see Sect. 4.3.1). The probability for a BMR to appear depends on the cycle parameters given as input and on the phase of the cycle. The new BMR described by Eqs. (3.18) and (3.20) is then added to the surface magnetic field and evolved according to Eq. (4.1).

The large-scale magnetic properties discussed below, i.e. the total unsigned photospheric field and the polar field strength, are taken as averages over the calculated cycles. Using this technique one has to be aware of the error resulting from statistical fluctuations. Because of the numerous parameter combinations examined in the study and the extended computing time needed we had to restrict the duration of the simulations to 55 years (two

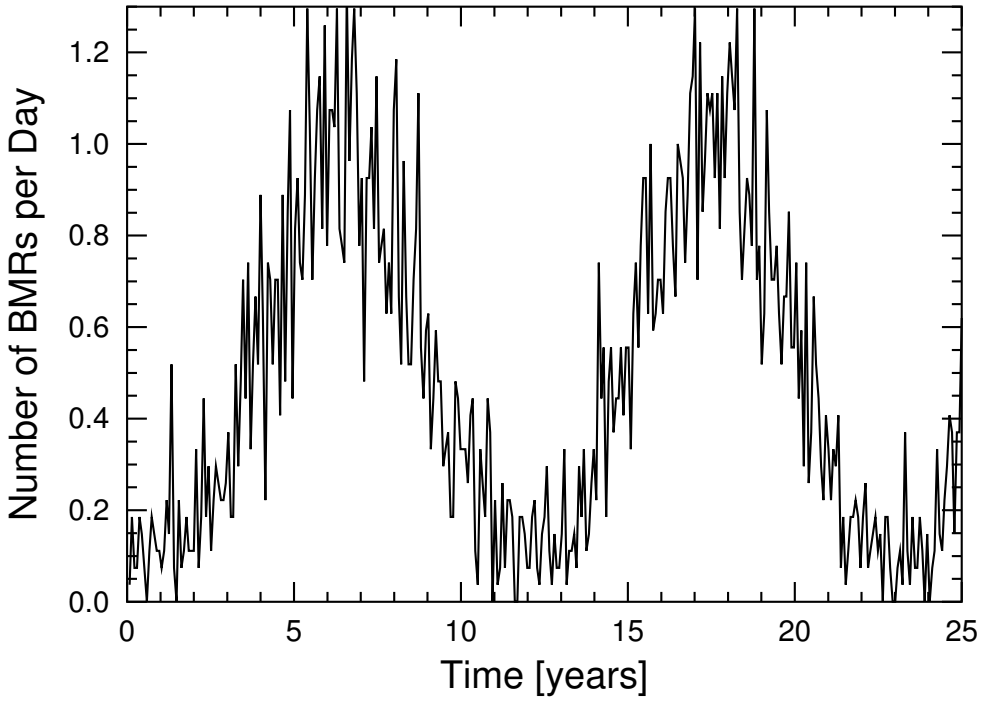

Figure 4.1: The cycle activity for the reference parameter set. The number of BMRs emerging per day are averaged over 27 days.

and a half magnetic cycles). For test purposes averages of many cycles have been calculated for some cases to ensure that the obtained results are reliable. Typical fluctuations of the large-scale magnetic field resulting from the random nature of the BMR properties do not exceed a few percent.

4.2.5 Initial field configuration

To start a simulation, an appropriate initial flux distribution is needed. For a given set of parameters, the initial field is chosen such that poleward meridional flow and equatorial diffusion approximately balance (van Ballegooijen et al. 1998),

$$v_0 B_r \approx \frac{\eta_h}{R_\odot} \frac{\partial B_r}{\partial \theta} \,. \tag{4.4}$$

This configuration corresponds to the situation at cycle minimum when only few BMRs emerge and the polar regions have maximal flux. The explicit form of the radial magnetic field results from Eqs. (4.2) and (4.4):

$$\begin{aligned} B_r \quad & (R_\odot, \lambda) = \\ = \quad & \begin{cases} \text{sign}(\lambda) B_0 \exp[-a_0(\cos(\pi\lambda/\lambda_0)+1)] & \text{if } \ |\lambda| < \lambda_0 \\ \text{sign}(\lambda) B_0 & \text{otherwise}\,, \end{cases} \end{aligned} \tag{4.5}$$

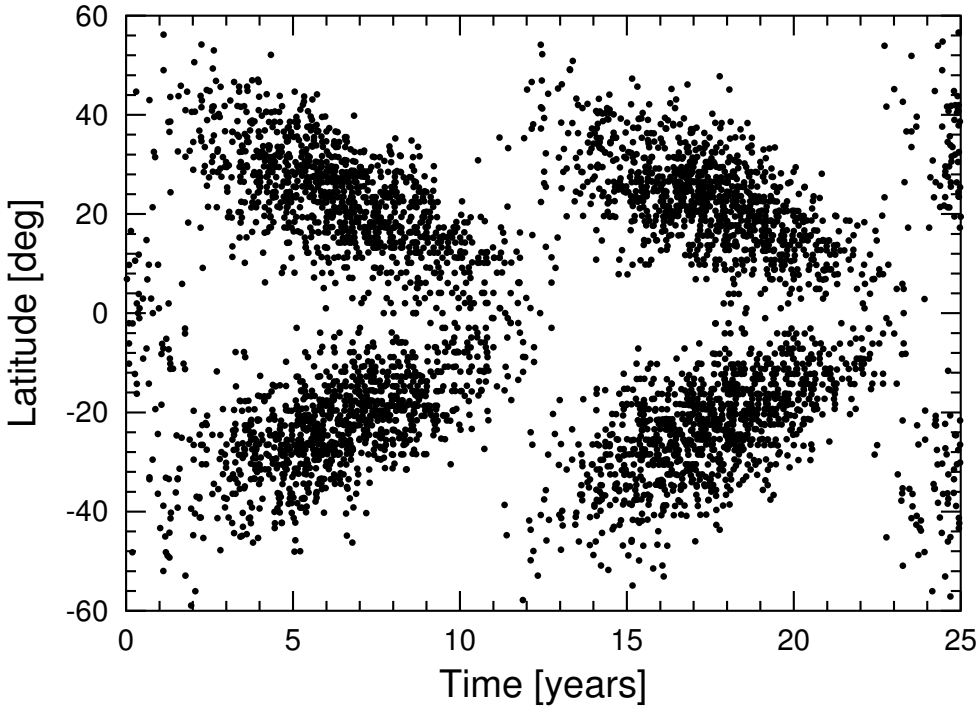

Figure 4.2: Simulated butterfly diagram, latitudes of emerging active regions plotted vs. time, for the reference parameter set.

where λ is the latitude, $\lambda_0 = 75°$, $a_0 = v_0\, R_\odot\, \lambda_0/(\pi\, \eta_h)$, sign$(\lambda)$ is the sign of the latitude and B_0 is the initial polar magnetic field strength, which has to be adjusted for each actual parameter set to avoid asymmetry of the global magnetic field with respect to the equator. The initial field given by Eq. (4.5) represents a situation where a new cycle is just about to start while the old decaying cycle is still ongoing due to an activity overlap set to two years (see Sect. 4.3.1). Note that the initial radial field distribution is independent of longitude, i.e. it is axisymmetric.

4.3 Reference cycle model

4.3.1 Reference cycle parameters

In order to study the dependence of global magnetic properties on the cycle parameters, a reference case based on solar cycle parameters closely resembling the observed large-scale field evolution is defined. The length of each cycle is set to 13 years with an overlap time of two years between consecutive cycles. This overlap time is introduced on the basis of the work of Harvey (1992, 1993) and Hathaway et al. (1994), who showed that BMRs belonging to a new cycle start emerging while BMRs of the old cycle are still appearing. Note that due to this overlap the interval between two peaks of flux emergence is 11 years.

At the beginning of a cycle, BMRs emerge at a mean latitude of $40°$, with a standard deviation of $10°$. Towards the end of a cycle, the mean emergence latitude decreases to

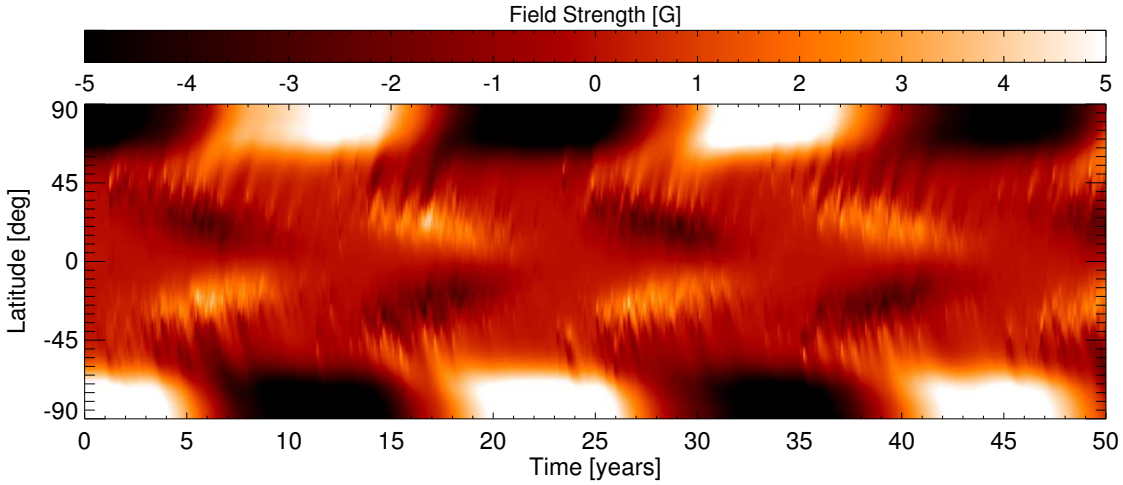

Figure 4.3: Time-latitude plot of the surface magnetic field for the reference case. The magnetic field is averaged over longitude and over a time period of 27 days. The saturation level of the colour shading is set to 5 G (see bar at top).

$5°$, with a standard deviation of $5°$. Emergence longitudes are assumed to be random, i.e. we neglect possible active longitudes. Unlike the true solar cycle which rises faster than it declines, the activity cycle in the simulation is represented by a Gaussian curve, i.e. it is symmetric around the time of maximum, which is reached 6.5 years after the beginning. Asymmetric cycles are studied in Sect. 4.4.10, where we find that asymmetry does not strongly affect the results. Fig. 4.1 shows the number of BMRs emerging per day as a function of time. The corresponding butterfly diagram is plotted in Fig. 4.2. The angle of the BMR, i.e. the angle between the line connecting the two centres of the polarities and the east-west line, is taken according to Joy's law, $\alpha = 0.5\,\lambda$ (λ is the latitude).

The polarity separations, $\Delta\beta$, of the simulated BMRs range from $3.5°$ to $10°$ in heliographic latitude with a step width of $0.1°$. This corresponds to region sizes of 30 to 250 square degrees. Smaller regions or even ephemeral regions cannot be simulated, because of the limited numerical resolution. The assumed size distribution function is $n(A) \sim A^{-2}$, where A is the area. This relation was found by Schrijver and Harvey (1994) through a power-law fit of the observed distribution of regions exceeding 3.5 square degrees in area. The biggest observed active regions in their study do not exceed 75 square degrees. For full-disk magnetograms excluding sunspots they yielded a linear relationship between the region size and its magnetic flux. The modelling of the active regions in the simulations as described above also leads to an almost linear relation between region size and flux content. The modelled BMRs are bigger in size than the ones emerging on the Sun. The larger areas in the simulations are necessary in order to account for the additional flux emerging in the ephemeral active regions, which are neglected in the current simulations. A value of $B_{\max} = 250$ G in Eq. (3.20) leads to a smaller slope in the flux–area relation than found by Harvey, but ensures that the total number of roughly $2\,100$ BMRs per cycle leads to a total input flux of approximately 10^{25} Mx. A similar flux input of $8.9 \cdot 10^{24}$ Mx per eleven-year cycle has been determined by Harvey and Zwaan (1993).

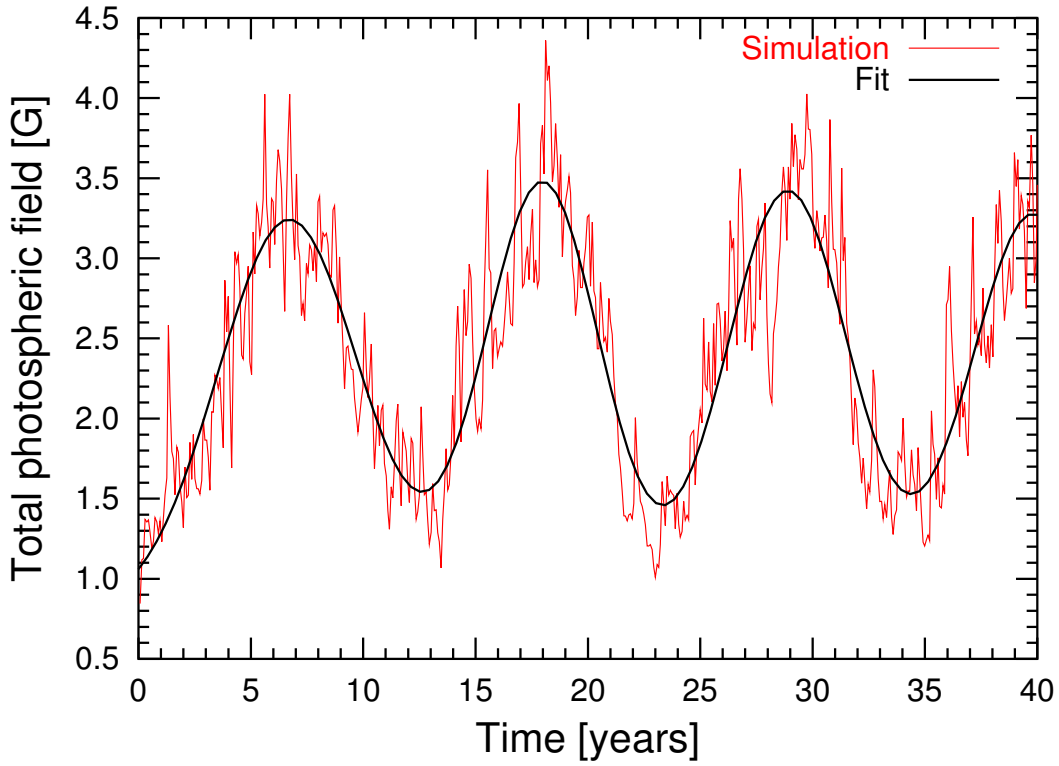

Figure 4.4: Evolution of the total photospheric field (Eq. 4.6) for the reference case. The total field is calculated every 27 days (red line). The black line represents a nonlinear least-squares fit (Eq. 4.7).

Fig. 4.3 shows the magnetic butterfly diagram, i.e., a longitude-averaged time-latitude plot for the surface magnetic field, for the reference parameter set.

4.3.2 Unsigned magnetic flux

The total unsigned photospheric flux is obtained by integrating the radial field over the solar surface

$$\Phi_{\rm tot} \;=\; R_\odot^2 \int |B_r(R_\odot,\theta,\phi,t)|\,{\rm d}S\,. \tag{4.6}$$

Fig. 4.4 shows the unsigned average flux density $B_{\rm tot} \equiv \Phi_{\rm tot}/(4\pi R_\odot^2)$, for the reference case. In the simulation, the field strength is calculated every 27 days. The fluctuations of the magnetic field make it hard to detect maxima and minima and compare them with the results for other parameter sets. Therefore the flux density is fitted using the nonlinear least-squares Marquardt-Levenberg algorithm (Press et al. 1992). A sum of Gaussians is taken to start the fitting procedure

$$B_{\rm Fit}(t) \;=\; \sum_1^N a_i \exp\left(\frac{-(t-b_i)^2}{e_i}\right)\,, \tag{4.7}$$

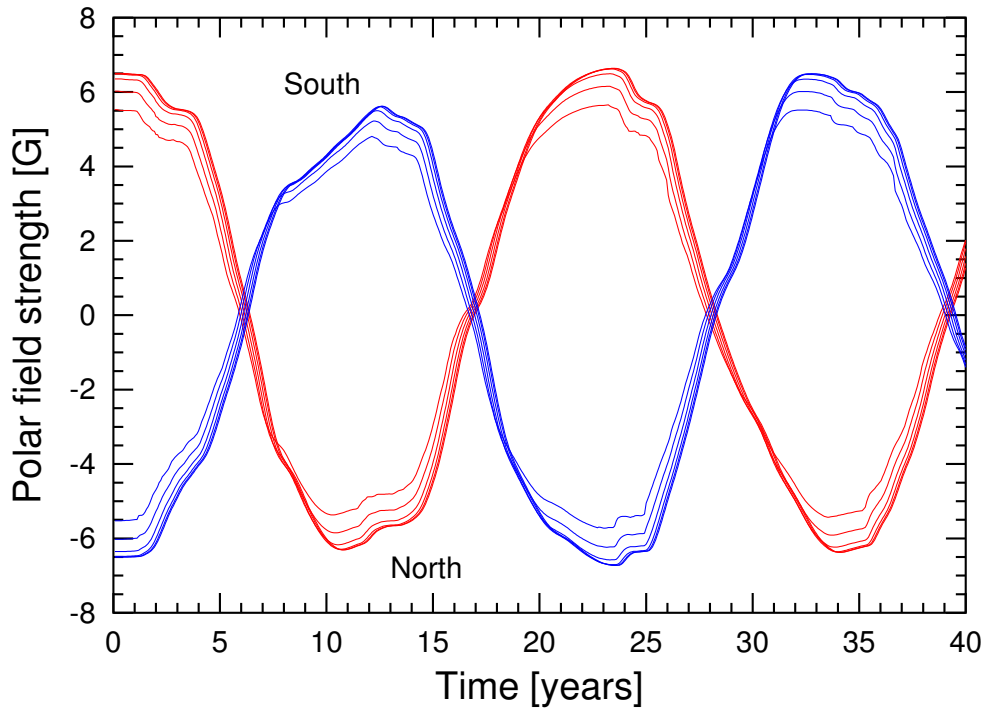

Figure 4.5: North and south polar field calculated for sizes of the polar caps from $5°$ (largest field strength) to $30°$ angular width (smallest field strength) in steps of $5°$.

where N is the number of maxima and a_i, b_i and e_i are fitting parameters. The result of this fitting procedure is shown as the solid line in Fig. 4.4. The cycle maxima and minima given below are obtained by averaging over all extrema of the fitted curve for the simulated time series.

4.3.3 Polar fields

During solar minima, the polar fields reach their maximum values. The cycle of the Sun's polar magnetic field is in antiphase to the Sunspot activity cycle. Svalgaard et al. (1978) derived an average polar cap field of $5\,\mathrm{G}$ during minimum and proposed an axisymmetric distribution of the large-scale field of the form $B = \pm 11.5 \cos^2\theta$ G. More recently, the Ulysses mission confirmed a polar field strength of $5\,\mathrm{G}$ (Smith and Balogh 1995). The polar field contributes strongly to the interplanetary and heliospheric field (open flux). Therefore, the evolution of the magnetic flux in the polar caps is an important quantity, but no unique definition of what constitutes the polar caps exists. In the literature, definitions for the solar polar caps range from the field within $10°$ of the pole to that within $30°$. Fig. 4.5 shows the calculated polar fields of the reference case for caps ranging in angular width from $5°$ to $30°$. Apparently, the exact choice of this width does not have a strong effect on our results. We adopt a value of $15°$ for the polar cap in the remainder of the paper. In our analysis we are interested in the maximum values reached by the spatially averaged fields in these polar caps.

The maximum polar field strength is determined by averaging over the absolute values of all maxima and minima of both polar caps obtained during a simulation. To get the maximum values, the polar fields have been decomposed into their Fourier components. A few components turn out to be sufficient to well approximate the field and to remove noise. The different analysing technique compared with the fit procedure as used for the total surface field is necessary because the shape of the polar field is a priori not known in contrast to the total surface field, which follows approximately the shape of the cycle activity.

Table 4.1: Overview of the studied parameters and their influence on the total unsigned flux ($B_{\rm tot}$) and the polar field ($B_{\rm pole}$).

Parameter	Standard case	Range	Dependence of $B_{\rm tot}$	Dependence of $B_{\rm pole}$	Sect./ Fig.
Diffusion coefficient η_h [$\mathrm{km^2\ s^{-1}}$]	600	$50 - 1500$	decrease	strong decrease; saturates for $\eta_h \gtrsim 500$	4.4.1 / 4.6
Meridional flow amplitude v_0 [$\mathrm{ms^{-1}}$]	11	$0 - 30$	weak decrease	reaches maximum at $v_0 = 8$	4.4.2 / 4.8
Differential rotation	$k = 1$	$k = 0 - 10$	decrease	no effect	4.4.3 / 4.11
Activity level	1 (solar case)	$0.2 - 10$	power-law	linear increase	4.4.4 / 4.12
Cycle overlap [years]	2	$0 - 6$	background forms for $B_{\rm tot,min}$	weak decrease	4.4.5 / 4.13
Cycle length [years]	13	$5 - 20$	weak variation	increase	4.4.6 / 4.15
Size distribution	$\propto A^{-2}$	A^{-p}, $p = 1 - 4$	decrease	weak decrease	4.4.7 / 4.17
Tilt angle	$0.5\,\lambda$	$0.1\,\lambda - 2.0\,\lambda$	linear increase	linear increase	4.4.8 / 4.20
Scatter of tilt angles [deg]	0	$0 - 30$	no effect	no effect	4.4.8 / -
Shift of emergence latitudes [deg]	40	initially $35 - 60$	$B_{\rm tot,min}$ decreases, $B_{\rm tot,max}$ increases	increase	4.4.9 / 4.22
Slope of mean emergence line [deg]	$40/5$ (start/ end of cycle)	$22.5/22.5$ to $45/0$	no effect	weak decrease	4.4.9 / 4.23
Spread around mean emergence line [deg]	$10/5$ (start/end)	$0 - 20$	no effect	no effect	4.4.9 / -
Position of activity maximum [years]	6.5 (= 0.5 cycle length)	$1 - 12$	no effect	no effect	4.4.10 / Table 4.2

4.4 Parameter study: results and discussion

For the study of the influence of the model parameters, i.e. diffusion coefficient, meridional flow amplitude and differential rotation rate, we use the same synthetic emergence sequence of BMRs in all calculations, while for the study of the cycle parameters new sequences of BMRs were created for each simulation.

Table 4.1 gives an overview of the parameters studied and the results of the corresponding simulation runs. Besides the description of the parameter (column 1), the value adopted for the standard case (column 2), and the range of values tested (column 3), we list the qualitative dependence of $B_{\rm tot}$ (column 4) and $B_{\rm pole}$ (column 5), the section in which this dependence is described as well as the number of the figure in which it is plotted (last column). The three parameters listed above the horizontal line are parameters of the model that enter into Eq. (4.1), while the remainder enters indirectly through the source term.

4.4.1 Magnetic diffusivity

In order to obtain the dependence of the global magnetic field properties on the diffusion rate, simulations with diffusion coefficients in the range $50 - 1500\,\mathrm{km^2\ s^{-1}}$ have been run (the value adopted for the reference model is $600\,\mathrm{km^2\ s^{-1}}$). Fig. 4.6 a shows how the maximum and minimum magnetic surface fields, $B_{\rm tot,max}$ and $B_{\rm tot,min}$ respectively, vary with increasing diffusion coefficient. A higher diffusion rate leads to a faster spreading of the BMRs. Neighbouring magnetic polarities approach each other faster than at a lower diffusion rate, leading to enhanced cancellation of flux and thus to the decrease in $B_{\rm tot,max}$ seen in Fig. 4.6 a. This effect can be clearly seen in the magnetic butterfly diagrams for low ($50\,\mathrm{km^2\ s^{-1}}$) and high ($1500\,\mathrm{km^2\ s^{-1}}$) diffusion rates shown in Fig. 4.7 a and Fig. 4.7 b. In the first case meridional circulation dominates, carrying a large amount of flux to the poles, whereby early in a cycle the following polarity contributes more to the field being transported to high latitudes than later in the cycle. We expect that this is due to Joy's law, with the tilt angles of BMRs being larger at high latitudes (i.e. early in the cycle).

The polar field shows a similar behaviour as the maximum of the total magnetic field (Fig. 4.6 b). For a diffusion rate of $50\,\mathrm{km^2\ s^{-1}}$, $B_{\rm pole}$ is 14.5 G. This amplitude decreases rapidly with higher diffusion rates, and for $\eta_h \approx 500\,\mathrm{km^2\ s^{-1}}$ a saturation level of about 6 G is reached.

At still higher diffusion rates the enhanced cancellation of magnetic flux in the activity belts leaves less magnetic flux to migrate towards the poles. On the other side, a higher diffusion rate leads to more cross-equatorial cancellation of mainly preceding polarity flux. Both effects run contrary to each other and balance for high η_h so that $B_{\rm pole} \approx$ const. $B_{\rm tot,min}$ is mainly dominated by the polar field for high diffusion rates and thus shows a similar behaviour as $B_{\rm pole}$ for large values of η_h.

4.4.2 Poleward meridional flow

We consider meridional flow velocities in the range between 0 and $30\,\mathrm{ms^{-1}}$. In the absence of a meridional flow ($v_0 = 0$), most of the magnetic flux remains at low latitudes

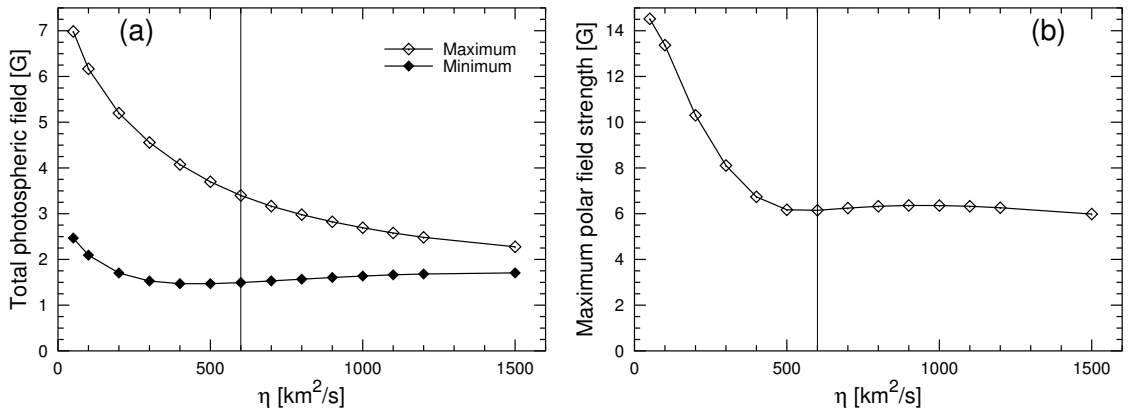

Figure 4.6: (a) Total photospheric field at cycle maximum ($B_{\mathrm{tot,max}}$) and minimum ($B_{\mathrm{tot,min}}$) vs. diffusion coefficient, η_h. The vertical line indicates the reference case. (b) Polar field strength B_{pole} vs. diffusion constant, η_h. The plotted values are the averages of the absolute values of all maxima or minima.

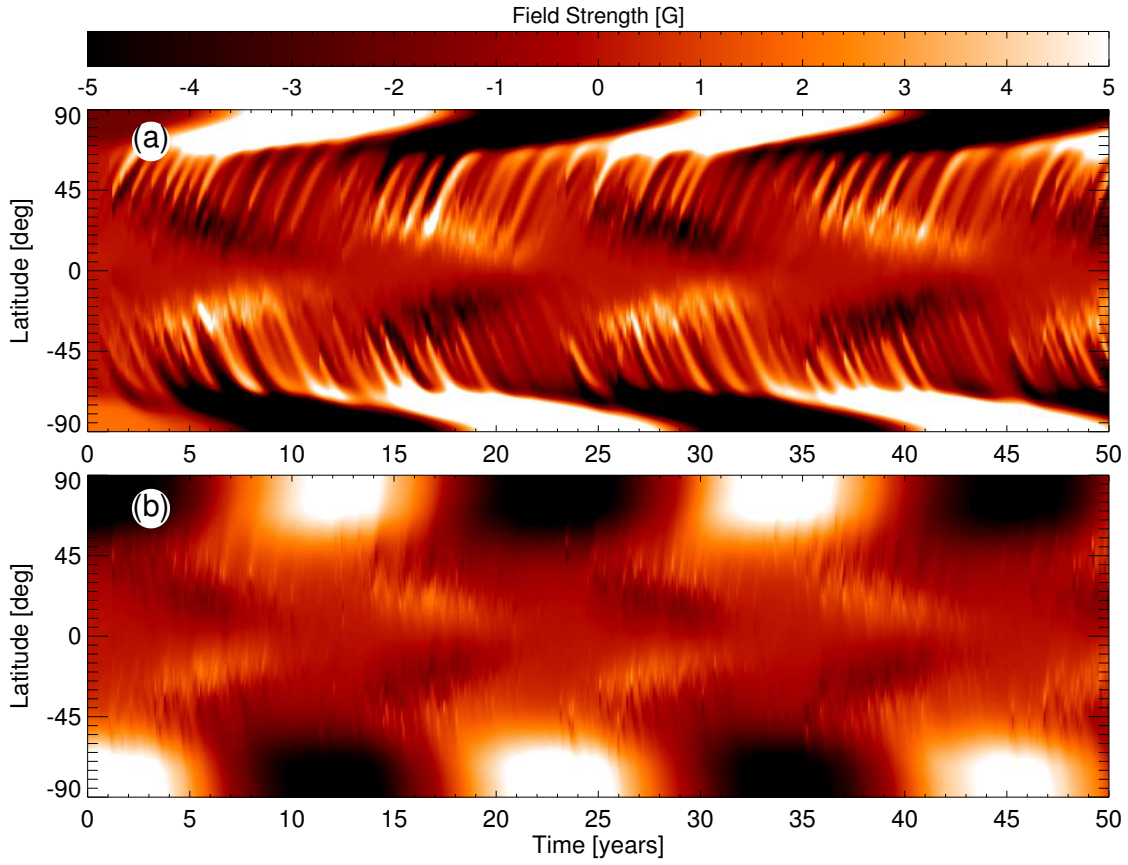

Figure 4.7: Magnetic butterfly diagrams for the extreme values of the diffusivity: $\eta_h = 50\,\mathrm{km^2\ s^{-1}}$ (a) and $\eta_h = 1500\,\mathrm{km^2\ s^{-1}}$ (b).

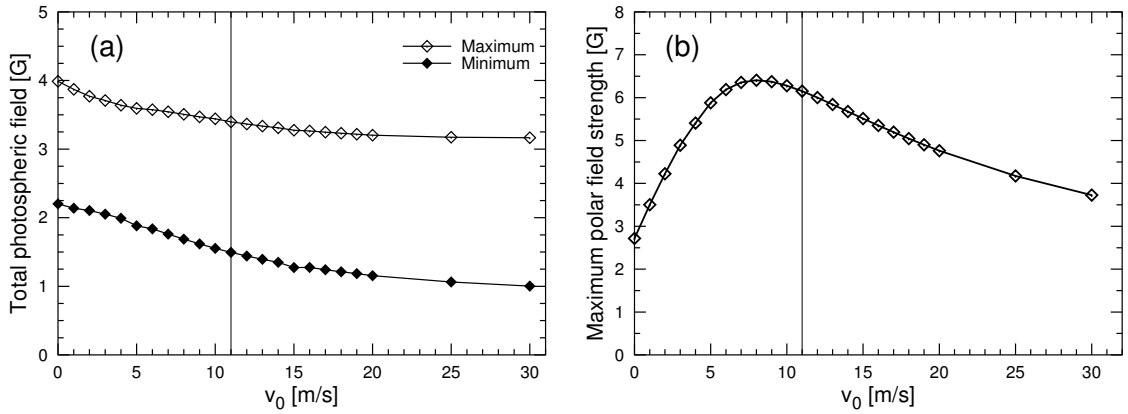

Figure 4.8: (a) $B_{\mathrm{tot,max}}$ and $B_{\mathrm{tot,min}}$ vs. meridional flow amplitude, v_0. The vertical line indicates the reference case. (b) Polar field strength B_{pole} vs. flow amplitude.

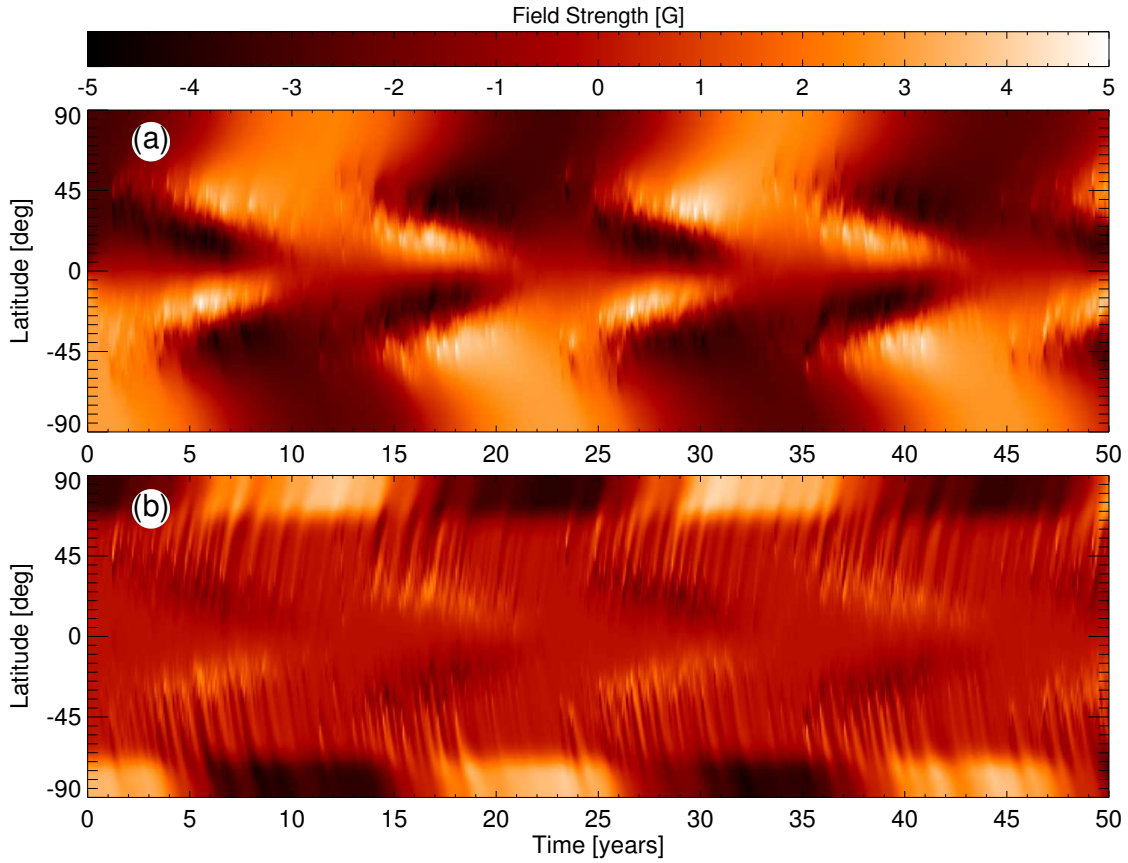

Figure 4.9: Magnetic butterfly diagrams for the extreme cases of absence of a poleward meridional flow (a), and for a meridional flow amplitude of $v_0 = 30\,\mathrm{ms}^{-1}$ (b).

and the polar field extrema are about 3 G (Fig. 4.8 b). However, magnetic flux transport only by diffusion is sufficient to reverse weak polar fields, as is clearly visible in the corresponding magnetic butterfly diagram (Fig. 4.9 a), which shows rather diffuse fields at high latitudes, in contrast to the corresponding diagrams for reduced diffusion (Fig. 4.7 a) or enhanced v_0 (Fig. 4.9 b). These latter show sharp stripes at high latitudes as flux from individual BMRs is transported to the poles, with the following polarity dominating, but also including distinct stripes of the preceding polarity.

$B_{\rm pole}$ as a function of v_0 initially increases as more following polarity flux is carried to the poles. Also, an enhanced meridional flow reduces the diffusive dispersion of the polar fields. As v_0 becomes even larger, cross-equatorial cancellation is reduced. Both magnetic polarities are carried to the pole by the meridional flow and cancel there. This leads to a reduction of $B_{\rm pole}$. The strongest polar fields form for intermediate meridional flow speeds of $v_0 = 8\,{\rm ms}^{-1}$.

A higher poleward meridional flow transports the opposite polarities to the smaller area in the polar regions, leading to more efficient cancellation and thus reduction of the total flux (Fig. 4.8 a).

4.4.3 Differential rotation

In this section, we modify the differential rotation (Eq. 4.3) such that the rotation rate at the equator becomes k times the solar value while the rotation rate at the poles remains at the solar value,

$$\omega_k(\theta) \;=\; \Big[(k-1)(\sin\theta+1)-(k-2)\Big]\cdot\omega(\theta)\,, \tag{4.8}$$

where $\omega(\theta)$ is given by Eq. (4.3). The resulting rotation profiles are plotted in Fig. 4.10 for $k = 1\ldots10$. The surface shearing due to differential rotation leads to flux cancellation by bringing opposite polarities together (see Figs. 2-4 in Mackay et al., 2002a). This effect is especially pronounced at mid latitudes and thus in the activity belts where a mixture of both polarities is present. Fig. 4.11 shows how $B_{\rm tot}$ decreases with increasing k. During cycle maxima the influence of the differential rotation on the total unsigned flux is significant. At minima, where only few BMRs are present and thus are more separated in longitude, a stronger differential rotation has only a weak effect on the total field.

The polar field is not influenced by differential rotation, which can be explained analytically: integrating the flux transport equation (Eq. 4.1) over a circle of constant latitude from 0 to 2π in longitude leads to a value independent of $\omega(\theta)$. For fixed values of the diffusion coefficient, the meridional flow and the source function, the average polar field is therefore independent of the differential rotation with a value of $B_{\rm pole} = 6.2$ G, for all differential rotation profiles.

4.4.4 Activity level

Next we consider the influence of changing activity level, i.e. total amount of emerging flux or cycle strength. This is relevant for solar cycles of varying strength and for stars with different activity levels. We describe higher activity levels through a larger number of emerging BMRs and thus a larger amount of emerging flux while keeping the size

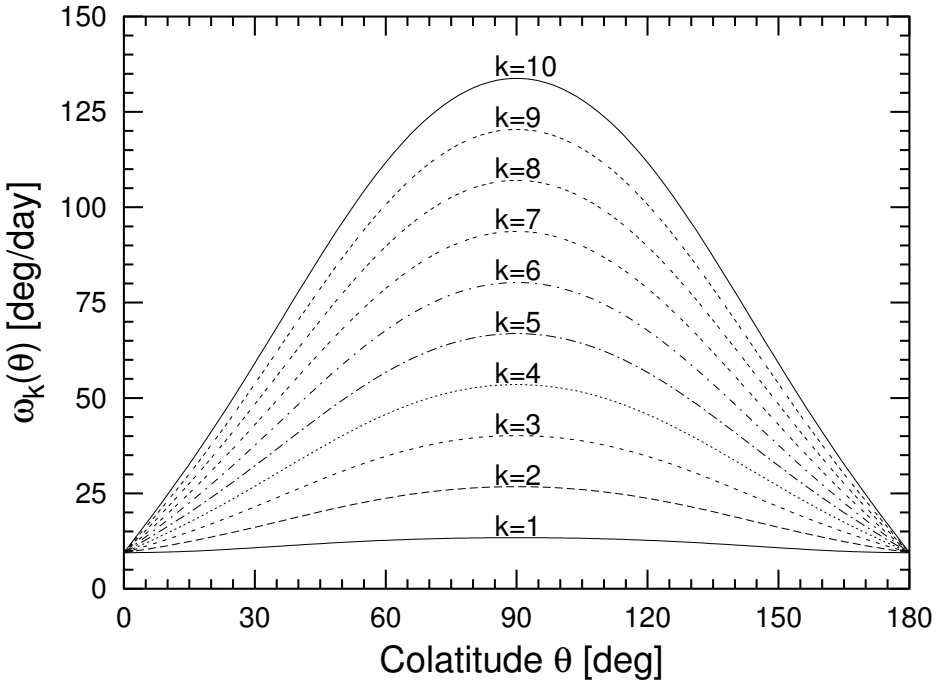

Figure 4.10: Modified differential rotation profile vs. colatitude. The equator is assumed to rotate k-times faster than in the rotation curve of Snodgrass (1983), while the the rotation at the poles is equal to the Snodgrass rotation, i.e. the standard case.

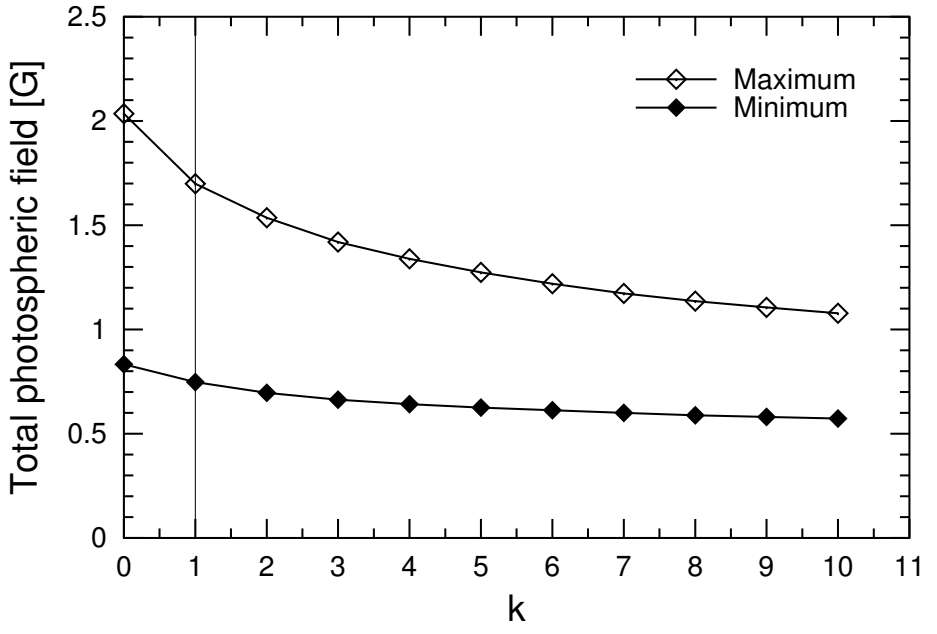

Figure 4.11: $B_{\mathrm{tot,max}}$ and $B_{\mathrm{tot,min}}$ vs. k in the modified rotation profile (Eq. 4.8).

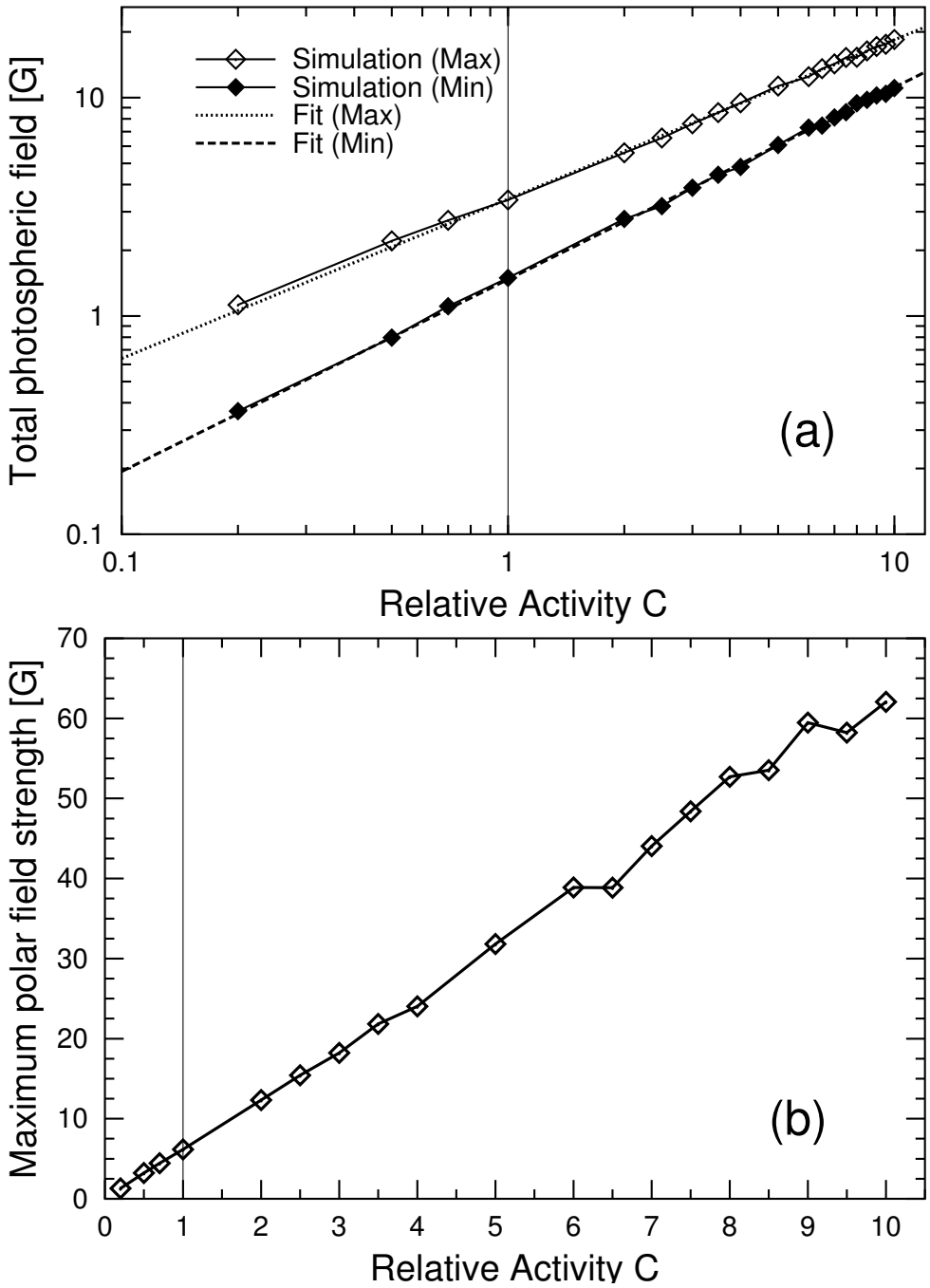

Figure 4.12: (a) Logarithmic plot of $B_{\mathrm{tot,max}}$ and $B_{\mathrm{tot,min}}$ vs. relative activity level C of cycle at its maximum and minimum. The fitted curves are also plotted. (b) B_{pole} vs. the relative activity level of cycle.

distribution of emerging BMRs unchanged. To this end, we multiply the standard values $N = 2\,100$ for the number of BMRs per cycle and $\Phi_{\rm em,tot} = 1.25 \cdot 10^{25}$ Mx for the total emerging magnetic flux both by a factor, C, where $C = 1$ corresponds to the reference parameter set (solar case).

The simulation results are presented in Fig. 4.12 a. Power-law fits (dotted and dashed lines in Fig. 4.12 a) reveal the following dependence of the total surface field on the activity level: $B_{\rm tot,max} = 3.43\,C^{0.73}$ G for cycle maxima and $B_{\rm tot,min} = 1.47\,C^{0.88}$ G for cycle minima. Consequently, the total flux increases at a less than linear rate with increasing activity or emerging flux. As more BMRs emerge on the surface, opposite polarities emerge closer to each other, leading to more cancellation of magnetic flux. The larger exponent for $B_{\rm tot,min}$ probably arises from the fact that at activity minimum a significant fraction of the field resides in the polar caps, where a single polarity dominates.

The polar fields evolve linearly with the activity amplitude (Fig. 4.12 b). Power-law fits yield $B_{\rm pole} = 6.15\,C^{1.01}$ G. Similar results have been found by Schrijver and Title (2001). This behaviour is probably due to the fact that cross-equator flux cancellation also increases rapidly with activity level, so that the preferred transport of following-polarity flux to the poles is correspondingly enhanced.

Within the wide parameter range considered here, the surface evolution of the field does not lead to a saturation of $B_{\rm tot}$ or $B_{\rm pole}$. The saturation of activity on very rapidly rotating stars (Vilhu and Rucinski 1983) is therefore probably not caused by cancellation of the magnetic field at the stellar surface. The power-law exponent of 0.73 between $B_{\rm tot,max}$ and emerging flux suggests that some contribution from this effect may be present, but it is not likely to dominate.

4.4.5 Overlap time of successive cycles

In this section we study the influence of the overlap time of successive cycles, which is set to two years in the reference model. The length of the individual cycle remains at 13 years.

The simulations show that the surface flux during maxima is not influenced by varying the overlap time between 0 and 6 years (Fig. 4.13 a). In contrast, the field during activity minima grows rapidly with the overlap between consecutive cycles. This result is in agreement with the predictions of the simple model describing the long-term evolution of the Sun's large-scale magnetic field by Solanki et al. (2000, 2002b) and with the simulations of Schrijver et al. (1997). The growth of the field during minima can easily be understood by inspecting the butterfly diagram (Fig. 4.14 a and b). For a large overlap (Fig. 4.14 b), the simultaneous presence of two activity belts at high and low latitudes is clearly visible. In this extreme case for which the overlap time is half the cycle length, one cycle ends during the maximum of the following cycle and the photospheric flux no longer varies significantly with time (Fig. 4.13 a). Thus the build-up of a background field by increasing the overlap time leads to a proportional decrease of the cycle amplitude.

For the polar fields, the effect of overlapping cycles corresponds to a decrease in the cycle length. The time during which magnetic flux is transported to the poles is reduced. The time between polar maxima decreases, with always the following-polarity flux from the cycle with higher emergence latitudes being at an advantage in reaching the poles. Therefore, the polar fields decrease with longer cycle overlaps (Fig. 4.13 b). Why do

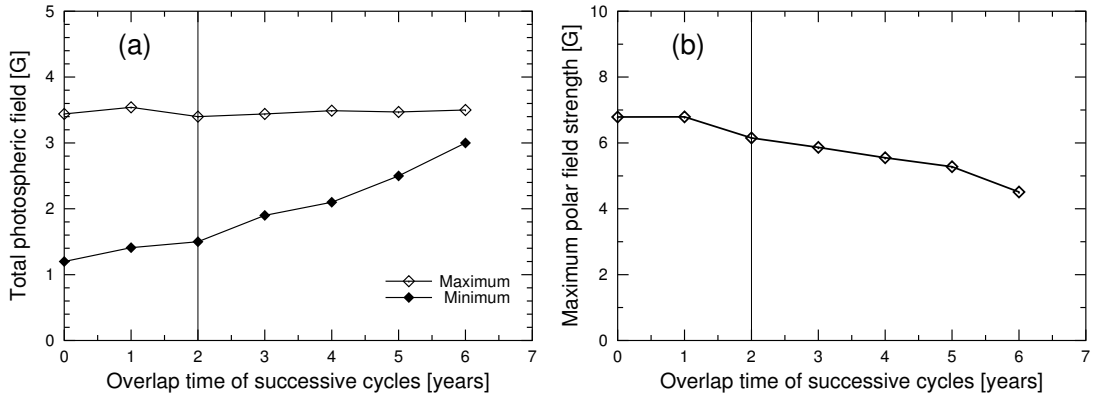

Figure 4.13: (a) $B_{\mathrm{tot,max}}$ and $B_{\mathrm{tot,min}}$ vs. overlap time of consecutive cycles. (b) Polar field strength vs. overlap time.

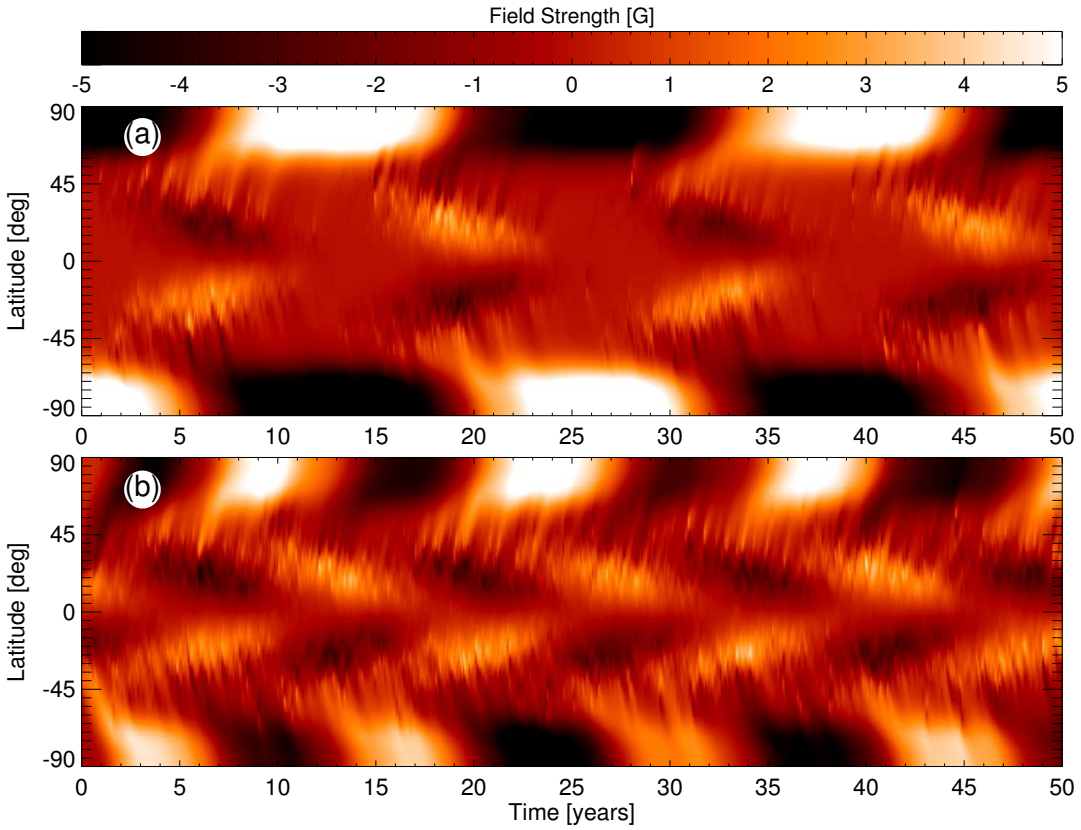

Figure 4.14: Magnetic butterfly diagrams for no overlap between successive cycles (a) and for an overlap time of 6 years (b).

cycles dominantly feed the polar flux during their early phases? We believe that this is due to a combination of effects. The emergence latitudes are higher and thus the tilt angles are larger during the initial phases. As we will see in Sects. 4.4.8 and 4.4.9, both of these parameters have a large effect on the polar fields.

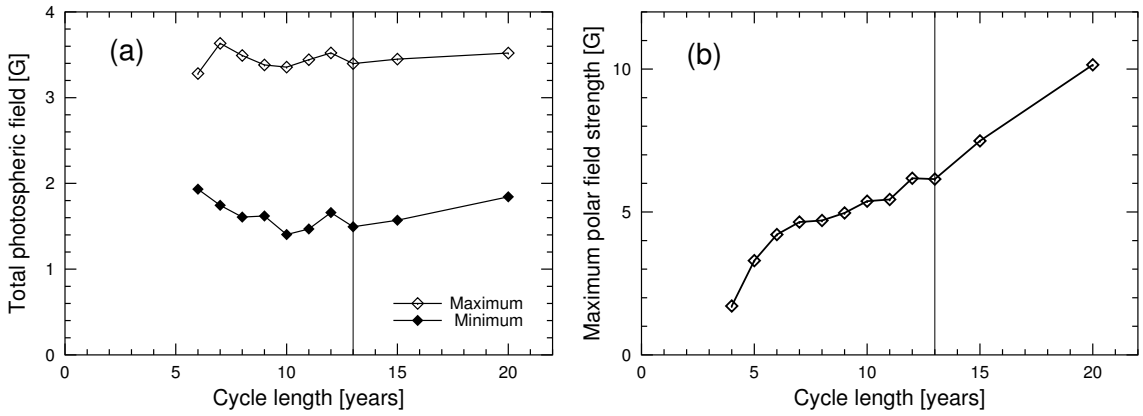

Figure 4.15: (a) $B_{\mathrm{tot,max}}$ and $B_{\mathrm{tot,min}}$ vs. cycle length. (b) B_{pole} as a function of cycle length.

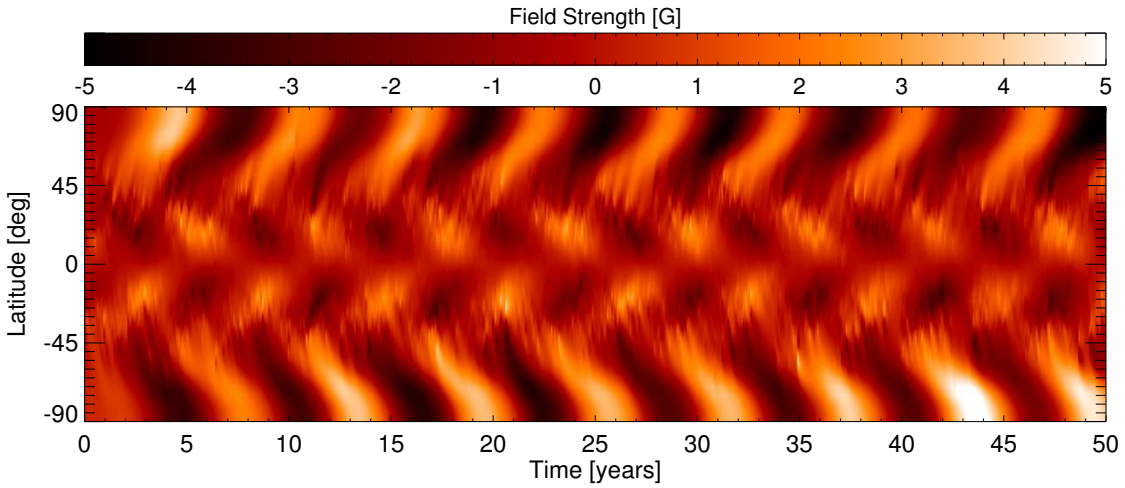

Figure 4.16: Magnetic butterfly diagram for a cycle length of 5 years. The overlap time between successive cycles is 2 years.

4.4.6 Cycle length

The length of the cycle has been varied from 4 to 20 years, keeping the overlap between two successive cycles always at a value of two years. The cycle amplitude was maintained at a fixed level, so that the number of emerging BMRs varied linearly with the cycle length. The simulations show that the maximum total surface flux remains roughly constant (Fig. 4.15a) while $B_{\mathrm{tot,min}}$ displays a more complex behaviour. For short cycles (length $\lesssim$ 10 years) $B_{\mathrm{tot,min}}$ decreases with increasing length, while for longer cycles it increases gradually. The polar fields increase roughly linearly with the cycle period (Fig. 4.15 b).

In a longer cycle, more BMRs emerge and contribute to the polar fields by preferential

poleward transport of following-polarity. Since the cancellation of flux in the BMRs and between BMRs takes place on a timescale much shorter than the cycle length, the total flux is hardly affected by cycle length, at least at cycle maximum. The meridional flow becomes particularly important to keep the polar caps from diffusing away over longer cycles. Diffusion of polar flux could be one reason why in the case of the Sun, longer cycles tend to be followed by weaker cycles (Solanki et al. 2002a, Makarov et al. 2003).

The strong decrease of the polar field strength for short cycle periods is partly also due to the two-year overlap of successive cycles. The magnetic butterfly diagram (Fig. 4.16) reveals that this enhances the decrease in the polar field at very short cycles (see Sect. 4.4.5). The poleward flux transport is dominated by diffusion which results in weak polar fields (see Sect. 4.4.2). The very short duration of the phase in which one dominant polarity is being transported to the pole (stripes of one colour in Fig. 4.16), means that over a considerable fraction of time opposite polarities are moving to the pole. Cancellation due to diffusion then reduces the polar flux. The decrease in $B_{\rm tot,min}$ with cycle period seen for short cycles is probably caused by the decreasing relative overlap between cycles as they get longer (compare Sect. 4.4.5). This effect is important for short cycles since the overlap in fraction of the cycle length is largest then.

4.4.7 Size distribution of BMRs

Schrijver and Harvey (1994) determined the size distribution of solar active regions during cycle 21 as $n(A) = 4.7\,A^{-2}$. An exponent of -2 is a critical value, since for less negative exponents the new flux brought to the solar surface is dominated by the large active regions, while for more negative exponents it is the small ephemeral regions that dominate. We applied size distribution functions of the form $n(A) \sim A^{-p}$ where p was varied between 1 and 4. In order to isolate the effect of the size distribution from other dependences, the total input flux from new regions was kept constant over the cycle by adjusting the total number of BMRs emerging over the cycle. For a higher value of p the probability of smaller regions increases and thus more regions have to emerge in order to reach a fixed amount of flux (Fig. 4.19).

The effect of the diffusion of the magnetic field and cancellation of magnetic flux is stronger in smaller active regions than in bigger ones. Therefore, the total surface flux is reduced when the distribution function is such that small regions are preferred (larger values of p in Fig. 4.17 a). This effect is most pronounced at activity maxima when the largest number of active regions are present. At cycle minima a fair fraction of the flux is concentrated at the poles and thus less affected by the size distribution (see Fig. 4.17 b), so that the total flux at minimum exhibits a weaker dependence on p. Field from bigger regions has a larger chance of reaching the polar caps owing to its longer lifetime (less cancellation due to diffusion) and thus the polar fields become stronger for lower values of p (Fig. 4.17 b). The weak dependence of the polar fields on p can be explained by the same argument as for the dependence on the diffusion coefficient: more cancellation of flux in the activity belts is counterbalanced by increased cross-equatorial cancellation.
The dominance of the large BMRs for $p = 1$ and of the small BMRs for $p = 4$ is seen in the magnetic butterfly diagrams (Fig. 4.18 a and b, respectively). The graininess of the field at both the emergence and higher (sub-polar) latitudes for $p = 1$ contrasts with the smoothness (produced by averaging in the plot over many smaller regions) for $p = 4$.

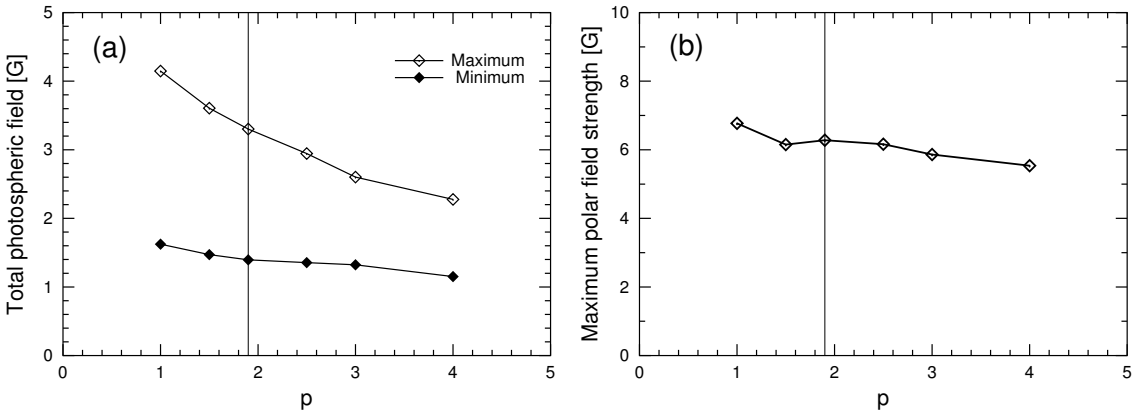

Figure 4.17: (a) $B_{\mathrm{tot,max}}$ and $B_{\mathrm{tot,min}}$ vs. exponent p in the size distribution function $n(A,t) \sim A^{-p}$. (b) Polar field strength vs. exponent p.

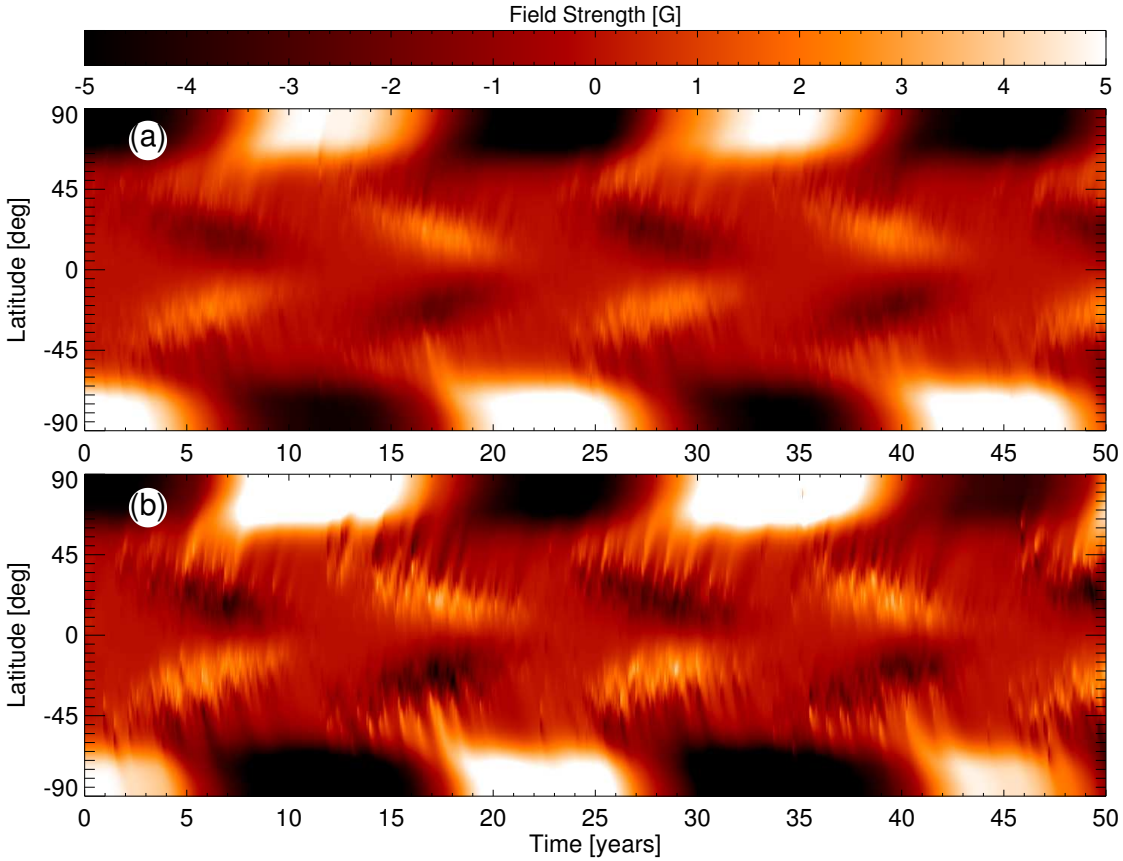

Figure 4.18: Magnetic butterfly diagrams for size distributions of active regions $\sim A^{-4}$ (a) and $\sim A^{-1}$ (b).

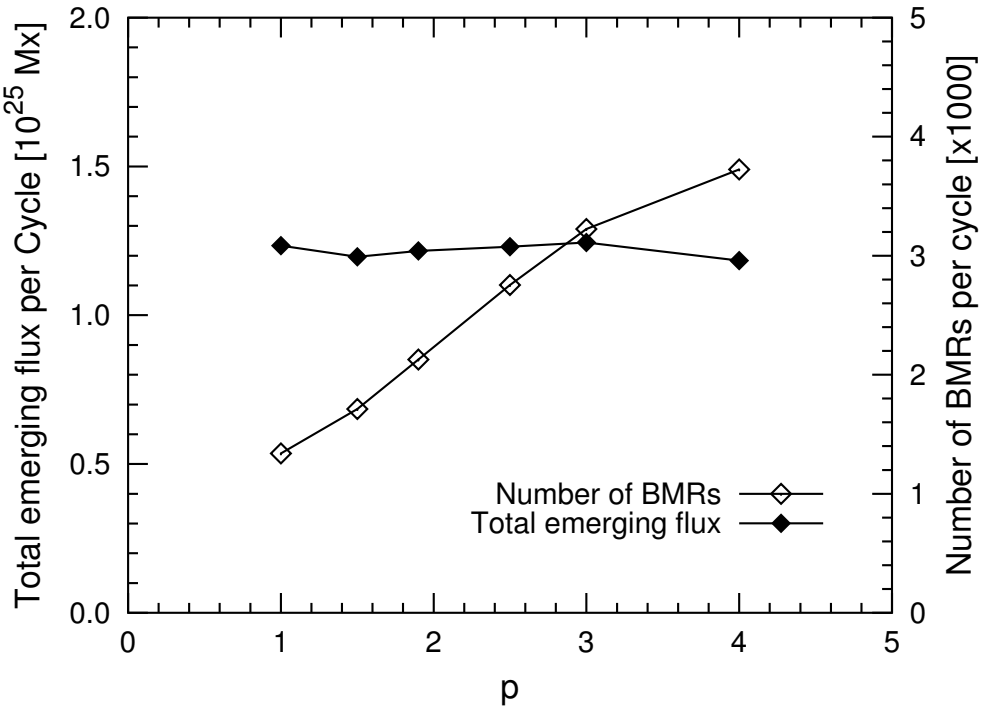

Figure 4.19: Number of emerging BMRs per cycle and total emerging flux per cycle vs. the exponent p in the size distribution function $n(A) \sim A^{-p}$. The total number of emerging BMRs in the individual simulations is set such that the total emerging flux remains roughly constant.

The upper panel looks more diffuse than the lower. The diffusion time τ_d depends on the scale $\tau_d = l^2/\eta_h$, where l is a typical length and η_h is the diffusion coefficient, while the timescale for the meridional transport τ_v does not ($\tau_v = R_\odot/v_0$). If l decreases, i.e. when smaller BMRs are preferred, the diffusion becomes more important than the meridional flow.

Although $B_{\rm pole}$, i.e. the maximal polar field strength, does not vary much with the size distribution, the temporal evolution of the polar fields changes as can be seen on the magnetic butterfly diagrams.

4.4.8 Tilt angle

The tilt angle of a BMR, $\alpha(\lambda)$, is a result of the Coriolis force acting on the underlying toroidal magnetic flux tube as it rises to the surface. Starting from Joy's law, $\alpha = 0.5\,\lambda$, we generalize the relation between tilt angle and latitude to $\alpha = b\,\lambda$ and vary the parameter b between 0.1 and 2. Differences in the average tilt angle are expected to occur on stars of different spectral type, evolutionary status and rotation rate (activity level), since the strength of the Coriolis force relative to other forces acting on the rising flux tube depends on these parameters (Schüssler and Solanki 1992, Schüssler et al. 1996).

$B_{\rm tot,max}$ shows a linear increase with b (Fig. 4.20 a). For larger tilt angles, opposite

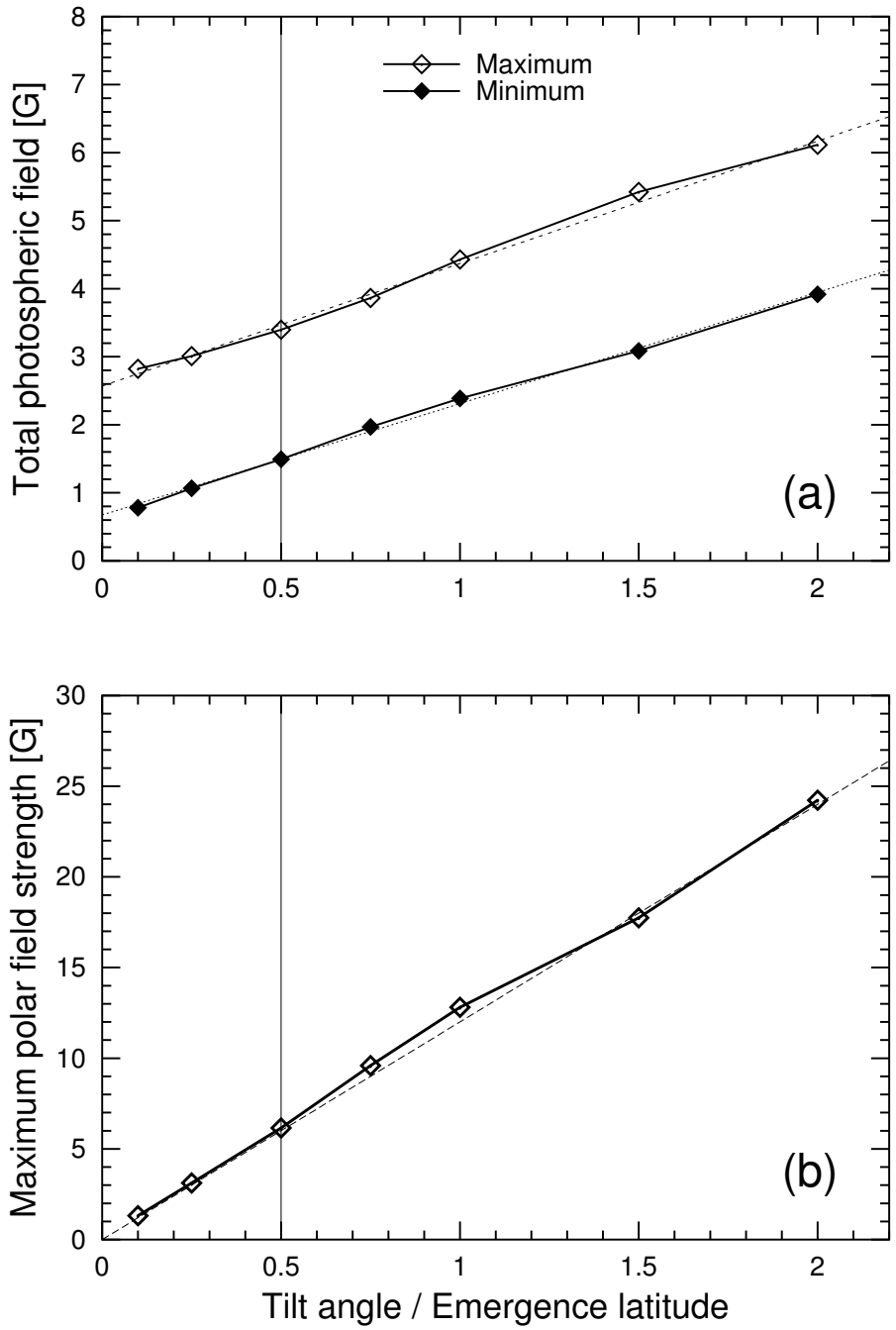

Figure 4.20: (a) $B_{\mathrm{tot,max}}$ and $B_{\mathrm{tot,min}}$ vs. parameter $b = \alpha/\lambda$ (α is the tilt angle and λ is the emergence latitude). (b) Polar field strength vs. b. The linear fits are also indicated.

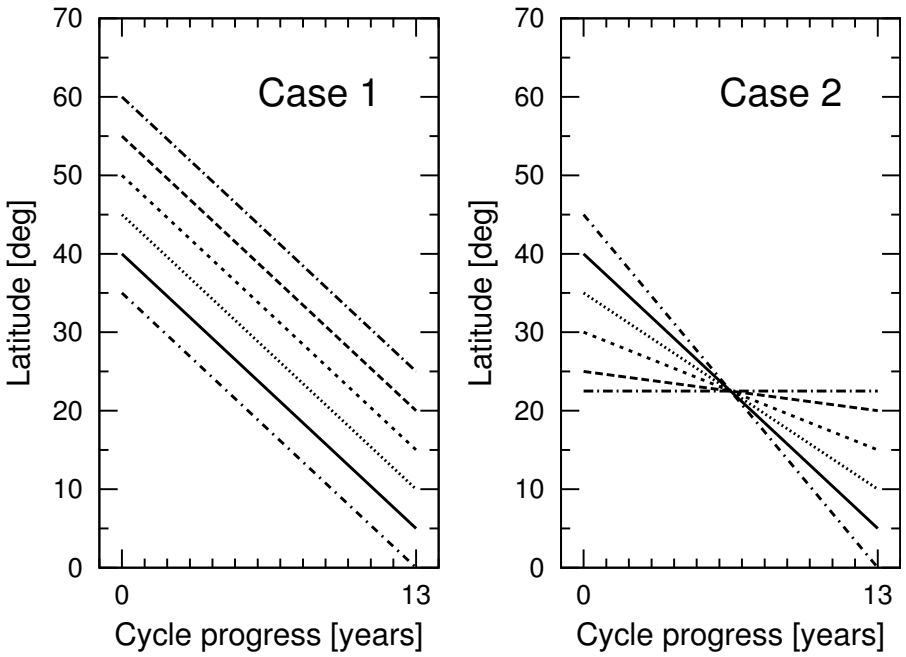

Figure 4.21: Sketch of the variation of the mean activity line in the butterfly diagram. *Left*: The mean line is shifted, with starting latitudes ranging from 35 to $60°$ (case 1). *Right*: Variation of the slope of the mean activity line (case 2). The solid line represents the reference case.

polarities from neighbouring BMRs are more separated in longitude and thus diffusion is less effective in flux cancellation. For larger tilt angles, cross-equatorial cancellation of preceding flux is enhanced (see the evolution of a single bipole described in Mackay et al., 2002a), leading to more flux on the solar surface and at the same time also to the accumulation of more flux at the poles. Thus the polar fields become stronger for higher values of b (Fig. 4.20 b). In the investigated range of b, the polar field strength is approximately $B_{\rm Pole} \approx 12\,b$, $B_{\rm tot,max} \approx 1.8\,b + 2.6$ and $B_{\rm tot,min} \approx 1.6\,b + 0.7$ (all values in G).

We have also considered the influence of a scatter in the tilt angles. The standard deviation of the tilts of individual BMRs around the mean is $\sim 19°$ (Wang and Sheeley 1989). We have considered random distributions of tilt angles with standard deviations ranging from $1°$ to $30°$. It turned out that this had no significant effect on both the total magnetic field and the polar field as long as average tilt angles were kept constant. The total fluxes at activity maximum and minimum varied by less than $10\,\%$ over the considered parameter range, while the polar field varies by less than $30\,\%$. Both quantities did not show a clear trend.

4.4.9 Emergence latitudes

A quantitative analysis of the influence of the emergence latitudes of the BMRs on the global field properties has been performed for two cases (see Fig. 4.21). In the first case, we have shifted the entire activity belt in latitude, while in the second case we

have changed the range of emergence latitudes while keeping the average emergence latitude of all BMRs in a cycle fixed. This corresponds to changing the slope of the mean emergence line in the butterfly diagram. In order to obtain clear trends, the width of the distribution around the mean emergence line has been set to $\sigma = 1°$. Subsequently, the spread σ around the mean latitudes has also been varied.

Shift of the emergence latitudes (case 1)

A poleward shift of the activity belt in general leads to higher polar field strengths (Fig. 4.22 b). The BMRs emerge closer to the pole and thus the time for reaching it by diffusion and meridional advection is shorter and therefore cancellation through diffusion is reduced. Also, higher emergence latitudes result in higher tilt angles of the BMRs which lead to a higher $B_{\rm pole}$ (see Sect. 4.4.8). A slight increase in the polar field is given when the activity belt is shifted equatorward relative to the standard case. In this case, diffusion over the equator enhances cancellation of leading polarity, and increasing distance from the equator decreases this cancellation.

The total surface field exhibits a stronger contrast between cycle maximum and minimum with increasing emergence latitude (Fig. 4.22 a). At cycle maximum increasing latitude of emergence decreases the amount of cross-equatorial cancellation between leading polarities, leading to a larger amount of flux at maximum. This effect is most important as long as emergence latitudes are small. But why is there less field at minimum? Possibly: With less cross-equator cancellation more cancellation between fluxes in the same hemisphere takes place ($B_{\rm tot,min}$ is like a mirror of $B_{\rm tot,max}$).

Range of emergence latitudes (case 2)

Changing the slope of the wings of the butterfly diagram leaves the average tilt angle of the BMRs unchanged, thus not having a strong effect on the surface field (Fig. 4.23 a) and also not on the polar fields (Fig. 4.23 b). The difference in the field strength between the extreme cases, i.e. constant emerging latitudes over the cycle and a strong decrease from $\theta_{\rm in} = 45°$ at the beginning to $\theta_{\rm fi} = 0°$ at the end of the cycle, is only about $3\,$G for the polar field. This indicates that the two effects described in the previous paragraph, i.e. fast approach of the poles for polarities emerging at high latitudes and high diffusion across the equator for flux emerging at low latitudes, roughly compensate. Cancellation in the polar region reduces the polar field, while cancellation across the equator supports a higher polar field.

Spread around the mean (case 3)

Both the total surface field and the polar fields are remarkably independent of the statistical spread of BMRs around the mean. There is no noteworthy change in the field strengths ($< 10\%$) if the standard deviation is increased from 0 to $20°$.

4.4.10 Asymmetric activity cycles

In the previous sections, the simulated activity cycle was always symmetric in time with respect to the cycle maximum. However, the sunspot record shows that the solar maxi-

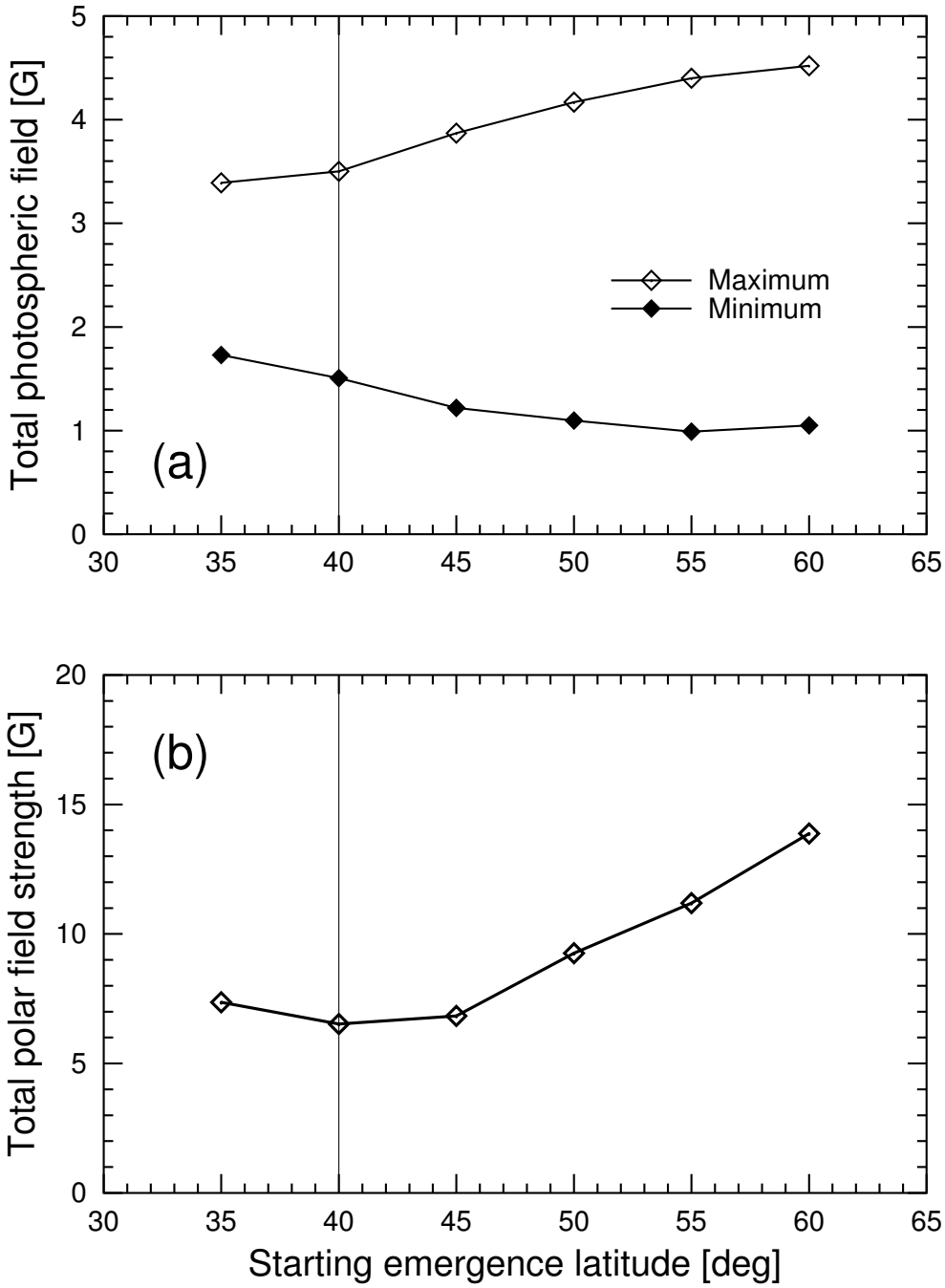

Figure 4.22: (a) $B_{\mathrm{tot,max}}$ and $B_{\mathrm{tot,min}}$ vs. starting mean emergence latitude. (b) Polar field strength vs. starting latitude.

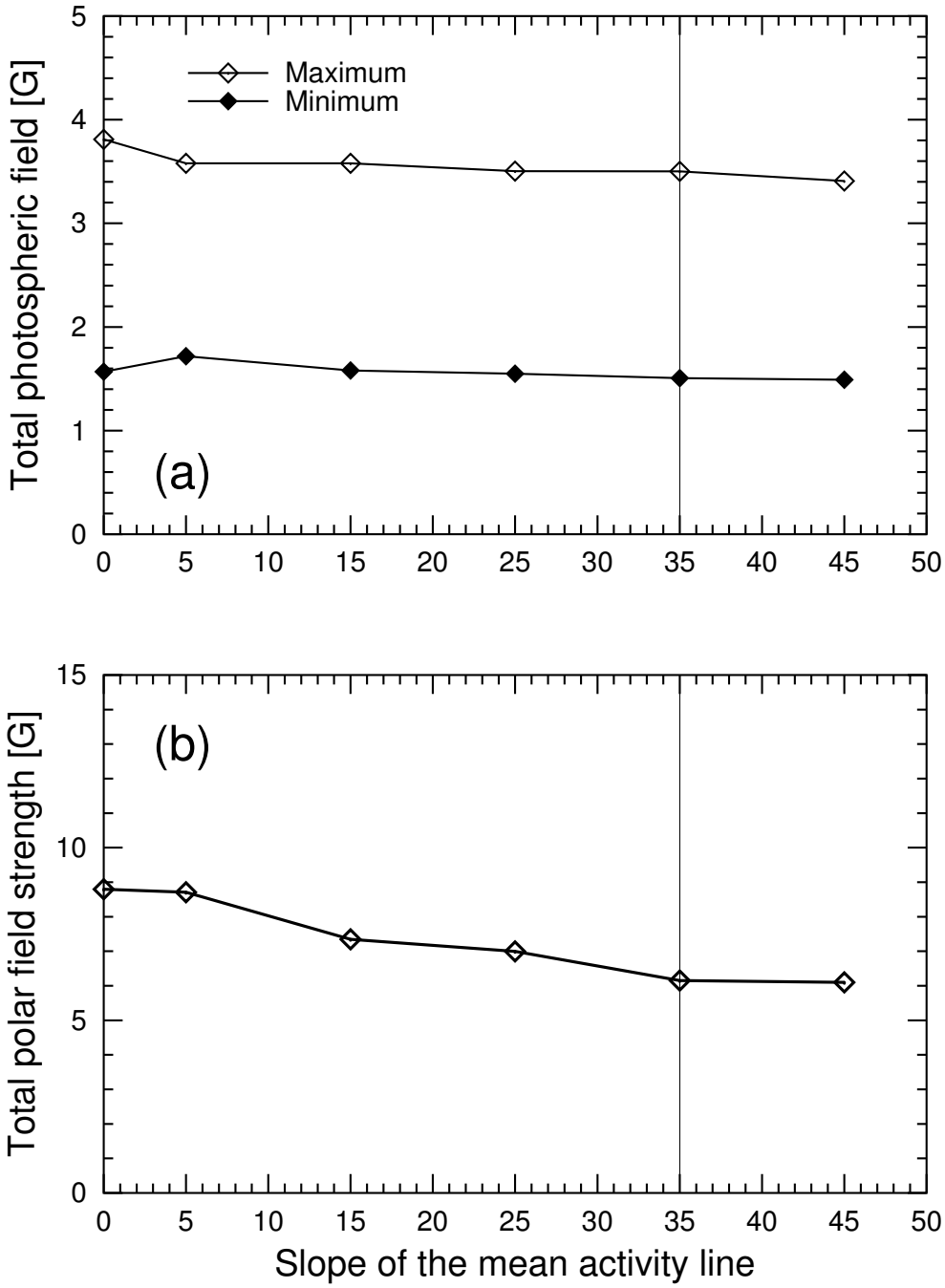

Figure 4.23: (a) $B_{\mathrm{tot,max}}$ and $B_{\mathrm{tot,min}}$ vs. slope $\theta_{\mathrm{in}} - \theta_{\mathrm{fi}}$ of the mean activity line at cycle maximum and minimum. (b) Polar field strength vs. slope of the mean activity.

mum is reached already well in the first half of most cycles. In order to study asymmetric cycles we have considered the following class of time profiles of flux emergence: a linear increase until the maximum followed by a linear decrease to zero. The corresponding emergence rates of BMRs have been adjusted such that the total number of BMRs during a cycle remains constant and equal to the previously used Gaussian profile. The times of activity maxima can now be varied between 1 and 12 years after the beginning of a cycle. It turns out that the total surface field as well as the maximum value of the polar field do not depend significantly on the time of the cycle maximum. Both quantities vary by less than 15%. Fig. 4.24 shows the polar field strength for the case when the activity maximum is reached after 2 and after 11 years, respectively. In the first case, the high initial emergence rate coupled with the large tilt and high emergence latitude of the BMRs early in the cycle leads to an early polar reversal and a fast build-up of the polar fields. The new maximum of $B_{\rm pole}$ is built up within 3 years. After the maximum of the emergence rate, the amount of net flux reaching the poles decreases rapidly as both the emergence rate and the tilt angles of the BMRs decrease. It appears to be just sufficient to maintain the polar field, which leads to a roughly rectangular time profile of the polar fields. In contrast, when the activity peaks very late in the cycle, i.e. at low latitudes, the polar field reversal takes place over a longer period of time resulting in a sharp maximum of polar field strength.

4.4.11 Shape of activity profile

Except for the last section, the activity profile was taken to be Gaussian in shape. Here we consider the influence of the functional form on the global field by comparing three different types of activity profiles. Alternatively to the Gaussian profile we apply a linear form of activity as described in the preceding section with the maximum in the middle of the cycle as well as a sinusoidal one. The total amount of BMRs per cycle, i.e. the amount of emerging flux integrated over the activity curve for one cycle, is held constant. Table 4.2 shows $B_{\rm tot}$ and $B_{\rm pole}$ for the three cases.

A linear increase and decrease of the activity leads to smaller $B_{\rm tot,max}$ and higher $B_{\rm tot,min}$ compared with the Gaussian profile. In the latter case, the cycle maximum is wider than in the linear case, which explains the higher $B_{\rm tot,max}$. In contrary, during cycle minimum, where an overlap of two cycles is present, the superposition of two linear cycle activities is larger for the linear profile than for the Gaussian profile, for which the overlap of two cycles nearly vanishes.

The sinusoidal profile gives an emergence pattern in between the two other discussed cases, so that $B_{\rm tot,max}$ and $B_{\rm tot,min}$ have intermediate values. The polar field does not vary significantly with the shape of the profile in all three cases.

4.4.12 Phase relation between the activity cycle and polar fields

The polar fields reverse around cycle maximum. A more precise determination of the time lag between BMR emergence rate and polar field reversal can be obtained by shifting and cross-correlating both time series. The maximum correlation coefficient indicates the phase difference. This method has been applied to all of the above discussed parameter

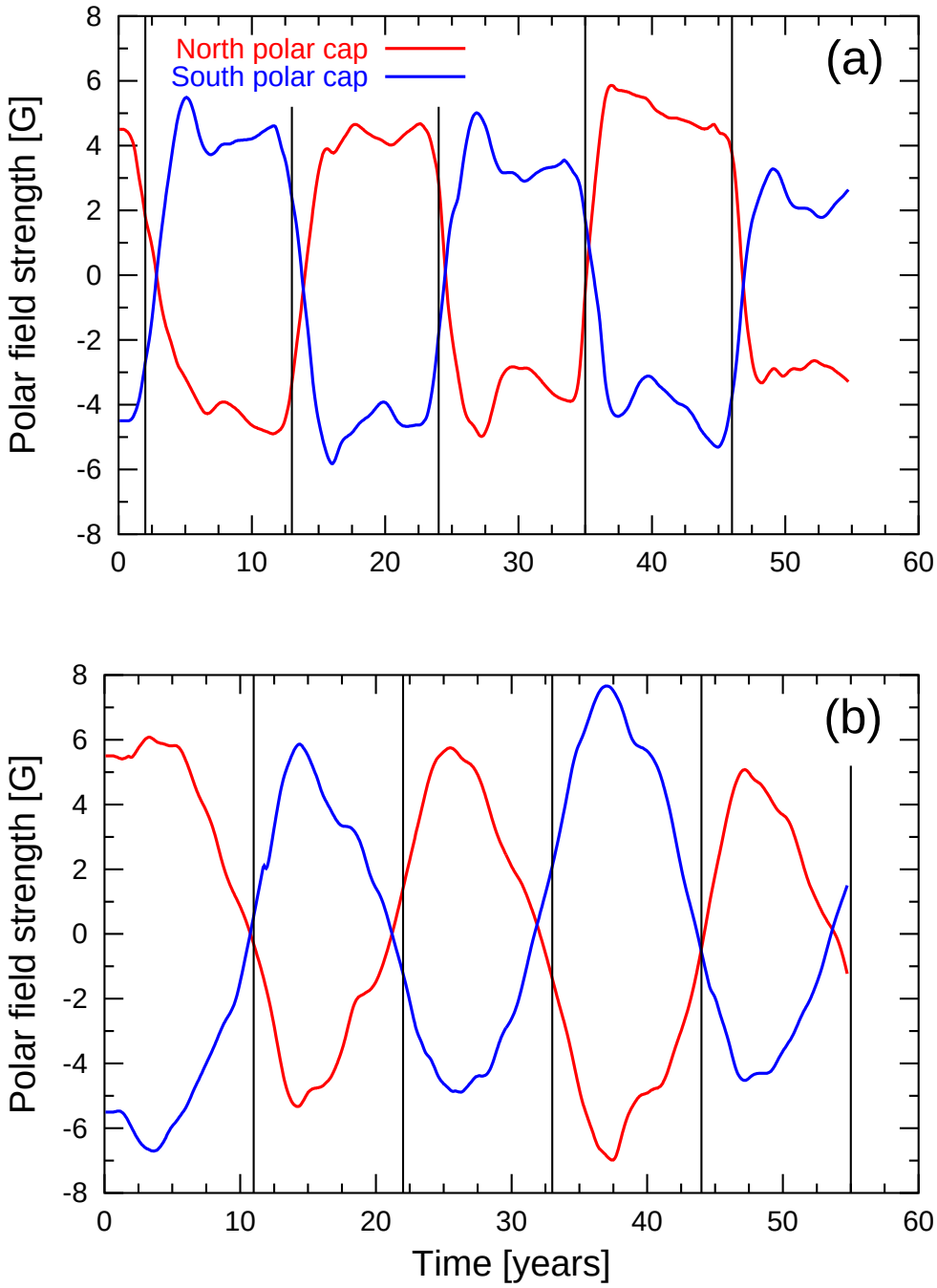

Figure 4.24: Time evolution of the polar fields when the evolution of the emergence rate is described by 2 straight lines. The activity maximum, marked by the vertical lines, is reached after (a) 2 years and after (b) 11 years, respectively.

Table 4.2: Dependence of the total field and the polar field on the functional form of the activity cycle.

activity profile	$B_{\mathrm{tot,max}}$ [G]	$B_{\mathrm{tot,min}}$ [G]	B_{pole} [G]
Gaussian	3.4	1.5	6.2
linear	2.6	1.9	5.5
sinusoidal	2.9	1.8	5.0

sets. It turns out that for all cases the polar fields reverse within ± 0.5 years of cycle maximum.

4.5 Conclusion

We have considered the large-scale evolution of the magnetic field arising from the flux transport model for a variety of parameters. Two types of parameters can be distinguished: model parameters, i.e. diffusion coefficient, meridional flow and differential rotation, which influence the flux transport, and parameters that influence the source term in Eq. (4.1). The latter control the emergence rate, emergence latitudes and emergence time of new BMRs. We have carried out a detailed study of the dependence of relevant properties on the large-scale surface field on these parameters. This has helped us to distinguish the parameters having a large influence on global magnetic properties from those playing a smaller role. The average tilt angle of the BMRs, the diffusion coefficient and the level of activity, i.e. the total emergent flux, have a particularly large effect on the polar field and the total unsigned flux. The meridional flow velocity and the cycle length have a large influence on the formation of the polar field. The overlap time of consecutive cycles leads to the formation of a background field (field during cycle minimum).

The parameter study should help in particular to get a better understanding of the behaviour of the large-scale field on the Sun at different times and at different activity levels. We also expect it to provide a guide for future studies of the magnetic field evolution on cool stars.

5 A necessary extension of the surface flux transport model

5.1 Introduction

Flux transport models aim at describing the evolution of the solar surface flux distribution. Bipolar magnetic regions emerge from the solar interior and the transport of the corresponding radial magnetic flux by horizontal flows due to convection, differential rotation and meridional flow is followed in time, e.g. (Leighton 1964, DeVore et al. 1984, Wang et al. 1989b, van Ballegooijen et al. 1998, Schrijver 2001, Baumann et al. 2004). Despite the success of flux transport models in explaining the Sun's large-scale magnetic field pattern, they fail in reproducing the correct polar flux and the Sun's open magnetic flux of the last cycles. The conceptual deficiency in flux transport models arises from ignoring diffusion in radial direction. The consequence is an artificial dynamo effect. For example, a dipolar axisymmetric magnetic field can be maintained permanently by a balance between advection through a meridional flow and horizontal diffusion. As a consequence, a standard flux transport model fails to reproduce the evolution of the polar flux when applied to many cycles.

Missing processes in flux transport models are flux loss from the surface by (1) retraction of $\cap$-loops, (2) the emergence of $\cup$-loops and (3) radial diffusion. (1) and (2) involve radial velocities which are not included in surface flux transport models, but can at least crudely be described by radial diffusion.

Dikpati and Choudhuri (1994) have avoided these problems with the surface flux transport model by considering flux transport of an axisymmetric field in the meridional plane by a meridional circulation and turbulent diffusion. However, this comes at the price of ignoring the longitudinal structure of the magnetic field. Key properties like the tilt angle of bipolar magnetic regions have therefore to be introduced in an ad-hoc fashion in their model (Choudhuri and Dikpati 1999).

In order to obtain a better reproduction of the historical records, Schrijver et al. (2002) proposed an additional exponential decay term in the surface flux transport model. Wang et al. (2002) varied the meridional flow in their simulations by increasing the poleward flow amplitude during the more active cycles in order to obtain stable oscillations of the Sun's polar field.

In this chapter we derive a term parametrising the radial diffusion processes in the surface flux transport model. To this end, we consider the diffusion problem in a spherical shell and determine the decay term from the decay modes. The calibration of the new parameter is then done by comparing the simulations with observations.

The outline of the chapter is as follows. In Sect. 5.2 we discuss the decay modes in a spherical shell for appropriate boundary conditions for the solar convection zone. In Sect. 5.3 we derive a decay term for the surface flux transport model based on the decay modes. In Sect. 5.4 we present first applications of the radial decay term. Finally, in Sect. 5.5 we summarize our results.

5.2 Decay modes of a poloidal field in a spherical shell

The time evolution of the magnetic field is described by the induction equation which reduces in the absence of flows to the diffusion equation

$$\frac{\partial \mathbf{B}}{\partial t} = -\eta \, \nabla \times (\nabla \times \mathbf{B}) \,, \tag{5.1}$$

where η is the magnetic diffusivity. The magnetic field $\mathbf{B}_{\rm tot}$ can be split into a poloidal part and a toroidal part. The flux transport model assumes a purely radial magnetic field at the solar surface, which is supported by observations (Martinez Pillet et al. 1997). Therefore, the surface field is purely poloidal. Any toroidal field in the Sun's interior affects the surface only through flux emergence, whereby it is assumed to be instantaneously transformed into a poloidal field at the surface. Therefore, only the evolution of the poloidal magnetic field in a spherical shell (representing the convection zone) needs to be considered.

In the following, $\mathbf{B}$ symbolizes the poloidal field. Because of the separation of the field, the diffusion equation (Eq. 5.1) is valid for the poloidal field alone. As a result of the solenoidality, any poloidal magnetic field can be represented by a scalar function S (Bullard and Gellman 1954, Krause and Rädler 1980)

$$\mathbf{B} = -\nabla \times (\mathbf{r} \times \nabla S) = -\mathbf{r} \triangle \, S + \nabla \frac{\partial}{\partial r}(rS) \,, \tag{5.2}$$

where $\triangle$ is the Laplace-operator in spherical coordinates. Inserting this field representation in the diffusion equation for the poloidal field, Eq. (5.1), leads to

$$\begin{aligned} -\nabla \times \left(\mathbf{r} \times \nabla \, \frac{\partial S}{\partial t} \right) &= \eta \, \nabla \times \nabla \times \nabla \times (\mathbf{r} \times \nabla S) \\ &= \eta \, \nabla \times \nabla \times (\mathbf{r} \times \triangle S) \\ &= -\eta \, \nabla \times (\mathbf{r} \times \nabla \triangle S) \;, \end{aligned} \tag{5.3}$$

where we have used $\nabla \times \mathbf{r} = 0$. From Eq. (5.3) it follows that

$$\mathbf{r} \times \nabla \left[\eta \triangle S - \frac{\partial S}{\partial t} \right] = 0 \,. \tag{5.4}$$

We introduce a spherical polar coordinate system with the coordinates r, θ and ϕ whose origin is located in the center of a conducting sphere with radius R. The vector potential, $-\mathbf{r} \times \nabla S$, is invariant under gauge transformations, so that S can be chosen such that the normalization condition

$$\int_{-1}^{1} \int_{0}^{2\pi} S \; d(\cos\theta) \; d\phi = 0 \tag{5.5}$$

is fulfilled for any r. Let Ω be the angular part of the spherical Laplace-operator,

$$\begin{aligned} \triangle S &= \frac{1}{r^2}\left[\frac{\partial}{\partial r}\left(r^2\frac{\partial S}{\partial r}\right)\right. \\ &+ \left.\frac{1}{\sin\theta}\frac{\partial}{\partial\theta}\left(\sin\theta\frac{\partial S}{\partial\theta}\right)+\frac{1}{\sin\theta}\frac{\partial^2 S}{\partial\phi^2}\right] \\ &\equiv \frac{1}{r^2}\left[\frac{\partial}{\partial r}\left(r^2\frac{\partial S}{\partial r}\right)+\Omega S\right], \end{aligned} \tag{5.6}$$

then it follows for any S

$$\int_{-1}^{1}\int_{0}^{2\pi}\Omega S\; d(\cos\theta)\; d\phi = 0\,. \tag{5.7}$$

From Eqs. (5.5)−(5.7) we have

$$\int_{-1}^{1}\int_{0}^{2\pi}\triangle S\; d(\cos\theta)\; d\phi = 0\,. \tag{5.8}$$

Using Eq. (5.8), it follows from Eq. (5.4) that

$$\eta\triangle S - \frac{\partial S}{\partial t} = 0\,. \tag{5.9}$$

Eq. (5.9) can be uniquely solved by introducing appropriate boundary conditions. As discussed above, the field is assumed to be radial at the surface of the considered sphere. Thus the upper boundary condition is $B_\theta = 0$, or

$$\frac{\partial(rS)}{\partial r} = 0 \qquad \text{at} \quad r = R_\odot\,. \tag{5.10}$$

The bottom of the convection zone borders to the radiative core, which is assumed to be an ideal conductor. The boundary condition therefore is

$$\frac{\partial S}{\partial\theta} = 0 \qquad \text{at} \quad r = r_b\cdot R_\odot\,, \tag{5.11}$$

with $r_b = 0.7$.
The solution of Eq. (5.9) with the boundary conditions Eqs. (5.10) and (5.11) is given by

$$S(r,\theta,\phi,t) = \sum_{n=0}^{\infty}\sum_{l=1}^{\infty}\sum_{m=-l}^{l} R_l^n(r)\; Y_{lm}(\theta,\phi)\; T_l^n(t)\,, \tag{5.12}$$

where we have omitted the monopole term and also separated the time dependence. The solution Eq. (5.12) corresponds to a decomposition into orthogonal decay modes (Elsasser 1946). The field lines for some low order decay modes are shown in Fig. 5.1.

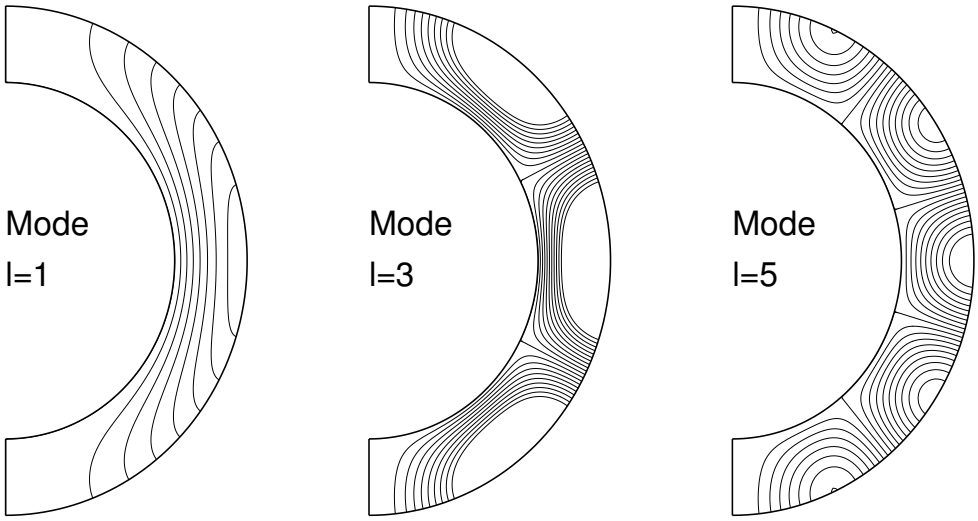

Figure 5.1: Meridional cut through the convection zone showing the fieldlines of the decay modes with $l = 1$, $l = 3$ and $l = 5$.

The time dependent part of Eq. (5.12) can be solved by assuming an exponential decay

$$T_l^n(t) = e^{-\eta\, k_{ln}^2 t/R_\odot^2}\,. \tag{5.13}$$

The eigenvalues of the spherical harmonics are

$$\triangle_h\, Y_{lm}(\theta,\phi) = -\frac{l\,(l+1)}{R_\odot^2}\, Y_{lm}(\theta,\phi)\,, \tag{5.14}$$

so that for the radial part remains

$$r^2\frac{\partial^2 R_l^n}{\partial r^2} + 2r\frac{\partial R_l^n}{\partial r} + \Big[k_{ln}^2 r^2 - l(l+1)\Big] R_l^n = 0\,, \tag{5.15}$$

which is the spherical Bessel differential equation whose general solution is

$$R_l^n(r) = a_{ln}\; j_l(k_{ln}r) + b_{ln}\; y_l(k_{ln}r)\,. \tag{5.16}$$

j_l and y_l are the spherical Bessel functions of the first and second kind, respectively, of order l. a_{ln} and b_{ln} can be determined using the lower boundary condition Eq. (5.11). Without loss of generality one can set $a_{ln} = 1$ and then find $b_{ln} = -j_l(k_{ln}r_b)/y_l(k_{ln}r_b)$. Combining this with the upper boundary condition Eq. (5.10) leads to

$$\begin{aligned} &l\Big[j_l(k_{ln})\; y_l(k_{ln}r_b) - j_l(k_{ln}r_b)\; y_l(k_{ln})\Big] \\ &-k_{ln}\Big[j_{l-1}(k_{ln})\; y_l(k_{ln}r_b) - j_l(k_{ln}r_b)\; y_{l-1}(k_{ln})\Big] = 0 \end{aligned} \tag{5.17}$$

from which the eigenvalues k_{ln} can be determined. The index n represents the number of nodes in radial direction, l is the total number of nodes on a sphere and m is the number of nodes passing through the poles of a sphere. It should be noted, that the eigenvalues of the time dependence, k_{ln}, do not depend on the index m.

5.3 Extension of the surface flux transport model

We use the results obtained in Sect. 5.2 to extend the surface transport model (DeVore et al. 1985a, Wang et al. 1989a) by a decay term aimed at describing the radial derivatives in the diffusion term. We write the extended surface transport equation as

$$\begin{aligned}\frac{\partial B_r}{\partial t} &= -\omega(\theta)\frac{\partial B_r}{\partial \phi} - \frac{1}{R_\odot \sin\theta}\frac{\partial}{\partial \theta}\left(v(\theta) B_r \sin\theta\right) + S'(\theta,\phi,t) \\ &+ \frac{\eta_h}{R_\odot^2}\left[\frac{1}{\sin\theta}\frac{\partial}{\partial\theta}\left(\sin\theta\frac{\partial B_r}{\partial\theta}\right) + \frac{1}{\sin^2\theta}\frac{\partial^2 B_r}{\partial\phi^2}\right] - D(\eta)\,, \end{aligned} \tag{5.18}$$

where $\omega(\theta)$ is the angular velocity of the photospheric plasma, $v(\theta)$ is the meridional flow velocity on the solar surface, $S'(\theta,\phi,t)$ is a source term describing the emergence of new magnetic flux, η_h is the effective diffusion coefficient associated with the non-stationary supergranular motions on the surface and $D(\eta)$ is the added term, which is further specified below.

Our aim is to determine the value of η in the surface transport model by considering the decay of the eigenmodes in a spherical shell (Sect. 5.2). To this end, we expand the surface magnetic field into spherical harmonics

$$B_r\left(R_\odot,\theta,\phi,t\right) = \sum_{l=1}^{\infty}\sum_{m=-l}^{m=+l} a_{lm}(t)\, Y_{lm}\left(\theta,\phi\right)\,. \tag{5.19}$$

We now consider a pure diffusion problem and define $D(\eta)$ as

$$\begin{aligned} D(\eta) &= \sum_{l=1}^{\infty}\sum_{m=-l}^{m=+l} D_{lm}(\eta) \\ &= \sum_{l=1}^{\infty}\sum_{m=-l}^{m=+l} \frac{a_{lm}(t)}{\tau_l}\, Y_{lm}\left(\theta,\phi\right)\,. \end{aligned} \tag{5.20}$$

where τ_l are the decay times of the individual modes. The decay times are degenerated with respect to the azimuthal number m. From Eqs. (5.18) to (5.20) we then have

$$\frac{\partial}{\partial t}\left[a_{lm}(t)\, Y_{lm}\right] = -\frac{a_{lm}(t)}{\tau_l}\, Y_{lm}\left(\theta,\phi\right)\,. \tag{5.21}$$

The solution for $a_{lm}(t)$ is an exponential function

$$a_{lm}(t) = e^{-t/\tau_l}\,. \tag{5.22}$$

In the meridional transport equation the time dependence is given by Eq. (5.13), where we have also used an expansion into spherical harmonics. The index l is in both models the same, so that the decay times τ_l can be related to η by equating Eqs. (5.22) and (5.13)

$$\tau_l(\eta) = R_\odot^2\left[\eta\, k_{l0}^2\right]^{-1}\,. \tag{5.23}$$

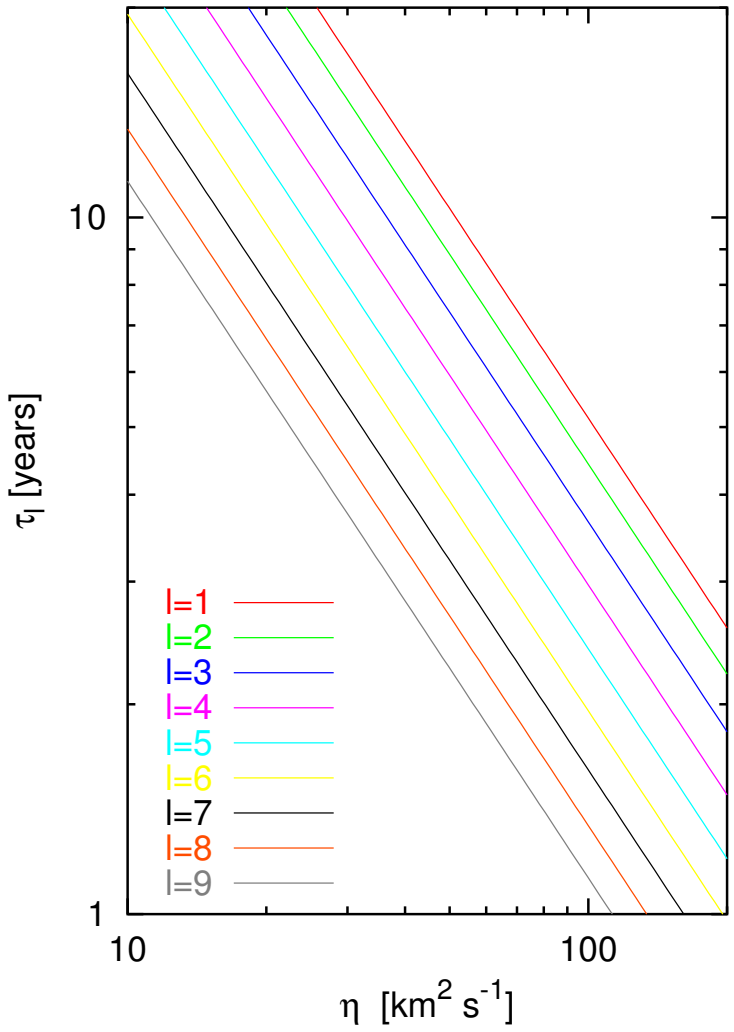

Figure 5.2: Dependence of the decay times τ_l of the harmonic components of the surface field on the radial diffusivity η. Shown are the modes from $l = 1$ to $l = 9$ for a physically reasonable range of η (n=0).

We consider only modes with $n = 0$, since the surface transport model has no information about the detailed depth structure. Therefore, the diffusivity η entering τ_l is taken as a free parameter, which has to be adjusted according to observations.

Fig. (5.2) shows the dependence of τ_l on η for several l. For a given η, the decay time τ_l becomes shorter for increasing l. The higher modes represent the small scale features which decay faster than the large-scale pattern, represented by modes with small l values. A value of $\eta = 100\,\mathrm{km^2\ s^{-1}}$ corresponds to a decay time of ~ 5 years for the mode $l = 1$, i.e. the dipole component. Schrijver et al. (2002) also used an exponential decay term in order to extend the flux transport model, however, we are able to refer this term to the horizontal structure of the eigenmodes.

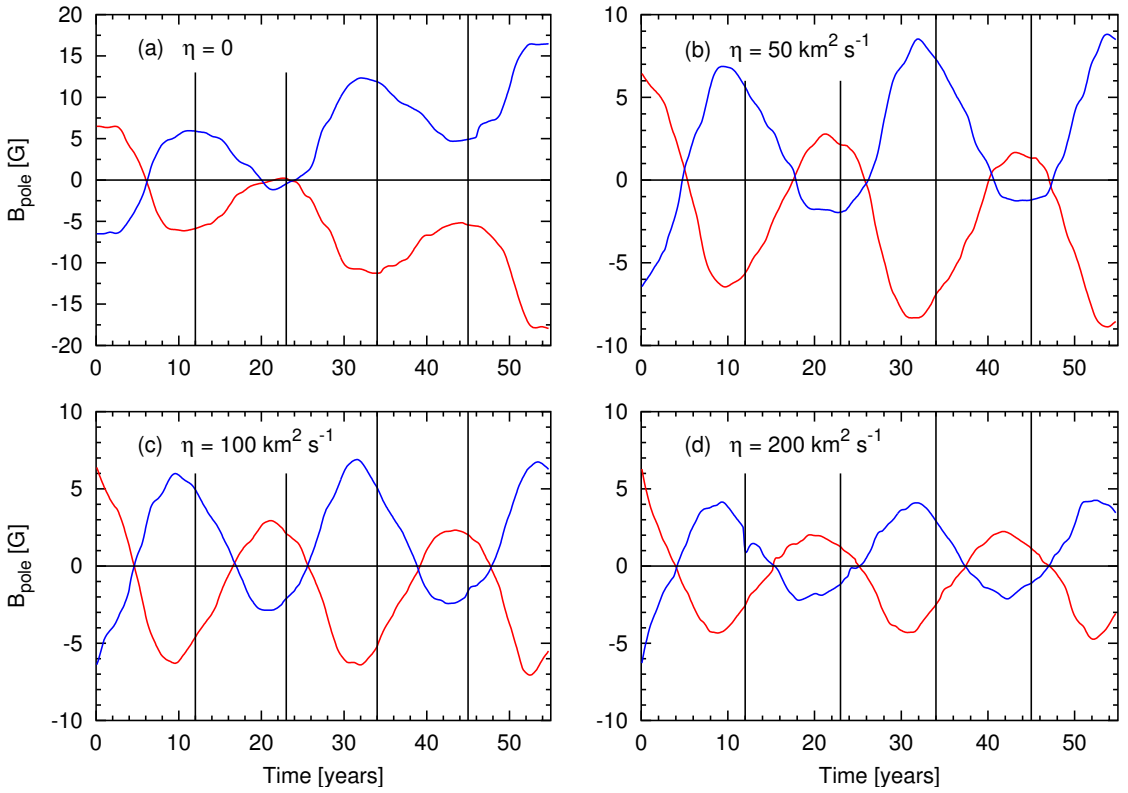

Figure 5.3: Evolution of the north (*red line*) and south polar fields (*blue line*) for asymmetric cycle strengths for four different values of η. The vertical lines indicate the activity minima.

5.4 Applications

5.4.1 Cycles of varying strength

In the previous section we have derived a decay term which extends the surface flux transport model and leads to modified decay rates of the harmonic components of the surface field. As an example of the effect of the new parameter η, we consider simulations of an artificial set of solar cycles which differ in strength. We generate a synthetic butterfly diagram similar to the reference case described in Baumann et al. (2004) but with a systematic difference in strength between odd and even cycles. To this aim we reduce the amount of new emerging bipolar magnetic regions per cycle, i.e. the activity, in every second cycle by a factor of 2. The new decay term in the transport model should lead to a stabilization of the polar cap field oscillations.

The results for the polar fields for the unmodified model, i.e. $\eta = 0$, and for several values of η are shown in Fig. 5.3. The polar field, $B_{\rm pole}$, is the averaged field over the polar cap down to 15° pole distance. Without the additional field decay due to radial diffusion, the polar fields diverge (Fig. 5.3 a). During the weaker cycles the flux supply is insufficient to cancel the existing polar field, to reverse it and to build up a new polar field of opposite polarity and of the same strength as before. The strength of the polar field scales linearly with the total amount of emerged flux (Baumann et al. 2004). After a few cycles, the

odd-even asymmetry leads to a runaway of the polar fields because the weaker cycles are not able to counter-balance the flux remaining from the stronger cycles. Switching on radial diffusion cures that problem (Fig. 5.3 b - d). A diffusion rate $\eta = 50\,\mathrm{km}^2\ \mathrm{s}^{-1}$ is too small to counter-act the strong cycle asymmetries and the runaway effect of the polar fields is still present, however much weaker than before. Setting $\eta = 100\,\mathrm{km}^2\ \mathrm{s}^{-1}$ results in stable oscillations of the polar fields around 0, whereas the polar field strength is larger for stronger cycles and smaller for smaller cycles. A value of $\eta = 200\,\mathrm{km}^2\ \mathrm{s}^{-1}$ shows the same qualitative behaviour as in the case of $\eta = 100\,\mathrm{km}^2\ \mathrm{s}^{-1}$, but the absolute values of the polar field is reduced owing to the stronger damping.

The fact that the diffusivity for the surface transport is larger than the diffusivity parameter η for the volume diffusion reflects the difference in length scales between the radial and the horizontal directions.

5.4.2 Polar reversal times

We now consider cycles of equal strength and investigate the reversal times of the polar field in dependence on the parameter η. Fig. 5.4 a shows the dependence of the total surface field reached during activity maximum and minimum, respectively, on η. The total surface field is obtained by integrating the absolute value of the field strength over the solar surface

$$B_{\mathrm{tot}} = \frac{1}{4\pi} \int |B_r(R_\odot, \theta, \phi)| \mathrm{d}\Omega \,. \tag{5.24}$$

During activity maximum, the total field, $B_{\mathrm{tot,max}}$, remains roughly constant as η varies, while the field during activity minimum, $B_{\mathrm{tot,min}}$, slightly decreases. During activity minimum, the field is dominated by the dipole mode. η leads to a decay of this dipole and so the polar field is weakened (Fig. 5.4 b). The enhanced decay of the existing polar fields as η increases and less new flux reaching the pole, balance, so that $B_{\mathrm{tot,max}}$ remains roughly unchanged. It is interesting to consider the reversal times of the polar field which are shifted relative to the activity cycle by the new diffusion term (Fig. 5.4 c). Makarov et al. (2003) found that the reversals of the magnetic dipole configuration occurs on average 3.3 years after sunspot minimum. We analysed the reversal time lag by cross-correlating the polar field with the total surface field. The parameter η leads to a shorter time until the maximum polar field is reached, which can be explained by the enhanced dipole decay. A value $\eta = 100\,\mathrm{km}^2\ \mathrm{s}^{-1}$ reproduces well the observed time lag between cycle minimum and polar reversal. However, care must be taken because we are analysing a synthetic dataset which does not include cycle fluctuations as is the case for real data. In summary, we can say that B_{pole} is decreased and reaches its maximum earlier, i.e. a few years after activity minimum, by applying the new decay term.

5.4.3 Comparison with observations

Direct observations of the Sun's surface magnetic field are available from NSO/KP synoptic maps since 1976. The longitude averaged magnetic field from this observations is shown in Fig. 5.5 a. We modelled the evolution of the surface field for the same period using the USAF/NOAA sunspot database. A detailed explanation how we transformed the sunspot record into magnetic input sources for our simulations is given in

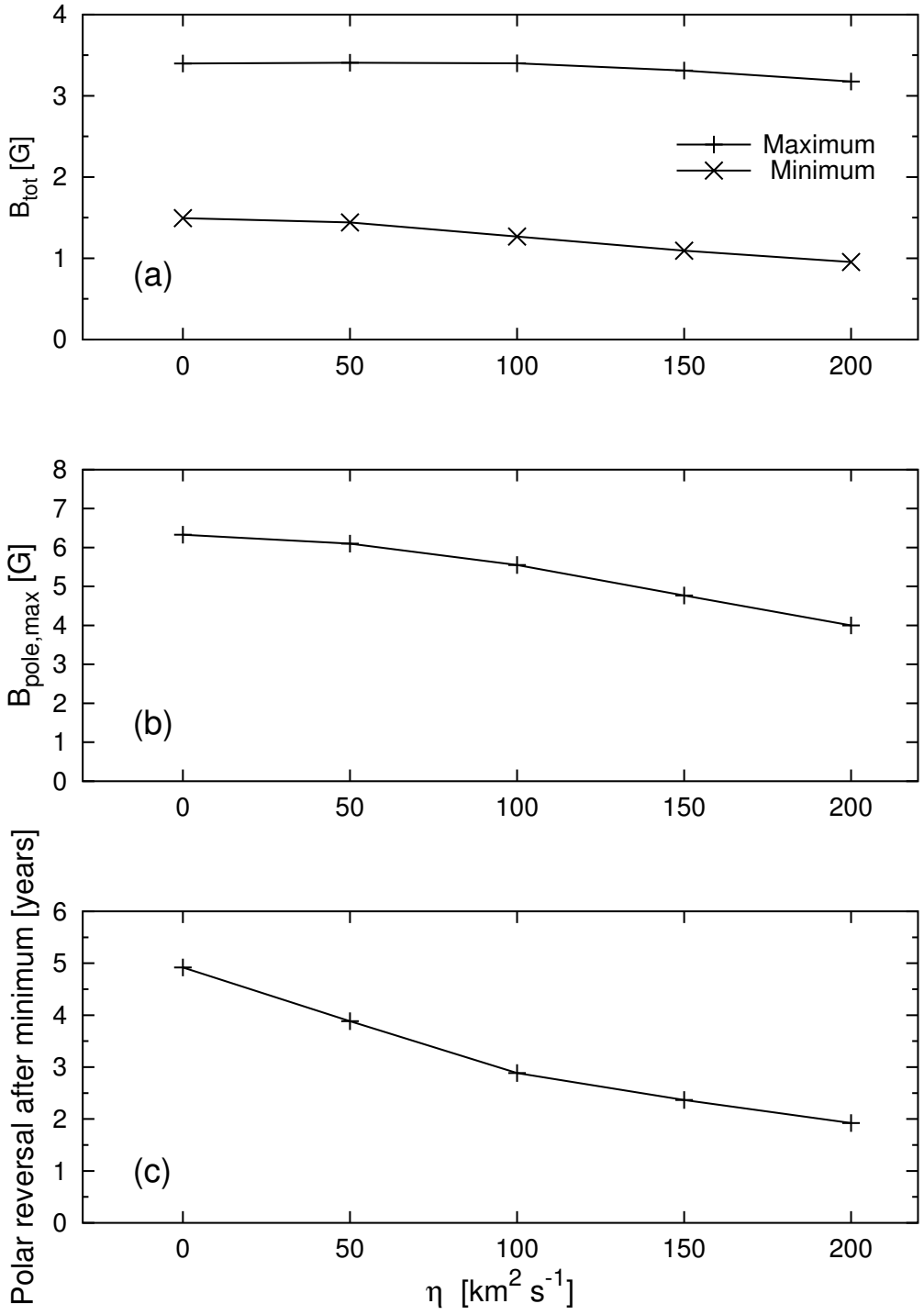

Figure 5.4: Dependence of the (a) total surface field $B_{\rm tot}$ during activity maximum and minimum, respectively, and the (b) maximal reached polar field $B_{\rm pole,max}$ on η. (c) Polar reversal times after activity minimum derived from cross-correlating the polar field and the total field.

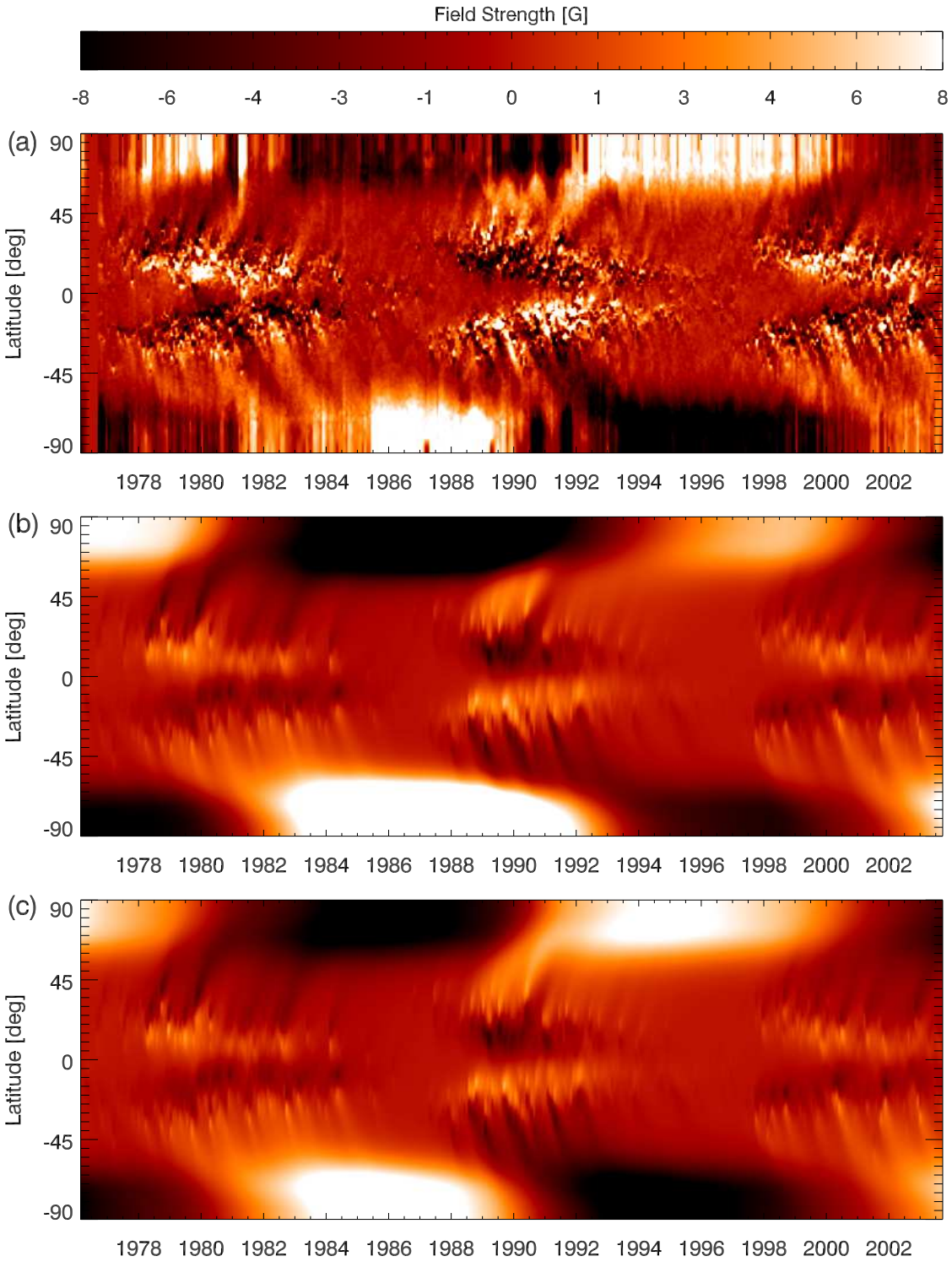

Figure 5.5: Longitude averaged magnetic butterfly diagrams. (a) Observation (NSO/KP), Courtesy D. Hathaway, NASA, Marshall Space Flight Center, (b) simulation with $\eta = 0$ and (c) $\eta = 100\,\mathrm{km}^2\,\mathrm{s}^{-1}$.

Sect. 6.6.1. The resulting model magnetic butterfly diagrams for the case when $\eta = 0$ and $\eta = 100\,\mathrm{km}^2\,\mathrm{s}^{-1}$ are shown in Fig. (5.5 b and c). Both simulations model the observed diagram rather well. However, there are differences especially in the polar fields. The reversal times of the polar fields are better represented by the extended model ($\eta = 100$). The direct comparison of the surface field calculations with the observations of the same time period gives further evidence supporting the improvement of the flux transport model.

5.5 Conclusion

We have investigated the decay of the eigenmodes of the diffusion equation. The boundary condition, that the field becomes radial at the surface, allows us to connect the spherical shell model with the surface flux transport model quantitatively. We can assign realistic radial diffusion rates to an additional decay term in the surface transport model. The exponential decay of magnetic flux on the Sun on a timescale of $5 - 10$ years was already proposed by Schrijver et al. (2002). The additional decay of magnetic flux is necessary to model realistically long-term trends of solar activity, like the polar field evolution or the open flux over several cycles. Based on our work we can now assign physical processes, i.e. radial diffusion, to the decay of the magnetic field on the photosphere. The surface flux transport model is, except for new emerging magnetic sources, a closed system within the photosphere. Interactions of magnetic flux between different layers of the solar convection zone or of the heliosphere, are not included. We now have a tool which helps us to include the vectorial character of the magnetic field in the transport model using a single parameter, η. Surely, this will not be enough to account for all the complicated reconnection processes occurring in the solar atmosphere, however, we expect the new term in the transport model to improve modeling the observed large-scale magnetic field evolution.

6 Modelling the open magnetic flux from the Greenwich sunspot group record

6.1 Introduction

The interplanetary magnetic field (IMF) has its origin in the so-called coronal holes, which are magnetically open regions on the Sun. In these open regions the solar wind, consisting of electrically well conducting plasma, drags the magnetic field lines into the heliosphere. During sunspot minimum, the open magnetic flux has its origin in the polar regions, while during cycle maximum the coronal holes form at low latitudes with rather small areas but high field strengths.

Wang et al. (2000a) extrapolated NSO Carrington maps out to a source surface and found that the open flux lags the sunspot cycle by 1-2 years while its amplitude varies by a factor of 2 only between sunspot minimum and maximum in contrast to the much larger variations (factor of $\sim 3-4$) of the Sun's total flux (Wang and Sheeley 2002, Krivova and Solanki 2004). The same result was found earlier by Slavin et al. (1986) analysing IMF observations for cycle 21.

Measurements from the *Ulysses* space craft have shown that the strength of the radial IMF component $|B_r|$ is independent of heliospheric latitude (Smith and Balogh 1995). Thus the heliospheric currents are confined to a thin current sheet in the equatorial plane during solar activity minimum (Hoeksema et al. 1983). During maximum the current sheet can extend up to 60°.
At a distance of 1 AU, the radial IMF component is a few nT and it has been found that the interplanetary magnetic field strength has doubled on average over the last century (Lockwood et al. 1999). The magnetic field transported by the solar wind reconnects with the Earth's magnetic field. The interaction of protons and electrons with molecules in the Earth's upper atmosphere leads to phenomena like aurorae. The IMF represents one potential link of solar activity with the Earth's climate and thus its variation is believed to have important terrestrial effects.

Simulations using a flux transport model were not able to reproduce the right phase relation between the surface magnetic field and the open flux. In these simulations the open flux is closely related to the low-order multipoles, mainly the dipole component, of the surface field (Wang et al. 2000a, Mackay et al. 2002b). This relation leads to a maximum amount of open flux during sunspot minimum. However, this evolution of the open flux in antiphase with the solar cycle is inconsistent with observations. Our

aim is to improve the model in order to obtain a better match between model and the observations. This concerns specifically the relationship between open flux and surface flux (phase relation and absolute values).

6.2 The source surface model

The solution of the Laplace equation (2.39) for the domain $r \geq R_\odot$ with the boundary condition $\psi(r \to \infty, \theta, \phi) = 0$ in spherical coordinates is

$$\psi(r,\theta,\phi) = R_\odot \sum_{l=0}^{\infty} \sum_{m=-l}^{l} \left(\frac{R_\odot}{r}\right)^{l+1} a_{lm}\, Y_{lm}(\theta,\phi)\,, \tag{6.1}$$

where $Y_{lm}(\theta,\phi)$ are the spherical harmonics and a_{lm} are complex expansion coefficients which have to be determined from the photospheric magnetic field. At some distance above the photosphere, the magnetic field is stretched radially away from the solar surface. The region where the heliospheric magnetic field becomes radially oriented is called the *source surface* (Schatten et al. 1969). The source surface is considered to be the origin of the interplanetary magnetic field (IMF). In this approximation all field lines which penetrate through the source surface, i.e. are not closed in the region $R_\odot < r < R_{\rm ss}$ ($R_{\rm ss}$ is the source surface radius), contribute to the open flux.

Requiring that $B_\theta(R_{\rm ss},\theta,\phi)$ and $B_\phi(R_{\rm ss},\theta,\phi)$ vanish at the source surface, the potential Eq. (6.1) has to be replaced by (Altschuler and Newkirk 1969, Nash et al. 1988)

$$\psi(r,\theta,\phi) = R_\odot \sum_{l=0}^{\infty} \sum_{m=-l}^{l} \left(\frac{R_\odot}{r}\right)^{l+1} \left[\frac{(r/R_{\rm ss})^{2l+1}-1}{l+1+l\,(R_\odot/R_{\rm ss})^{2l+1}}\right] a_{lm}\, Y_{lm}(\theta,\phi)\,. \tag{6.2}$$

From the solution Eq. (6.2) it follows that the radial magnetic field component outside the source surface ($r \geq R_{\rm ss}$) is

$$B_r(r,\theta,\phi) = \frac{\partial\psi}{\partial r} = \sum_{l=0}^{\infty} \sum_{m=-l}^{m=l} c_l(r)\, a_{lm}\, Y_{lm}(\theta,\phi)\,, \tag{6.3}$$

where

$$c_l(r) = \left(\frac{R_\odot}{r}\right)^{l+2} \left[\frac{l+1+l(r/R_{\rm ss})^{2l+1}}{l+1+l(R_\odot/R_{\rm ss})^{2l+1}}\right]\,. \tag{6.4}$$

The total open flux is calculated by integrating the unsigned field over the whole source surface

$$\Phi_{\rm open} = R_{\rm ss}^2 \int |B_r(R_{\rm ss},\theta,\phi)|\, d\Omega\,. \tag{6.5}$$

In order to compare the results from the source surface model with the measured radial IMF component near earth, we express the open flux as a field strength at $r_E = 1$ AU

$$B^E_{\rm open} = \frac{\Phi_{\rm open}}{4\pi\, r_E^2}\,. \tag{6.6}$$

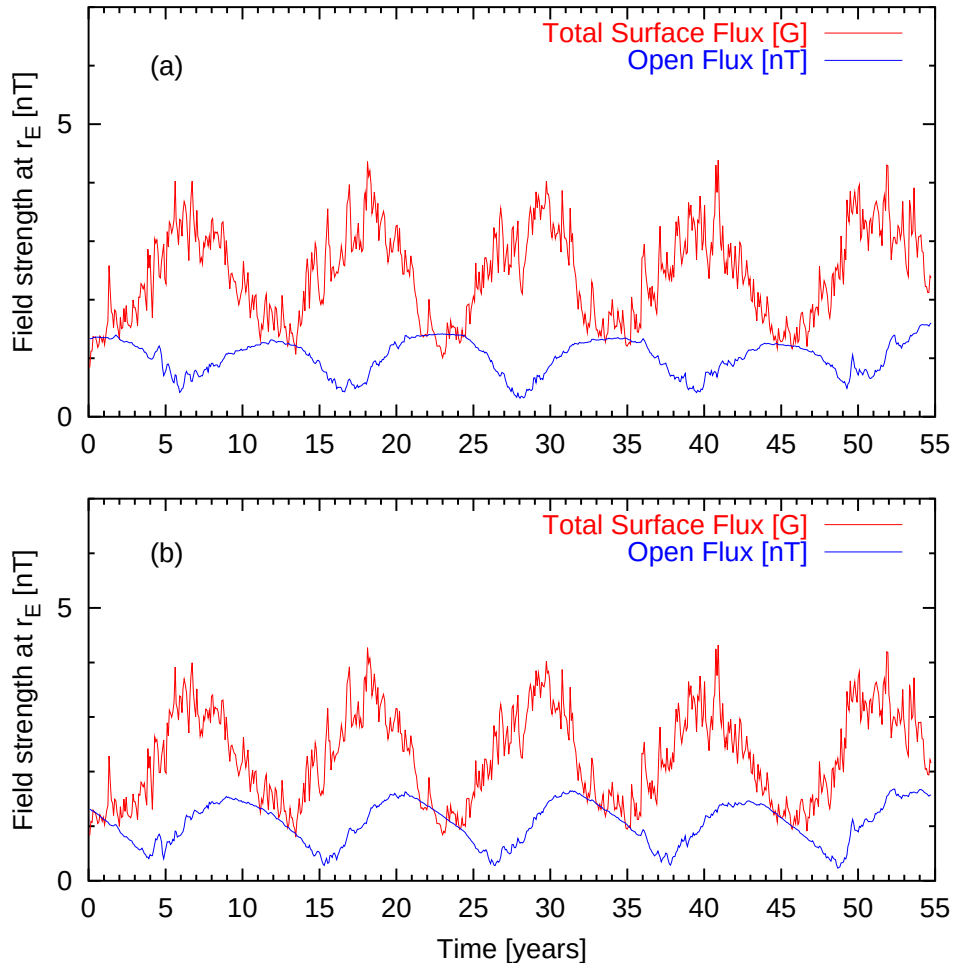

Figure 6.1: Time variation of total surface flux and open flux for a constant source surface location ($R_{\rm ss} = 2.5 R_\odot$) for (a) $\eta = 0$ and (b) $\eta = 100\,{\rm km}^2\ {\rm s}^{-1}$.

Furthermore, the total and the equatorial dipole components at the source surface are defined as

$$D_{\rm tot}(R_{\rm ss}) = \frac{1}{4\pi} \sum_{m=-1}^{1} \int \left| c_1(R_{\rm ss})\ a_{1m}\ Y_{1m} \right| d\Omega\,, \tag{6.7}$$

and

$$D_{\rm eq}(R_{\rm ss}) = \frac{1}{4\pi} \int c_1(R_{\rm ss}) \left[\left| a_{1,-1}\ Y_{1,-1} \right| + \left| a_{1,1}\ Y_{1,1} \right| \right] d\Omega\,, \tag{6.8}$$

respectively. The total quadrupole component at the source surface is given by

$$H(R_{\rm ss}) = \frac{1}{4\pi} \sum_{m=-2}^{2} \int \left| c_2(R_{\rm ss})\ a_{2m}\ Y_{2m} \right| d\Omega\,. \tag{6.9}$$

The described model for calculating the heliospheric magnetic field is referred to as the potential field source surface (PFSS) model in literature.

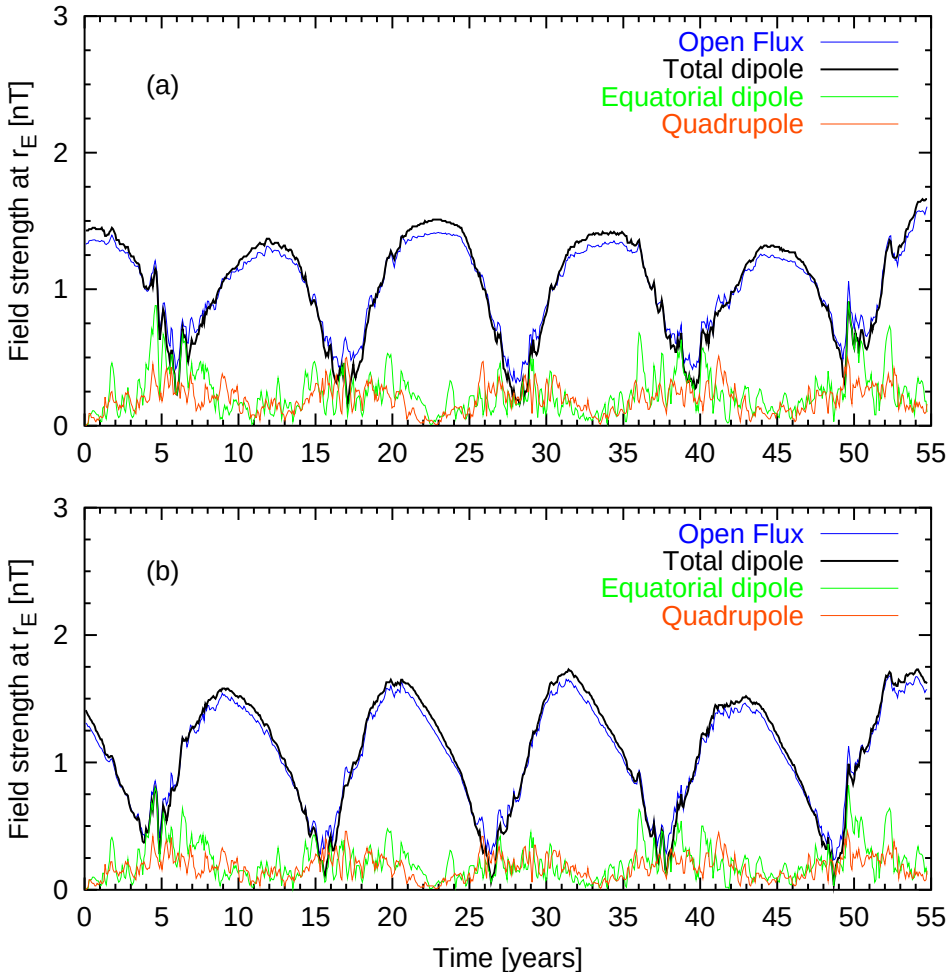

Figure 6.2: Time variation of open flux, total dipole, equatorial dipole and quadrupole for (a) $\eta = 0$ and (b) $\eta = 100\,\mathrm{km}^2\ \mathrm{s}^{-1}$.

6.3 Results for synthetic data

In order to understand qualitatively how the open flux (Eq. 6.5) depends on the surface magnetic field and thus on the flux transport parameters, we use the synthetic butterfly diagram resulting from the reference parameter set (Sect. 4.3.1) and calculate the related open flux. In this section, we investigate two modifications of the model. On the one hand, we perform calculations with and without the decay term derived in Sect. 5.3, and on the other hand we make the source surface radius, R_{ss}, in Eq. (6.4) time-dependent.

6.3.1 Influence of η on the open flux

Fig. 6.1 shows the calculated total surface field and the open flux for the case without the additional decay term (Sect. 5.3) in comparison with the case $\eta = 100\,\mathrm{km}^2\ \mathrm{s}^{-1}$. A part of the polar flux is removed due to radial diffusion in the latter case and thus less new magnetic flux is needed to cancel the existing polar fields. This leads to a shift of

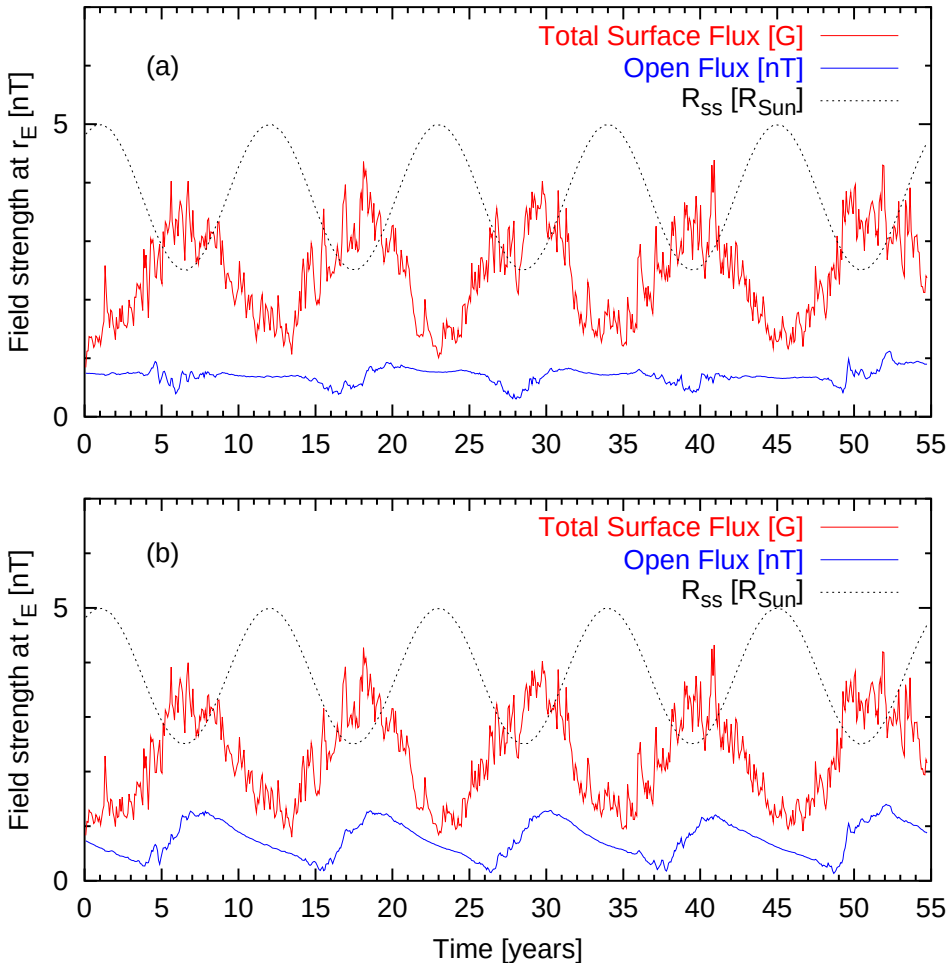

Figure 6.3: Time variation of total surface flux and open flux when the source surface is varying between $R_{\mathrm{ss,max}} = 2.5R_{\odot}$ and $R_{\mathrm{ss,min}} = 5.0R_{\odot}$ for (a) $\eta = 0$ and (b) $\eta = 100\,\mathrm{km}^2\ \mathrm{s}^{-1}$. The sinusoidal variation of the source surface radius is also shown.

the oscillation of the polar field and thus the dipole component towards cycle maximum (Fig. 6.1 b). However, this shift is not sufficient to bring the open flux in the correct phase with the activity cycle as observed. The ratio of maximum to minimum open flux becomes larger when η is set to $100\,\mathrm{km}^2\ \mathrm{s}^{-1}$ than for $\eta = 0$. The open flux variation is rather smooth compared to the surface magnetic field, which undergoes a strong modulation due to fluctuations in the flux emergence. The open flux is almost not affected by these fluctuations. Only during minima of the open flux, can fluctuations be seen. This smoothness is a result of the damping coefficients $c_l(r)$ in the model. The higher multipoles, which represent smaller magnetic flux elements, are strongly damped and thus small flux contributions of the surface field are filtered out in the open flux calculation.

When comparing Figs. 6.2 a and 6.2 b it can be seen that only the total dipole component is shifted by $\eta \neq 0$ while the equatorial dipole and the quadrupole component are almost unaffected by η. Fig. 6.2 shows also that the total open flux is very closely related to the total dipole component.

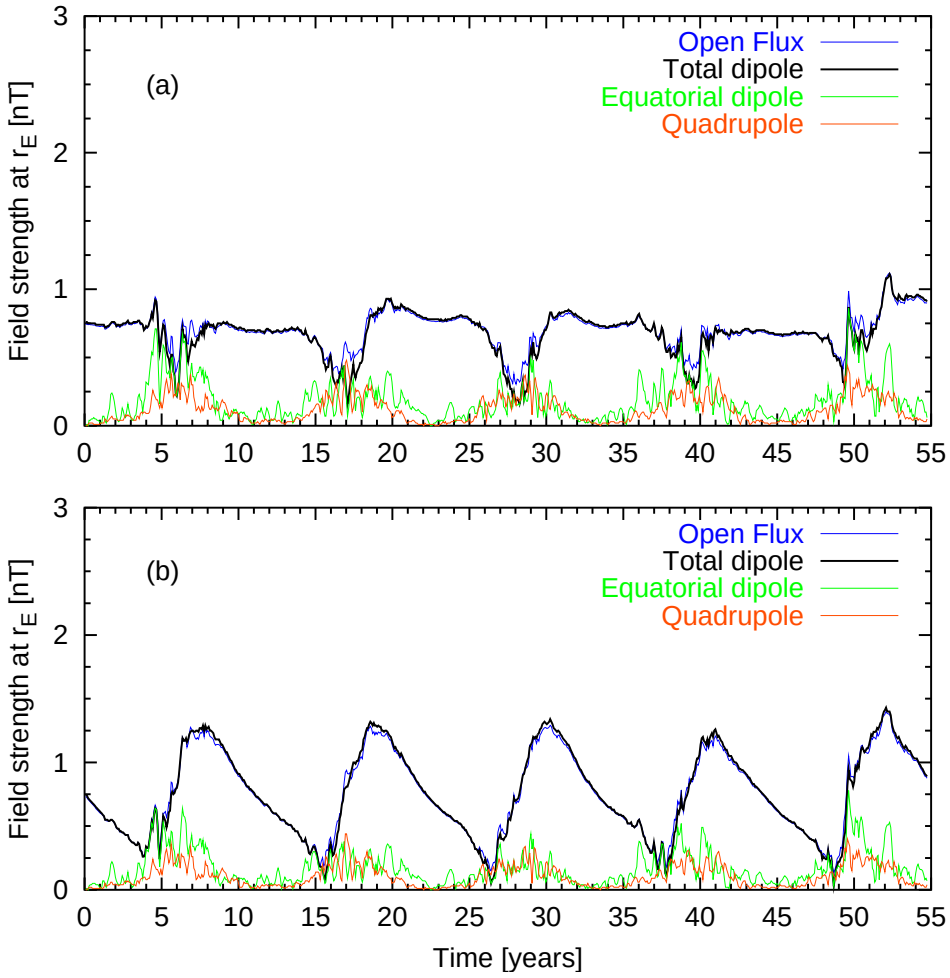

Figure 6.4: Time variation of open flux, total dipole, equatorial dipole and quadrupole when the source surface is varying between $R_{\mathrm{ss,max}} = 2.5 R_\odot$ and $R_{\mathrm{ss,min}} = 5.0 R_\odot$ for (a) $\eta = 0$ and (b) $\eta = 100\,\mathrm{km}^2\,\mathrm{s}^{-1}$.

6.3.2 Time-dependent source surface

The results for the open flux calculated from the source surface model show that a significant fraction of the open flux is missing, especially during sunspot maximum and the rise of a new cycle. Not included in the source surface model are for example coronal mass ejections (CMEs), which carry away magnetic field from the Sun into interplanetary space and occur more frequent during activity maximum than during minimum. In order to include these contributions, we let the source surface radius, R_{ss}, vary with time. During activity maximum, the source surface is assumed to be closer to the photosphere than during activity minimum. We let $R_{\mathrm{ss}}(t)$ vary with a sine function in antiphase with activity. We leave the source surface radius during activity maximum, $R_{\mathrm{ss,max}}$, at a value $2.5\,R_\odot$, whereas the source surface radius during activity minimum, $R_{\mathrm{ss,min}}$, is set to $5\,R_\odot$. The resulting open flux for the varying source surface and the reference parameter set is shown in Fig. 6.3. Without including radial decay in our model, i.e. $\eta = 0$, the open flux remains roughly constant during a longer period around activity minimum and

only varies by a noteworthy amount during activity maximum (Fig. 6.3 a). The increase of the dipole component and thus the open flux during activity minimum as obtained by the simulations with a constant source surface radius is now counter-balanced by the receding source surface. As a result of the larger distance of the source surface during cycle minimum, less magnetic flux penetrates through the source surface and contributes to the open flux. The source surface variation has only a minor effect on the equatorial dipole and the quadrupole components which have significant values only during activity maxima (Fig. 6.4).

The combination of a varying source surface and a radial diffusion coefficient of $\eta = 100\,\mathrm{km}^2\ \mathrm{s}^{-1}$ in the transport model (Fig. 6.3 b) cancels the effect of damping the open flux during cycle minimum as yielded from the source surface variation alone. The reason for this is that the radial diffusion coefficient η alone leads to a shift of the dipole component towards activity maximum. As a consequence of this shift, the dipole component is no longer in anti-phase with $R_{\mathrm{ss}}(t)$. However, the maximum of the open flux is now almost in phase with the level of activity.

6.3.3 High- and low-latitude open flux

In order to investigate separately the contributions to the open flux resulting from polar coronal holes and equatorial coronal holes, we plot the open flux resulting from high latitudes (above $45°$) and low latitudes (below $45°$) in Fig. 6.5 for the four previously discussed cases. In none of the cases is the expected anti-correlation between high- and low-latitude open flux present. In the unmodified model, i.e. $\eta = 0$ and constant R_{ss} (Fig. 6.5 a), the open flux from the equatorial region reaches its maximum roughly $1 - 2$ years after the open flux from the polar regions. However, the amplitude variation between maximum and minimum is less for the low-latitude open flux than for the high-latitude open flux.

In the case when $\eta = 100\,\mathrm{km}^2\ \mathrm{s}^{-1}$ the high and low-latitude fractions of the open flux are brought more into phase (Fig. 6.5 b). The situation is different when applying a time variation of the source surface radius (Fig. 6.5 c). The flattening of the dipole component as discussed in Sect. 6.3.2 is also reflected in the high- and low-latitude component of the open flux. During activity maximum, due to the combined effect of strong equatorial coronal holes and the closeness of the source surface, the low-latitude open flux shows strong variation and becomes sometimes higher than during activity minimum, while the high-latitude open flux drops towards zero. The combination of a variable source surface and $\eta = 100\,\mathrm{km}^2\ \mathrm{s}^{-1}$ brings both, high- and low-latitude component, in close relation (Fig. 6.5 d). Both curves contribute almost the same amount to the total open flux, they are almost in phase and also their amplitudes are of comparable strength.

6.3.4 Variation of R_{ss}

Unlike before, where we let the source surface radius vary with time, we now vary the constant distance of the source surface from the photosphere. A value of $R_{\mathrm{ss}} = 2.5 R_{\odot}$ for the source surface radius is widely accepted in literature (Altschuler and Newkirk 1969, Mackay et al. 2002a, Wang and Sheeley 2002). For this choice of the source surface radius, the field line structure of the calculated coronal magnetic field is in good agreement

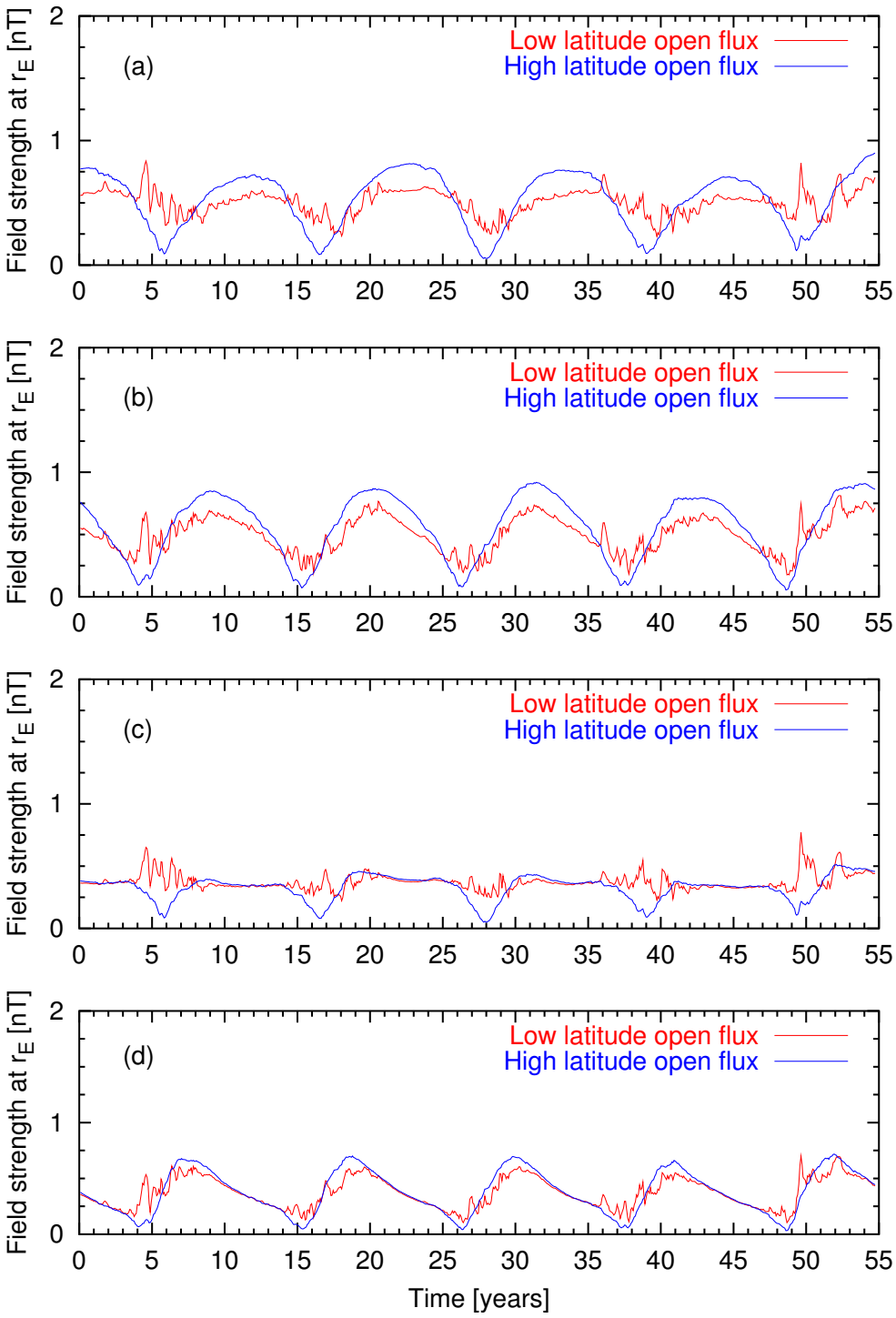

Figure 6.5: High-latitude (above $45°$) and low-latitude (below $45°$) contributions to the open flux. (a) $\eta = 0$ and constant $R_{\mathrm{ss,min}} = 2.5R_{\odot}$, (b) $\eta = 100\,\mathrm{km}^2\ \mathrm{s}^{-1}$ and constant $R_{\mathrm{ss,min}} = 2.5R_{\odot}$, (c) $\eta = 0$ and variable source surface $R_{\mathrm{ss,max}} = 5.0$ and $R_{\mathrm{ss,min}} = 2.5R_{\odot}$ and (d) $\eta = 100\,\mathrm{km}^2\ \mathrm{s}^{-1}$ and variable source surface $R_{\mathrm{ss,max}} = 5.0R_{\odot}$ and $R_{\mathrm{ss,min}} = 2.5R_{\odot}$

with observations of the corona during eclipses. However, Schatten et al. (1969) found that a source surface radius of $R_{\mathrm{ss}} = 1.6R_{\odot}$ leads to a good agreement of the calculated open flux with the observed IMF. The validity of the source surface model becomes questionable when the source surface is placed too close above the photosphere because actually closed field lines then penetrate through the source surface and are misleadingly counted to the open flux.

The resulting open flux from the synthetic reference parameter set for four different source surface radii is shown in Fig. 6.6. For $R_{\mathrm{ss}} = 1.75R_{\odot}$ and $R_{\mathrm{ss}} = 2.0R_{\odot}$, respectively, there is no big change in the behaviour of the open flux compared to the case $R_{\mathrm{ss}} = 2.5R_{\odot}$ (Fig. 6.1 b). Only the amplitude increases slightly due to more magnetic flux reaching the source surface as R_{ss} decreases. By reducing R_{ss} from $1.75R_{\odot}$ to $1.5R_{\odot}$, the amount of open flux increases by almost 30% and the maximum open flux is reached around 1 year earlier. This temporal shift results from the low-latitude flux that is now increased and out of phase with the high-latitude flux. The open flux from low latitudes shows more fluctuations than the open flux from the polar regions. This is due to the fact that in the low latitudes individual large active regions contribute to the open flux which cause these fluctuations, whereas the more uniform polar fields lead to a smooth high-latitude open flux. When the source surface radius is decreased even more ($R_{\mathrm{ss}} = 1.25R_{\odot}$), the amplitude of the low-latitude open flux exceeds the high-latitude open flux. However, having such a small source surface radius the physical aspects of the source surface model become questionable.

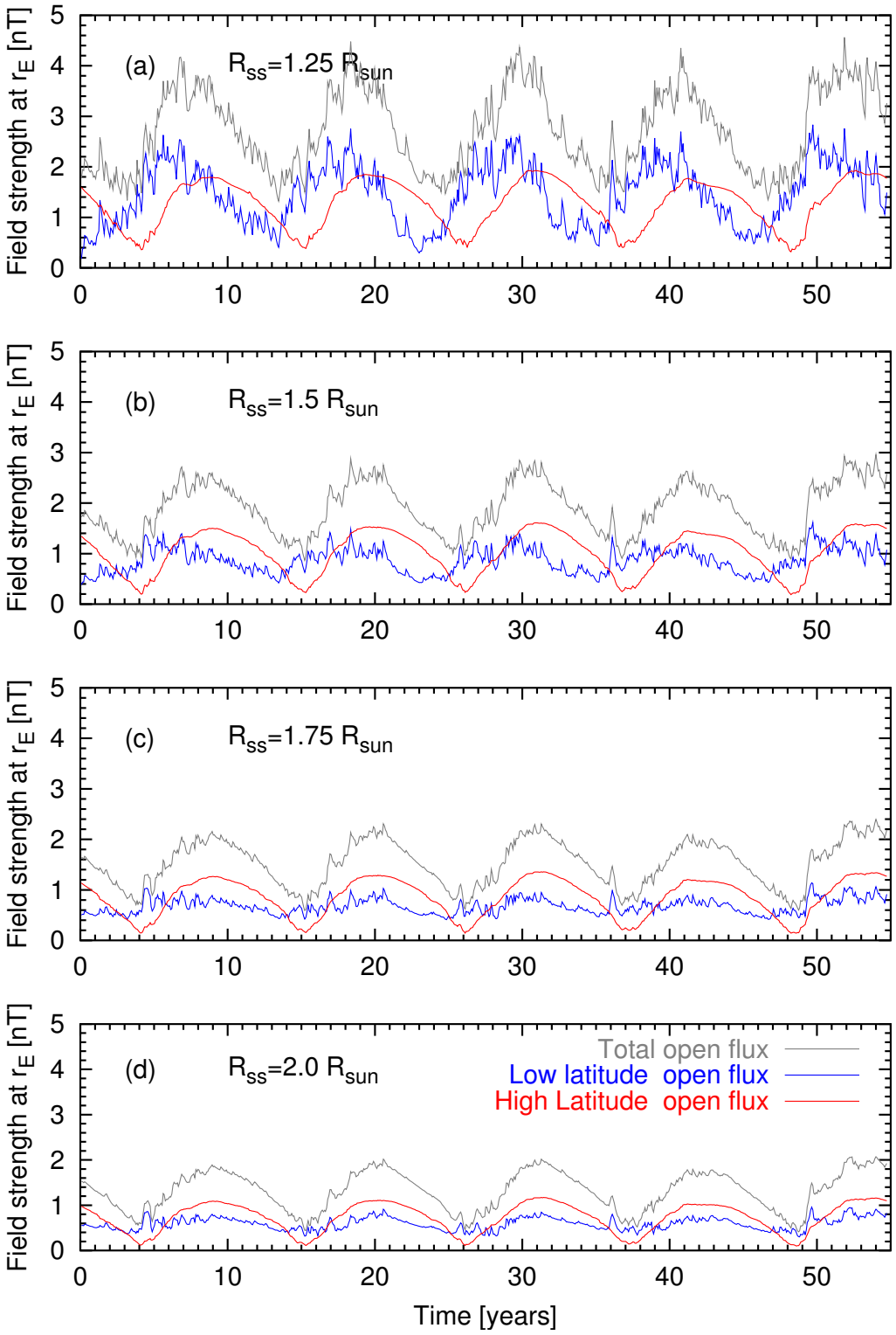

Figure 6.6: Total, high- and low-latitude open flux for four different source surface radii. (a) $R_{ss} = 1.25R_{\odot}$, (b) $R_{ss} = 1.5R_{\odot}$, (c) $R_{ss} = 1.75R_{\odot}$ and (d) $R_{ss} = 2.0R_{\odot}$.

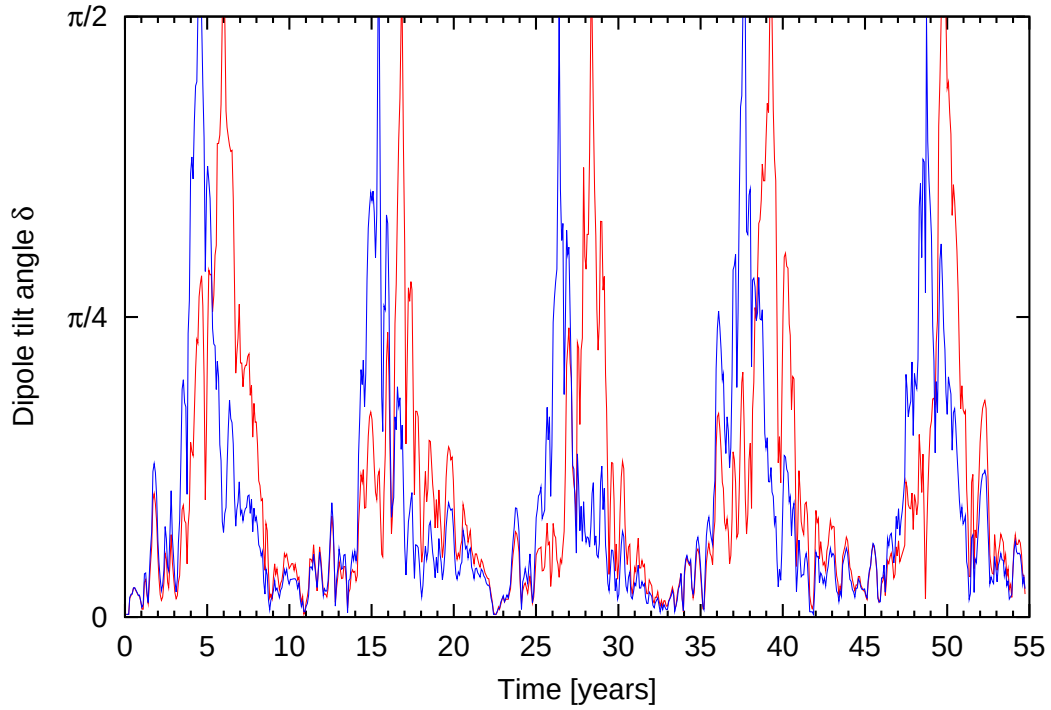

Figure 6.7: Dipole tilt angle for the reference parameter set for $\eta = 0$ (*red line*) and $\eta = 100\,\mathrm{km^2\ s^{-1}}$ (*blue line*).

6.4 Dipole tilt angle

The cyclic polar field reversal can be interpreted as a rotation of the dipole axis. During activity minima, the heliospheric current sheet is located in the equatorial plane. With increasing activity the current sheet becomes distorted and more inclined with respect to the equatorial plane (Balogh and Smith 2001). Fisk and Schwadron (2001) presented a model of a rotating heliospheric current sheet (which lies perpendicular to the dipole axis) as the origin of the polar field reversal.

The dipole tilt angle with respect to the axis of rotation is

$$\delta = \arcsin\left(\frac{D_{\mathrm{eq}}}{D_{\mathrm{tot}}}\right) . \tag{6.10}$$

The time behaviour of the dipole tilt angle for the reference parameter set for $\eta = 0$ and $\eta = 100\,\mathrm{km^2\ s^{-1}}$ is shown in Fig. 6.7. During activity minima, the dipole axis is roughly parallel to the axis of rotation, i.e. the dipole tilt angle is close to 0. This configuration is maintained roughly during half a cycle. Around cycle maximum, the dipole tilt angle increases rapidly and leads to a reversal of the dipole. The time of the reversal takes also about half a cycle. From Fig. 6.7 the advanced dipole reversal by about 2 years when $\eta = 100\,\mathrm{km^2\ s^{-1}}$ can be clearly seen.

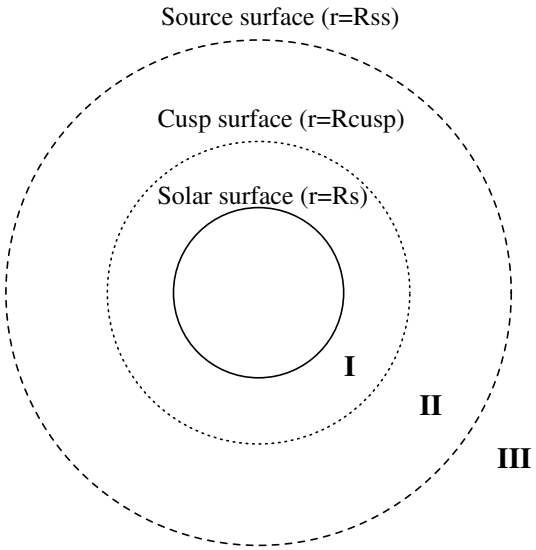

Figure 6.8: Geometry of the current sheet source surface model.

6.5 The current-sheet source surface model

The PFSS model is a crude way to derive the interplanetary magnetic field from the photospheric field. A major deficit is that it underestimates the open flux originating from the activity belts. The forcing of the magnetic field into radial direction at the source surface leads to a wrong topology of the coronal field, especially in the equatorial region. For example, helmet streamers or polar plumes tend to bend towards the equator. In order to improve the source surface model, which includes only volume currents, Schatten (1972) suggested the potential field-current sheet (PFCS) model, which includes the effect of current sheets.

In a first step, a potential field solution is derived for the region between the photosphere and a source surface. Then the magnetic field is calculated on the source surface. If the radial magnetic field component on the source surface points inwards, i.e. $B_r(R_{\rm ss}, \theta, \phi) < 0$, then $\mathbf{B}(R_{\rm ss}, \theta, \phi)$ is replaced by $-\mathbf{B}(R_{\rm ss}, \theta, \phi)$. After having done so, the magnetic field points outward everywhere on the source surface. However, the magnitude of the field remains unchanged. At this point, this procedure violates $\nabla \cdot \mathbf{B}$, but this error is corrected in a later step. The magnetic stresses beyond the source surface are not affected by this procedure, so that the field lines still form a minimum energy configuration. The physical aspect of this treatment is, that the field lines now cannot form closed loops beyond the source surface. In the second step, the original orientation of the field lines is restored. As a result, appropriate current sheets must form in order not to violate $\nabla \times \mathbf{B} = (4\pi/c)\,\mathbf{j}$.

Zhao and Hoeksema (1994) presented a model based on a magnetostatic atmosphere instead of a potential field. In principle, this model (called horizontal current-current sheet (HCCS) model) builds on the current-sheet technique of Schatten (1972). It also includes horizontal electric currents in addition to the streamer currents. The concept of the HCCS model is to introduce a *cusp surface* at a distance $R_{\rm cusp}$ above the solar surface. $R_{\rm cusp}$ is assumed to be the location of the cusp points of coronal helmet streamers.

Thus the magnetic field at the cusp surface is determined in a similar way as Schatten (1972) calculated the source surface field in the PFCS model. A further development of modelling the coronal field structure is the current sheet-source surface (CSSS) model (Zhao and Hoeksema 1995). This is a composite model that uses the streamer current sheet technique at a cusp surface (like in the HCCS model) and combines it with the PFSS model that forces the field lines in radial direction at an outer source surface. To this aim, the heliosphere is separated into 3 regions (Fig. 6.8). In a magnetostatic atmosphere with only horizontal electric currents, the analytical solution for the magnetic field is (Bogdan and Low 1986)

$$\mathbf{B} = -\left(1+\frac{a}{r}\right)^2 \frac{\partial \Phi}{\partial r}\,\hat{r} - \frac{1}{r}\frac{\partial \Phi}{\partial \theta}\,\hat{\theta} - \frac{1}{r\sin\theta}\frac{\partial \Phi}{\partial \phi}\,\hat{\phi}\,, \tag{6.11}$$

where the parameter a represents the length scale of horizontal electric currents in the corona.

The inner region (region I) is bordered by the photosphere and the cusp surface. The potential in this inner region is

$$\Phi_{\rm in} = \sum_{l=1}^{N_\odot}\sum_{m=0}^{l} R_l^\odot(r)\; P_l^m(\cos\theta)\; (g_{lm}^\odot\;\cos m\phi + h_{lm}^\odot\;\sin m\phi)\,, \tag{6.12}$$

where $N_\odot$ is the maximum principal index and $g_{lm}^\odot$ and $h_{lm}^\odot$ are the harmonic expansion coefficients which have to be determined from the photospheric field. The radial part of Eq. (6.12) is given by

$$R_l^\odot(r) = \frac{R_\odot(1+a)^l}{(l+1)(r+a)^{l+1}}\,. \tag{6.13}$$

In the middle region (region II), between the cusp surface and the source surface, the solution for the potential is

$$\Phi_{\rm mid} = \sum_{l=0}^{N_\odot}\sum_{m=0}^{l} R_l^c(r)\; P_l^m(\cos\theta)\; (g_{lm}^c\;\cos m\phi + h_{lm}^c\;\sin m\phi)\,, \tag{6.14}$$

with the radial part

$$\begin{aligned} R_l^c(r) \;&=\; R_\odot\left[\frac{l+1}{R_{\rm cusp}^2(R_{\rm cusp}+a)^l} + \frac{l(R_{\rm cusp}+a)^{l+1}}{R_{\rm cusp}^2(R_{\rm ss}+a)^{2l+1}}\right]^{-1} \\ &\quad\times\left[\frac{1}{(r+a)^{l+1}} - \frac{(r+a)^l}{(R_{\rm ss}+a)^{2l+1}}\right]\,. \end{aligned} \tag{6.15}$$

The coefficients g_{lm}^c and h_{lm}^c have to be determined by a least squares matching procedure. For a detailed mathematical treatment see Schatten (1972) and Zhao and Hoeksema (1995).

In the outer region (region III), beyond the source surface, the field is supposed to be radial and the radial component is extrapolated into interplanetary space by

$$B_r(r \geq R_{\rm ss},\theta,\phi) = B_r(R_{\rm ss},\theta_{\rm ss},\phi_{\rm ss})\;\left(\frac{R_{\rm ss}}{r}\right)^2\,. \tag{6.16}$$

Comparison of the CSSS model and the PFSS model

We investigate to what extent the more complex CSSS model leads to results for the open flux which are in better agreement with the observations. Therefore, we calculate the open flux from both models for our reference parameter set (Sect. 4.3) with $\eta = 100\,\mathrm{km}^2\ \mathrm{s}^{-1}$. Zhao and Hoeksema (1995) found that the parameter set $a = 0.2$, $R_{\mathrm{cusp}} = 1.4R_{\odot}$ and $R_{\mathrm{ss}} = 3.25R_{\odot}$ matches the observed radial IMF component quite well when extrapolating WSO photospheric field observations. Here, we use the parameters $a = 0.2$, $R_{\mathrm{cusp}} = 1.6R_{\odot}$ and set the source surface in both models (CSSS and PFSS) to $R_{\mathrm{ss}} = 2.5R_{\odot}$.

In order to understand qualitatively the differences between the two models, we investigate the latitudinal variation of the magnetic flux on the source surface. To this aim, we choose 4 different cycle minima and cycle maxima where we calculate the source surface flux.

During solar minimum, the open flux determined with the PFSS model at high latitudes varies approximately as the sine of latitude (Fig. 6.9 a). This behaviour comes from the fact that the open flux calculated with the PFSS model follows closely the dipole configuration of the photospheric field, which is especially pronounced during activity minimum. The CSSS model differs from the PFSS model in the equatorial region. Flux loops in the low latitudes that extend beyond the cusp surface are opened by the CSSS model and thus contribute to the open flux. This opening of flux by introducing a current sheet leads to a jump of the open flux at the equator from one polarity to the opposite polarity. This behaviour at the equator (*'split monopole'*) is qualitatively in better agreement with observations (e.g. by the Ulysses spacecraft) than the continuous latitudinal variation of open flux obtained by the PFSS model.

During solar maximum, the PFSS open flux resembles the quadrupolar structure of the photospheric field (Fig. 6.9 b). The open flux from the CSSS model shows a completely different behaviour. It remains almost constant over the whole range of latitudes with a switching of polarities at the equator.

The time evolution of the integrated open flux obtained by both models is shown in Fig. 6.10. At high latitudes (Fig. 6.10 b), the results from the two models show no big difference which becomes clear already from inspecting the latitudinal variation of the open fluxes (Fig. 6.9). The low latitude open flux from the CSSS model is higher than the one from the PFSS model (Fig. 6.10 c). This is due to the abrupt polarity reversal at the equator in the CSSS model which leads to a higher value of the open flux (which is the integral over the unsigned field at R_{ss}, Eq. 6.5). Also, there is a phase lag of about 1 year. The open flux from the CSSS model is ahead of the PFSS open flux. This might be a result of the cusp surface (beyond which all flux is already open) in the CSSS model being closer to the solar surface than the source surface in the PFSS model. This time lag has already been discussed in Sect. 6.3.4 where we found that a smaller source surface radius leads to a shift of the total open flux.

In summary, we can say that the CSSS model leads to more realistic results than the PFSS model when considering the heliospheric structure, especially for the low-latitude open flux by including the effect of horizontal currents and volume currents.

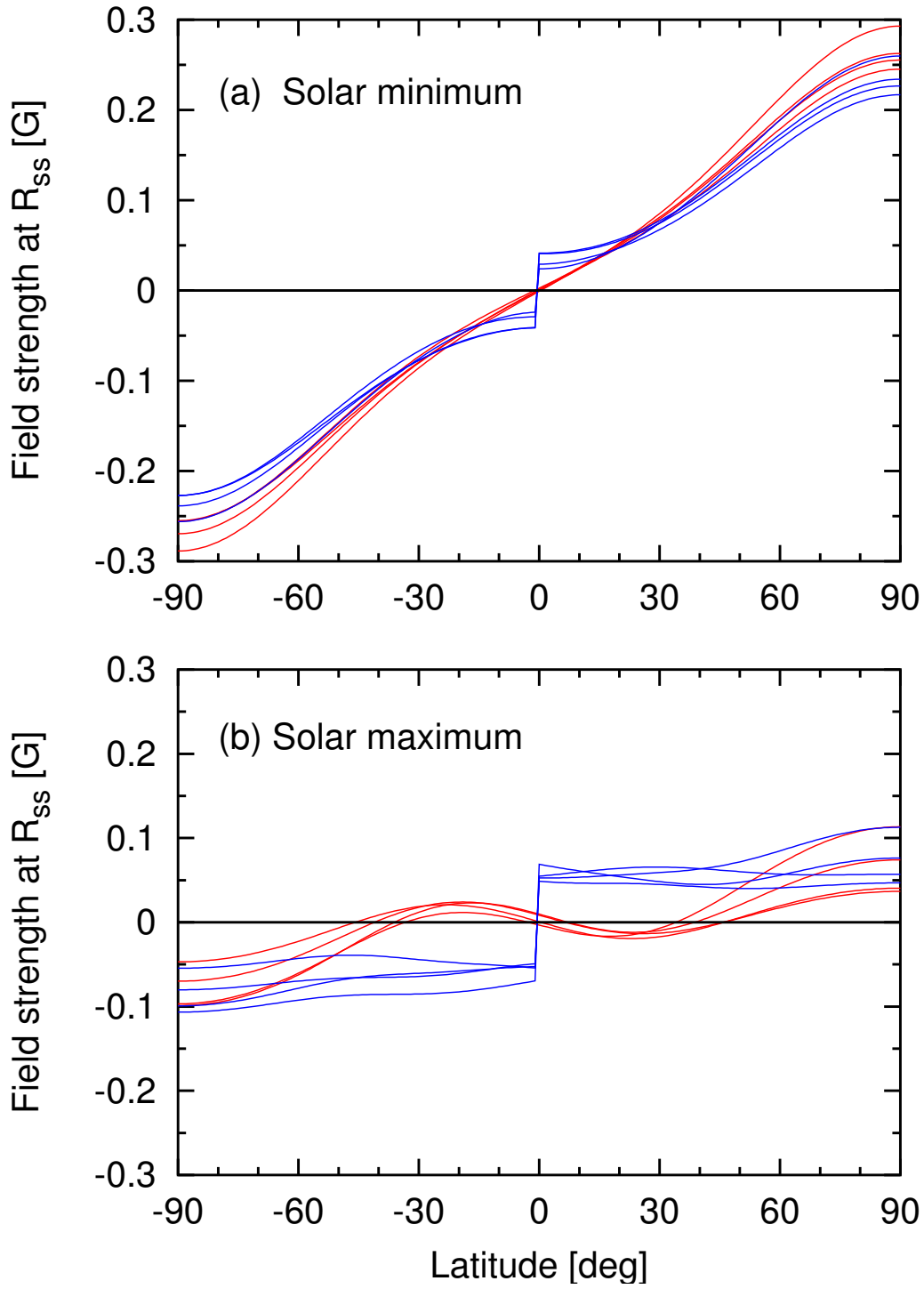

Figure 6.9: Latitudinal variation of the longitude averaged magnetic field on the source surface obtained with the PFSS model (*red lines*) and the CSSS model (*blue lines*) for 4 different times during solar minimum (a) and solar maximum (b). In the plot, the polarities are changed such that the field on the northern hemisphere is always positive.

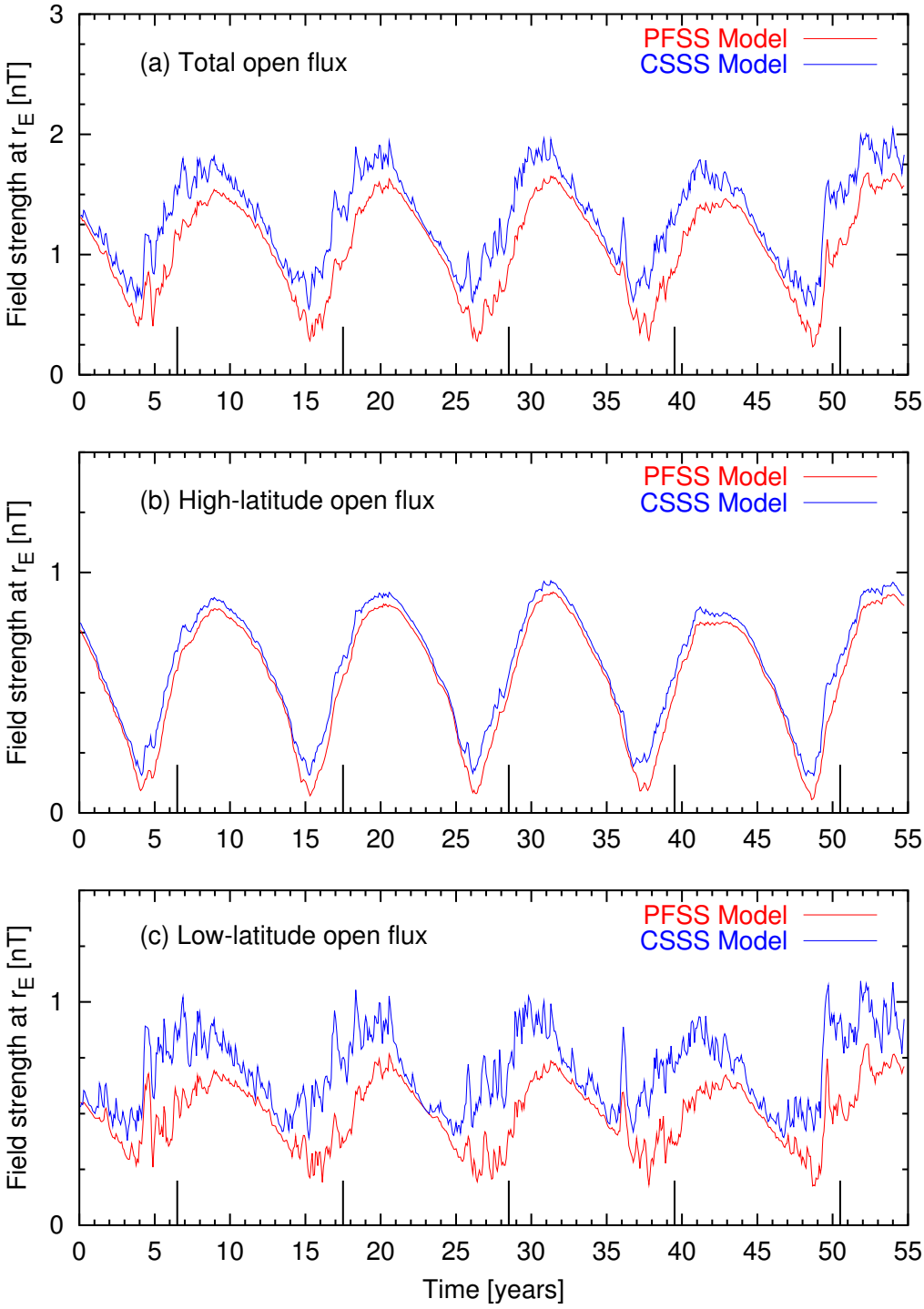

Figure 6.10: Comparison of the simulated open flux from the PFSS model and the CSSS model ($R_{\rm ss} = 2.5R_\odot$ and $R_{\rm cusp} = 1.6R_\odot$). (a) Total open flux, (b) high-latitude open flux ($> 45°$) and (c) low-latitude open flux ($< 45°$) obtained from the synthetic reference butterfly diagram ($\eta = 100\,{\rm km}^2\ {\rm s}^{-1}$). The vertical black lines indicate the times of activity maxima.

6.6 Simulation of the open flux on the basis of the RGO sunspot data

6.6.1 Method of transforming the sunspot record into an active region sequence

When modelling the magnetic field of the historical Sun, the relative sunspot number can be used as a proxy for flux emergence, because of the observed linear relationship between magnetic flux and the corresponding sunspot area (Schrijver and Harvey 1994). Here, we take the sunspot group areas from the digitized version of the Royal Greenwich Observatory (RGO) photographic results, which are available for the time period 1874-1976. After the Royal Greenwich Observatory concluded the sunspot dataset in 1976, the US Air Force (USAF) started compiling data from the Solar Optical Observing Network (SOON). This continued the RGO dataset with the help of the US National Oceanic and Atmospheric Administration (NOAA). However, care must be taken when using these extended data (from 1976 until present), because they are less uniformly compiled than the previous RGO collection and there may be systematic differences between the sunspot areas in the two records. We combine both datasets and transform them into a sequence of active regions as described below, in order to model the historical IMF record on this basis.

Our basic assumption is that every sunspot group can be related to one active region and thus also to one facular area. The relation of facular to sunspot area has been derived by Chapman et al. (1997) using a 7.5 year data set obtained at the San Fernando Observatory

$$A_{\mathrm{f}} = 414 + 21A_{\mathrm{s}} - 0.0036A_{\mathrm{s}}^2\,, \tag{6.17}$$

where A_{f} is the facular area seen in Ca II K line (393.4 nm) and A_{s} is the sunspot area. In an attempt to simulate the open flux starting from the RGO sunspot group record, we assume the total area of an active region to be $A_{\mathrm{tot}} = A_{\mathrm{s}} + A_{\mathrm{f}}$, where A_{s} is the area of the sunspots from the RGO/SOON data and A_{f} is the facular area derived from Eq. (6.17).

A problem of the RGO sunspot observations is that only spots on the visible solar disk are recorded, while there is no information about activity on the far side of the Sun. The observations thus miss about 50% of the small sunspots. For larger sunspot groups, this fraction is smaller because big spot groups emerging on the back side of the Sun are brought to the visible disk by the Sun's rotation. The estimation of the correct number of missing spot groups in the observation is a difficult task, as one has to take into account visibility problems near the solar limb, different decay stages of the spot groups, and the recurrence of sunspot groups (Kopecký et al. 1985). For our aims we restrict ourselves to a rough estimation of the missing spot groups. We extract all sunspot groups from the RGO database at the time of their maximum area development. This ensures that every spot group is considered only once. Furthermore, we take only sunspot groups which reach their maximum area within $\pm 45^\circ$ of the central meridian. Owing to the large number of observations, we expect this 90° window to be representative for the whole Sun (Note that by doing this, we neglect the possible presence of active longitudes and their flip-flop (Berdyugina and Usoskin 2003)). We construct now our butterfly diagram for the whole Sun by copying this 90° window 4 times to the remaining longitudes. Therefore,

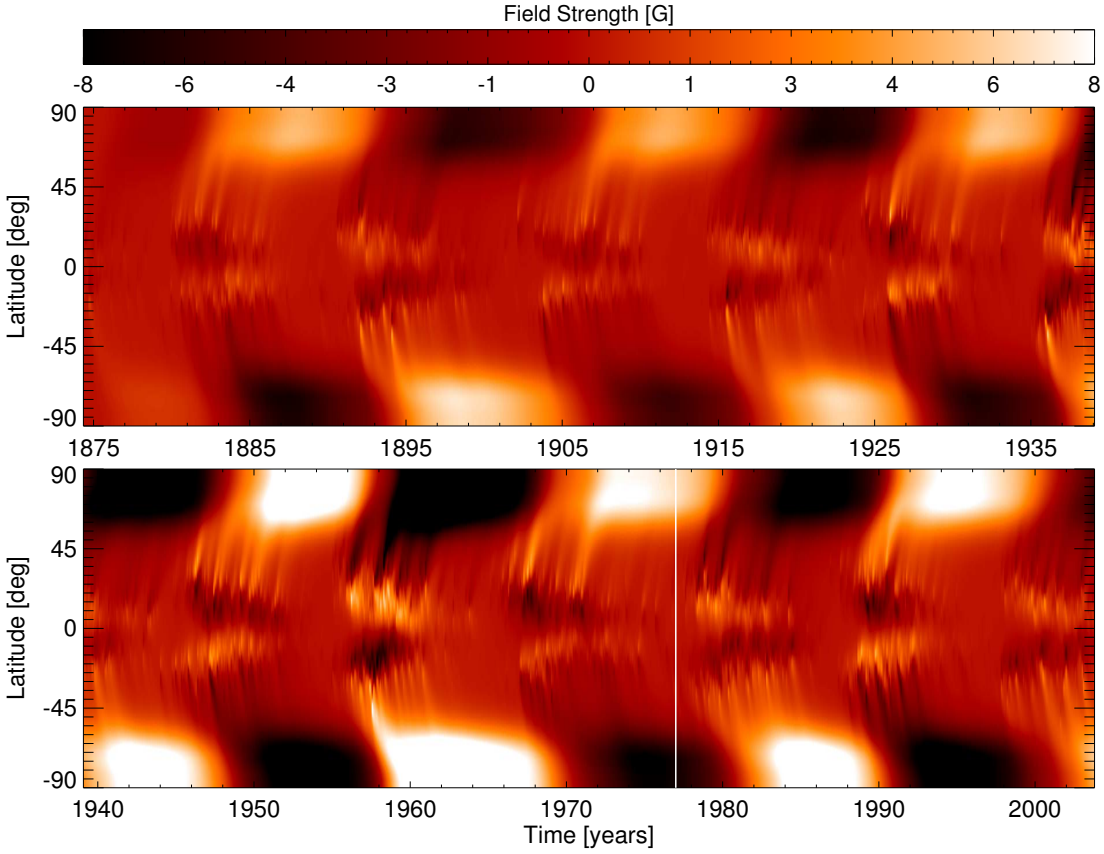

Figure 6.11: Simulated magnetic butterfly diagram. The input sources are derived from the extended RGO sunspot database. The vertical white line indicates the transition of the RGO observation period and the USAF sunspot database.

an observed sunspot group at a longitude ϕ is assumed to emerge at the same time with equal size at longitudes $\phi + 90°$, $\phi + 180°$ and $\phi + 270°$.

Having constructed a butterfly diagram in the above described way, we assign a bipolar magnetic region (BMR) to each sunspot group. The polarities of the BMRs are determined according to Hales' polarity rule (Hale et al. 1919) and the tilt angle is given by Joy's law, i.e. $\alpha = 0.5\,\lambda$, where λ is the latitude. The size of the BMR is determined by Eq. (6.17). For details of the treatment of BMRs in the code see Sect. 3.2. The number of BMRs for each cycle is given in Table 6.1; it is in general $3 - 5$ times higher than in the reference parameter set ($\sim 2\,000$ BMRs per cycle).

Owing to the linearity of the flux transport equation, the amplitude of emerging bipolar magnetic regions, i.e. $B_{\max}$ in Eq. (3.19), is a free parameter that can be adjusted in order to match the simulation with the observations. We calibrate $B_{\max}$ by comparing our result for the total surface field with the field strength given by the Mt. Wilson magnetic plage strength index (MPSI). The maximal polar field strengths for the cycles 21 and 22 are between $7-10$ G according to Dikpati et al. (2004) who analysed the polar fields measured at three different observatories (MWO, WSO and NSO). We find good agreement with our simulations for this time period using a value $B_{\max} = 50$ G.

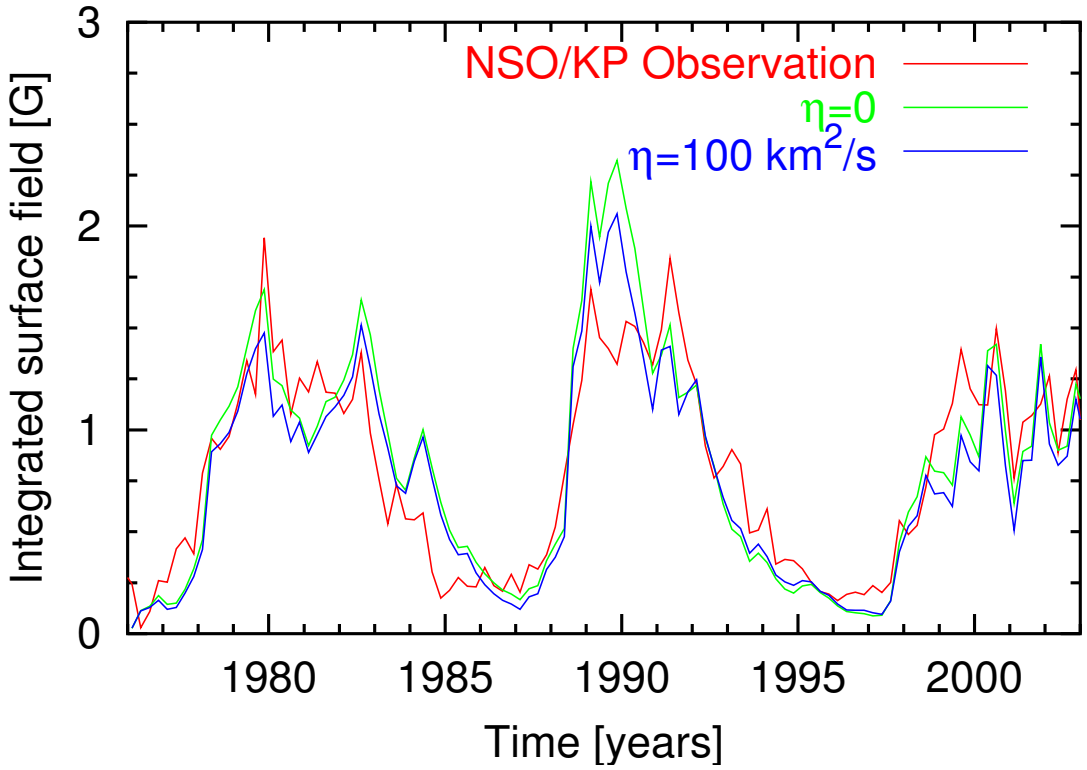

Figure 6.12: Field strengths obtained by integrating the absolute value of the longitude averaged surface field over the latitude range $\pm 45°$ (note that this integral is not equivalent to the total unsigned surface flux). Observation corresponds to the magnetic butterfly diagram Fig. 5.5 a, the simulation ($\eta = 0$) to Fig. 5.5 b and the simulation ($\eta = 100\,\mathrm{km}^2\ \mathrm{s}^{-1}$) to Fig. 5.5 c. Plotted is the 3 month average.

6.6.2 Surface magnetic field

We use the extended flux transport model (with $\eta = 100\,\mathrm{km}^2\ \mathrm{s}^{-1}$) in order to simulate the evolution of the solar surface magnetic field. The simulated longitude-averaged surface magnetic field for the time period 1874-2002 is shown in Fig. 6.11. The obtained magnetic butterfly diagram for the period after 1976 is discussed in connection with the effect of η in the extended flux transport model in Sect. 5.4.3. In order to compare the simulated surface magnetic field with the observation quantitatively, we integrate the longitude averaged surface field over the magnetic butterfly diagrams (i.e. Figs. 5.5 a - c). The integration is done over the latitude range $\pm 45°$, i.e. over the activity belts, in order to exclude the large uncertainties of the observed polar fields. The results are shown in Fig. 6.12. The curves of the simulations agree well with the observation. Especially the phase relation is in good agreement. The curve of the simulation with $\eta = 0$ lies slightly above the curve with $\eta = 100\,\mathrm{km}^2\ \mathrm{s}^{-1}$. However, the differences are not very big, indicating that the parameter η has not a big effect on the field in the activity belts.

The field strengths of the first 5 cycles, i.e. cycles $12 - 16$, are of comparable magnitude as can be seen from the total unsigned surface flux (Fig. 6.13). This is contrary to what one would expect when looking at the sunspot numbers for the same cycles which

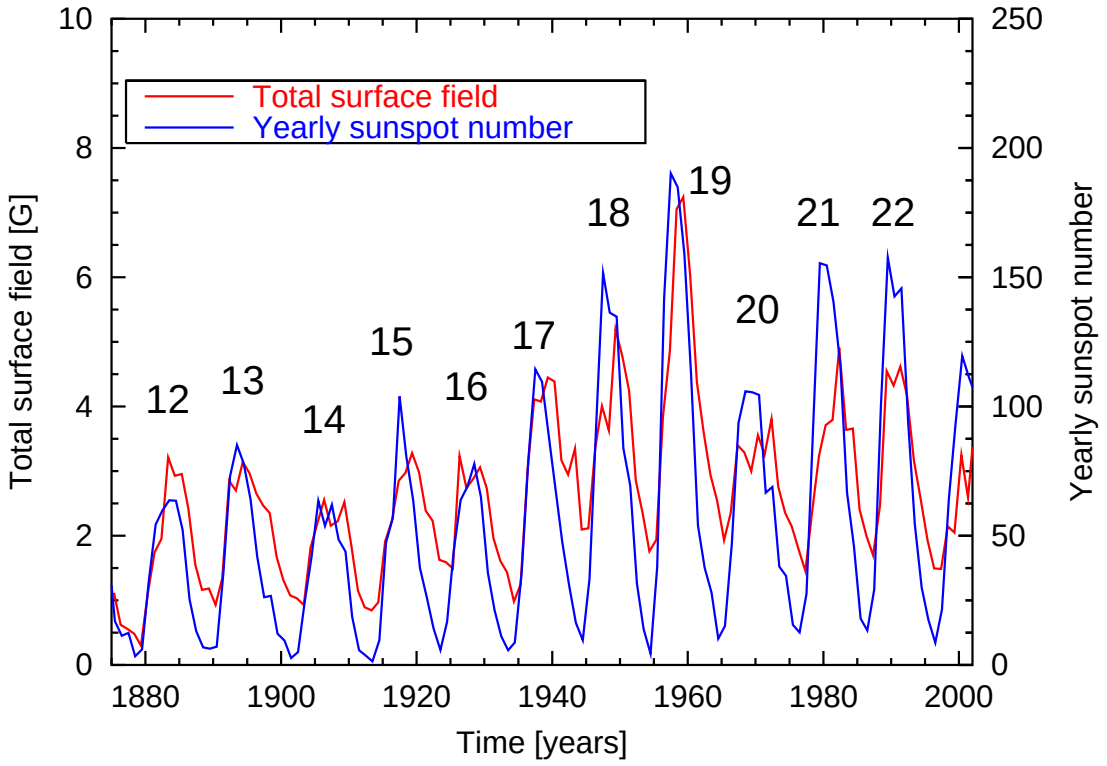

Figure 6.13: Annual means of simulated total surface field and sunspot number. The cycle numbers are also given.

alternate remarkably. This indicates that although a smaller amount of active regions emerges during cycles 12, 14 and 16, the total flux emergence in this cycles is similar to cycles 13 and 15. The similar strength of the cycles 12-15 can also be seen in the the evolution of the polar fields, defined as the average field over caps within 15° of the pole (Fig. 6.14). After a short initialization period of the simulation, the first 5 cycles (cycles 12 to 16) show rather regular oscillation with a maximum amplitude of ~ 6 G. The situation is different for the cycles 17-19. Here, a continuous increase in the sunspot number also leads to an increase in the total surface field and in the polar field. This is interesting because the total amount of emerging BMRs per cycle in our simulation is lower for cycle 18 than for cycle 17. A drop of a factor of about 2 in sunspot number, total surface field and polar field appears from cycle 19 to cycle 20, although the total number of emerging BMRs in both cycles is almost the same.

6.6.3 Comparison with IMF observations

We use the extended flux transport model ($\eta = 100\,\mathrm{km}^2\ \mathrm{s}^{-1}$) in order to simulate the evolution of the surface magnetic field on the basis of the RGO sunspot group data. From the simulated surface field we then calculate the open flux using the CSSS model with $R_{\mathrm{cusp}} = 1.6R_\odot$ and $R_{\mathrm{ss}} = 2.5R_\odot$. Direct IMF measurements are available since 1969. A longer time series for the radial IMF component has been reconstructed by Lockwood

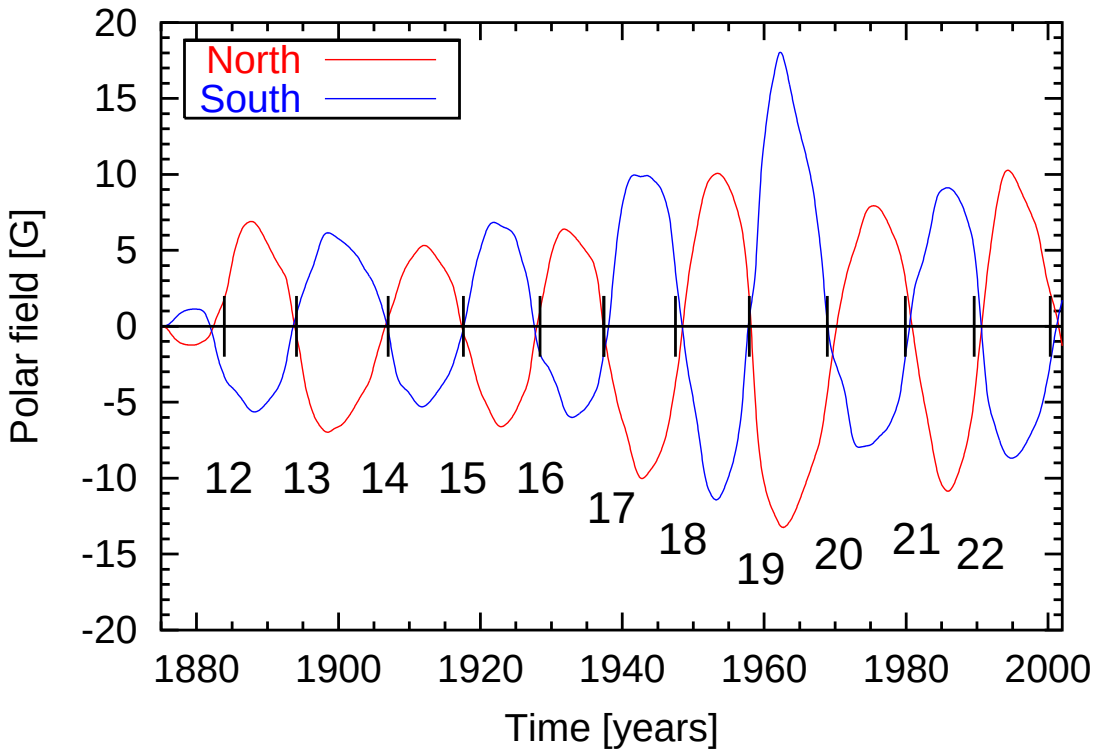

Figure 6.14: Simulated north and south polar field strength. The vertical black lines indicate the times of solar maxima.

et al. (1999) from the geomagnetic *aa* index. The comparison of the calculated open flux with the IMF measurements/reconstruction is shown in Fig. 6.15 a.

The simulation matches the reconstructed IMF rather poorly. The most striking difference is the long-term trend of the minimum open flux. The reconstructed minima of the open flux increase steadily from $\sim$ 0.7nT at 1900 up to $\sim$ 3nT at 1990 whereas the simulated open flux does not show this trend. This indicates that significant sources of the open flux are missing in the model. As we use sunspot group data as a proxy for flux emergence we have not included ephemeral regions (i.e. small active regions without sunspots) in our model. The contribution of ephemeral regions (ERs) to the open flux is rather uncertain while their contribution to the surface magnetic field is significant. ER show a more random orientation, so that their contribution to the Sun's total dipole moment is much smaller than the contribution from the large active regions (Schrijver and Harvey 1994). In contrast to sunspot cycles, ERs of consecutive cycles strongly overlap (Harvey 1992). This might contribute to the secular variation of the open flux (Solanki et al. 2002b). We found in Sect. 4.4.5 that an overlap of successive cycles leads to a build-up of a background magnetic field. In Fig. 6.15 a we have included the fraction of open flux originating from ERs obtained from the model of Solanki et al. (2002b). In this model it is assumed that the ER cycles are longer and shifted forward in time by 2.5 years with respect to the active region cycle. The modeled ER open flux is of the order of 10% of the total open flux. We try to improve our simulation of the open flux by simply adding

Table 6.1: Number of emerging BMRs per cycle, the accumulated BMR area per cycle and the total amount of magnetic flux emerging during a cycle as obtained from the procedure described in Sect. 6.6.1. Note that the first and the last cycle are incomplete in the dataset.

Cycle	BMRs	Area [deg^2]	Flux [10^{25}Mx]	Cycle	BMRs	Area [deg^2]	Flux [10^{25}Mx]
11	492	9 470	0.122	18	7 060	113 668	1.385
12	3 172	55 737	0.699	19	9 995	151 264	1.802
13	5 452	73 461	0.835	20	9 665	108 851	1.129
14	5 236	61 488	0.653	21	6 084	100 808	1.240
15	8 488	79 031	0.720	22	7 676	107 297	1.239
16	6 924	76 157	0.779	23	6 236	85 007	0.971
17	7 796	107 806	1.239				

the ER open flux of Solanki et al. (2002b). The result is shown in Fig. 6.15 b. The combination of the two models matches the reconstructed IMF better than the open flux derived from active regions alone. The secular trend of the open flux minima is now present in the combined model, however, still not that strong as observed. A small phase shift between the reconstructed IMF and the modelled open flux is still present. Furthermore, it is surprising that the largest discrepancies between model and observation occur during the last two cycles. This might be due to a systematic error between the RGO dataset (concluded in 1976) and the USAF data, which underly the simulations.

The amplitudes of the cycles $17-19$ happen to be too large. The reason for this could be that our method of transforming the sunspot group data into an active region sequence (Sect. 6.6.1) overestimates the total cycle flux for these cycles. These three cycles were particularly strong with large sunspot groups so that the magnetic flux associated with these large sunspot groups in our simulations might be too large.

6.7 Conclusion

Our aim was to model the historical solar surface magnetic field, the polar fields and the open flux on the basis of the RGO/USAF sunspot data. The simulation of the surface field with the extended flux transport model yields rather good results which shows the comparison with observations where available.

In order to understand the dependence and evolution of the open flux on the surface magnetic field, we investigated the open flux obtained from the PFSS model for different constant and time-varying source surface radii. It turned out that for a source surface radius of $R_{\rm ss} = 2.5 R_\odot$, as is generally accepted, not enough magnetic flux originating

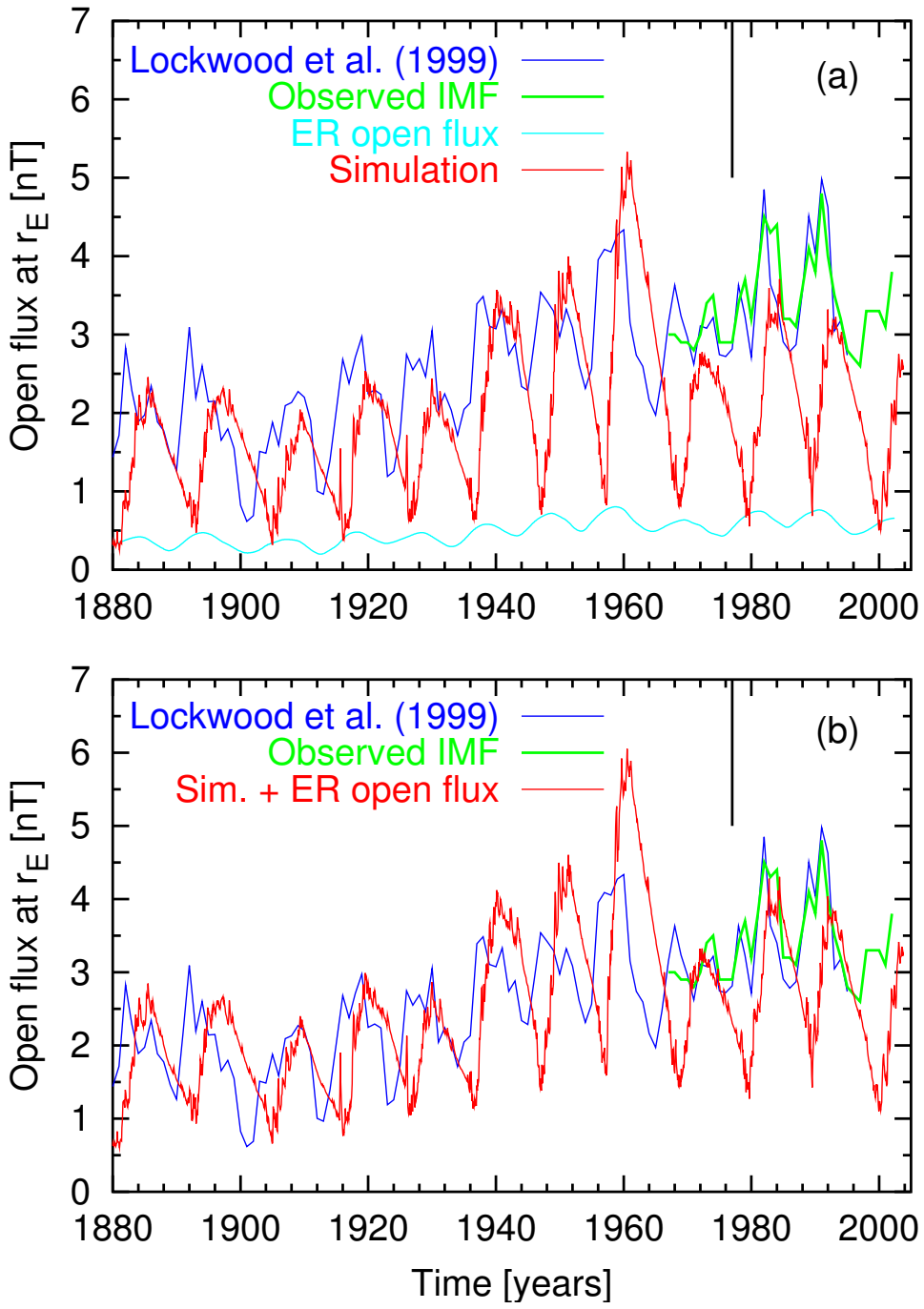

Figure 6.15: (a) Open flux simulated on the basis of the RGO sunspot database using the CSSS model with $R_{\rm cusp} = 1.6R_\odot$ and $R_{\rm ss} = 2.5R_\odot$. The yearly averaged radial IMF component for 1969-2002 is obtained from the NSSDC OmniWeb database and the reconstruction of the IMF is taken from Lockwood et al. (1999). The fraction of open flux originating from ephemeral regions obtained from the model of Solanki et al. (2002b) is also shown. (b) Open flux obtained from the simulation combined with the ER open flux together with the reconstruction of Lockwood et al. (1999) and the measured IMF.

from low latitudes penetrates through the source surface and thus contributes to the open flux. In this case the open flux is mainly dominated by the flux originating from the polar regions. Better agreement with the observed open flux distribution is yielded by reducing the source surface to $\sim 1.6 R_{\odot}$. The more complex CSSS model leads to similar results for the total open flux as the PFSS model, however, the heliospheric topology is reproduced better in this model.

The attempt to model the historical open flux on the basis of the RGO data yields rather poor results. The simulated open flux is shifted backward in time and the open flux minima are much too low with respect to the reconstructed IMF. An improvement is achieved when we add the open flux contribution of ephemeral regions. By doing so, the phase difference between simulation and observation is reduced and the secular increase of the open flux minima is obtained.

7 On the size distribution of sunspot groups in the Greenwich sunspot record 1874-1976

7.1 Introduction

Sunspots appear dark on the solar surface and typically last for several days, although very large ones may live for several weeks. Sunspots are concentrations of magnetic flux, with magnetic field strengths of the order of kG. Usually, sunspots come in groups containing two sets of spots of opposite magnetic polarity. The field is strongest in the darker parts of the sunspots, the umbra. In the lighter part, the penumbra, the field is weaker and more horizontal.

The size spectrum of sunspots ranges from 3 MSH (micro solar hemispheres) for the smallest (Bray and Loughhead 1964) to more than 3 000 MSH for very large sunspots. Smaller sunspots are more common than larger ones. A quantitative study of the size distribution of sunspot umbrae has been presented by Bogdan et al. (1988). They found a log-normal size distribution by analysing a dataset of more than 24 000 Sunspots from Mt. Wilson white-light images. The ratio of umbral to penumbral area depends only very slightly on the sunspot size (see the references and discussion in Solanki (2003)) so that such a distribution can be expected to be valid for sunspots as a whole. Since Bogdan et al. (1988) used all sunspot observations in their sample to determine their size distribution and many sunspots live multiple days, the same sunspot appears multiple times in their statistics. Furthermore, in the course of its evolution, the size of a sunspot changes. Hence the method of Bogdan et al. (1988) provides the instantaneous distribution of sunspot sizes at any given time (let us call it the snapshot distribution). This, however, does not in general correspond to the initial size distribution of sunspots, i.e. the distribution of the maximum sizes of sunspots, given that sunspots grow very fast and decay very slow. For many purposes, however, the latter distribution is the more useful one. An example is when the total amount of magnetic flux appearing on the solar surface in the form of sunspots needs to be estimated (since the field strength averaged over a full sunspot is remarkably constant, Solanki and Schmidt (1993), the sunspot area is a good measure of the total magnetic flux.)

The purpose of this chapter is to determine the distributions of both, the instantaneous sizes and the maximum sizes, and to compare these with each other. We determine the size distribution function of sunspot umbrae and of total sunspot areas from the digitized version of the daily sunspot observations of the Royal Greenwich Observatory (RGO).

7.2 Dataset and analysis procedure

The GPR (Greenwich Photoheliographic Results) provide the longest and most complete record of sunspot areas, spanning observations from May 1874 to the end of 1976. However, only the areas of complete sunspot groups and not of individual sunspots have been regarded. The area covered by the sunspots of a group is measured every time it is observed, i.e. at every development stage of its sunspots accessed by observations. In addition, the sunspot group is followed until it has reached its maximum area. This area is stored separately. We employ in all cases true areas corrected for projection effects.

These stored areas can now be used to derive two different distributions of sunspot area. If we simply form the distribution obtained from all the measured areas, we obtain the average distribution of sunspot sizes at any random instance. We call this the *snapshot method*. The snapshot method also underlies the study of Bogdan et al. (1988). In general, this instantaneous size of a sunspot group will be smaller than the size of the sunspot group at its full development. The maximum size is usually reached early in the development of a sunspot or sunspot group. It is followed by a steady decay (McIntosh 1981).

In the second method, hereafter called *maximum development method*, the area of a sunspot group is taken at the time when the group has reached its maximum area.
The maximum group area A_0 determined from the Greenwich data is in general too small. Since only one observation per day is available and thus the maximum area of the spot group can be reached several hours before or after the measurement. As we consider spot groups, the different spots in the group may reach their maximum area at different times. Therefore A_0 is in general somewhat smaller than the sum of the maximum areas of all the sunspots in the group. The area distribution of individual sunspots can be partly estimated by considering separately just groups of type 0, i.e. those containing just a single spot.

Also, visibility and projection effects lead to too small areas in the observations (Kopecký et al. 1985) affecting both distributions. The RGO dataset that we use is already corrected for foreshortening. Nevertheless, in order to minimize the errors resulting from visibility corrections we use only spot groups measured within $\pm 30\,^\circ$ from the central meridian. When determining the maximum area of a sunspot group, we make sure that the maximum extent is reached within $\pm 30\,^\circ$ although the sunspot group does not necessarily have to be born within this angle.

We divide the dataset into bins. Our criteria for the bin width is 20 % of the geometric mean area of the bin. We replace the continuous size distribution function $\mathrm{d}N/\mathrm{d}A$ by the discrete approximation $\Delta N/\Delta A$, where ΔA is the bin width and ΔN is the raw count of the bin.

We include in our analysis only sunspot groups whose areas exceed a lower cut-off limit $A_{\min}$. For umbral areas we set the limit to $A_{\min}^{\mathrm{umb}} = 15$ MSH (similar to Martínez Pillet et al. (1993)) and for total spot areas to $A_{\min}^{\mathrm{tot}} = 60$ MSH. Smaller areas than $A_{\min}$ are not taken into account in this study, as they are falsified from enhanced intrinsic measurement errors as well as from distortions due to atmospheric seeing.

In order to make the size distributions for different datasets comparable, we divide $\Delta N/\Delta A$ by the total number of spots exceeding $A_{\min}$. This corresponds to a normalization

$$\int_{A_{\min}}^{\infty} \frac{\mathrm{d}N}{\mathrm{d}A}\mathrm{d}A = 1\,. \tag{7.1}$$

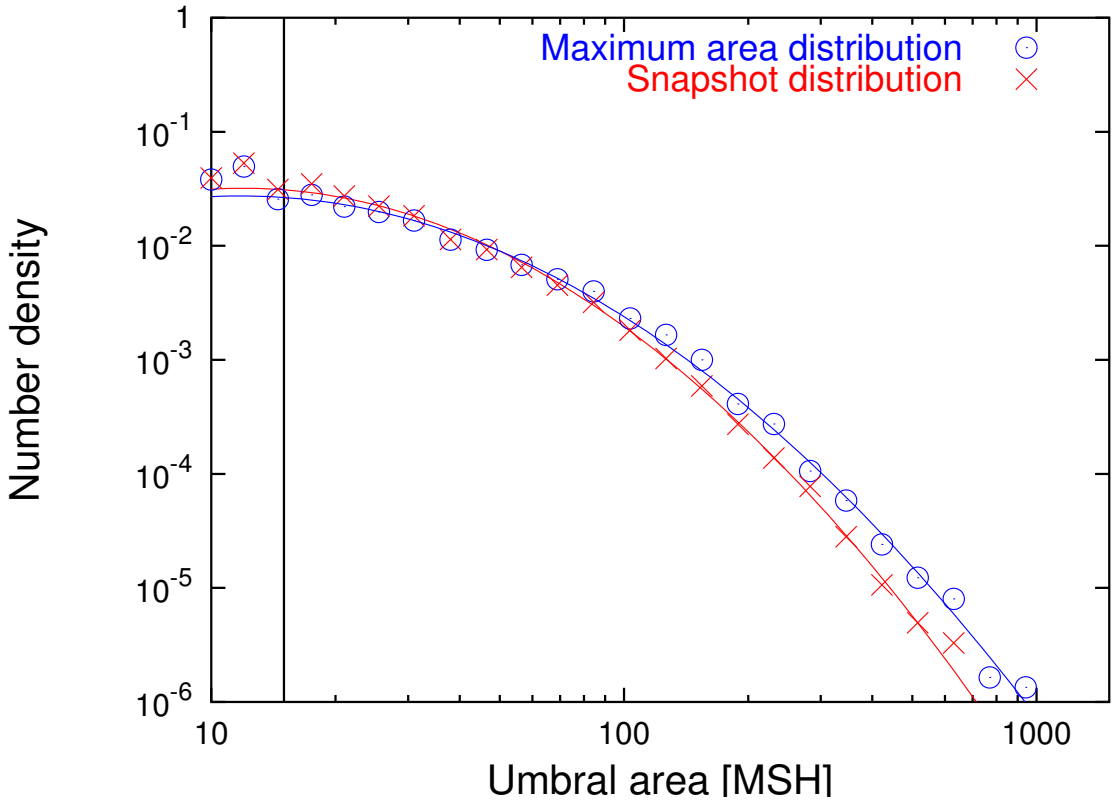

Figure 7.1: Size distribution function of umbral areas obtained from the maximum development method (*circles*) and snapshot method (*crosses*). The log-normal fits are overplotted (*blue line:* Fit to maximum area distribution, *red line:* Fit to snapshot distribution). The vertical line indicates the lower area cut-off.

Finally, we fit each empirical distribution with an analytical function. Following Bogdan et al. (1988) we employ a log-normal function, i.e. a continuous distribution in which the logarithm of a variable has a normal distribution. The general form of a log-normal distribution is

$$\ln\left(\frac{\mathrm{d}N}{\mathrm{d}A}\right) = -\frac{(\ln A - \ln\langle A\rangle)^2}{2\ln\sigma_A} + \ln\left(\frac{\mathrm{d}N}{\mathrm{d}A}\right)_{\max}, \tag{7.2}$$

where $(\mathrm{d}N/\mathrm{d}A)_{\max}$ is the maximum value reached by the distribution, $\langle A\rangle$ is the mean area and σ_A is a measure for the width of the log-normal distribution. Note that a log-normal function appears as a parabola in a log-log plot.

Log-normal distributions have been found in various fields of natural sciences. Examples of variates which are log-normally distributed are the size of silver particles in a photographic emulsion, the survival time of bacteria in disinfectants or aerosols in industrial atmospheres (Crow and Shimizu 1988), or, within solar physics, the distribution of radiances in the quiet Sun (Pauluhn et al. 2000).

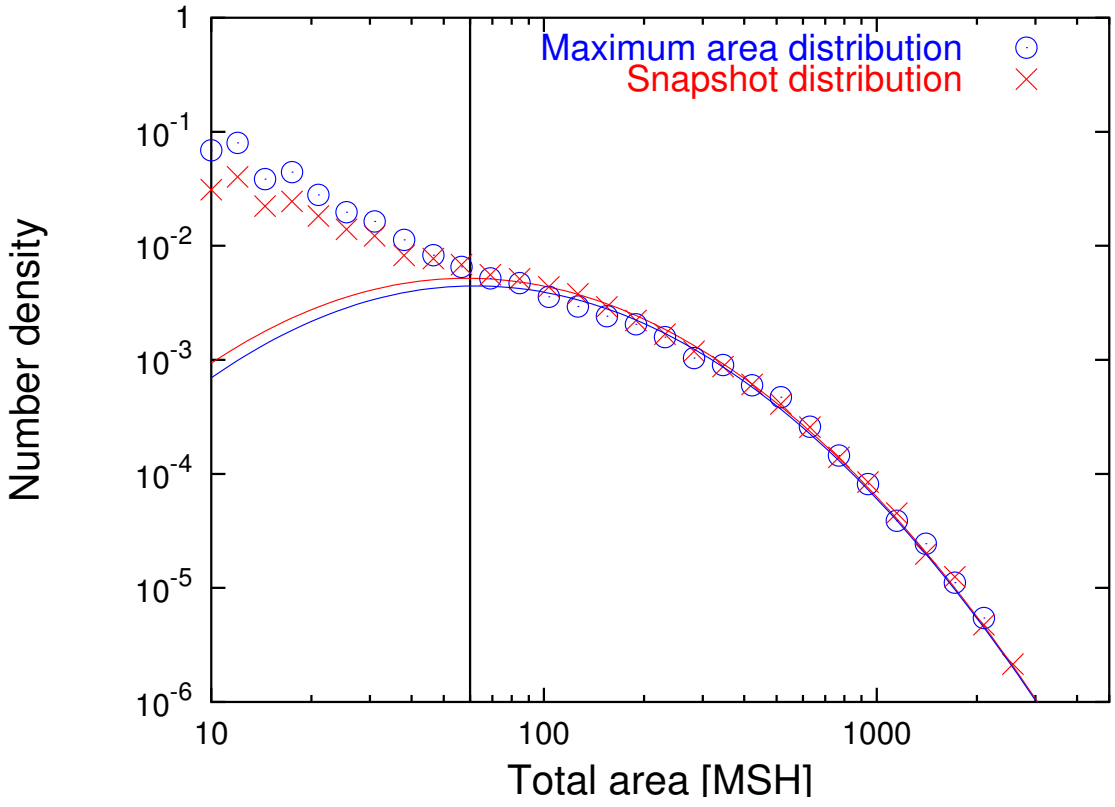

Figure 7.2: Size distribution function of the total spot group areas (umbra+penumbra) obtained from the maximum development method (*circles*) and the snapshot method (*crosses*). Overplotted are the log-normal fits for $A > 60$ MSH (*blue line*: Maximum development method, *red line*: Snapshot method).

7.3 Results for RGO spot group areas

7.3.1 Umbrae

The size distributions for the umbral area obtained from both, the snapshot method and the maximum development method, are shown in Fig. 7.1. For both methods, the resulting size distribution is well described by a log-normal function above the lower cut-off $A_{\min}$. As one would expect, the curve of the maximum areas lies above the snapshot curve for large sunspots. For smaller areas, the snapshot distribution is higher, resulting from the fact that the areas obtained with the snapshot method are smaller (since they include sunspots at different stages of decay), thus leading to more counts for smaller areas. The fit parameters are listed in Table 7.1. It is surprising that the size distributions obtained by both methods do not differ by a larger amount than suggested by Fig. 7.1. In general, the two distributions are expected to be more similar to each other if the lifetime of sunspots approaches the sampling time of the data, i.e. 1 day. For sunspots with shorter lifetimes both methods should give identical results. Therefore, the small difference between the two distributions is consistent with relatively short average lifetimes of sunspots.

The sunspot area measurements are not uniform across datasets. The umbral areas for

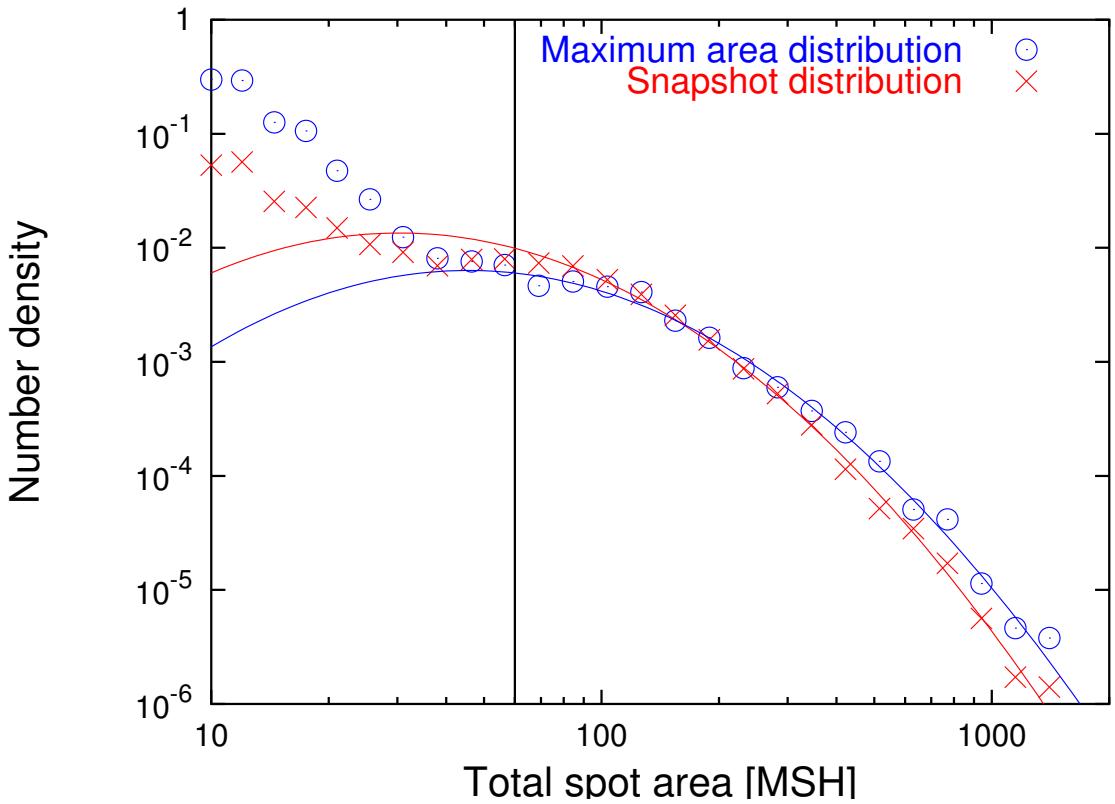

Figure 7.3: Maximum area distribution (*circles*) and snapshot distribution (*crosses*) of total spot areas for single spots. Fits to the data for $A > 60$ MSH: maximum development method (*blue line*), snapshot method (*red line*).

single spots from RGO are roughly a factor of 2-3 larger than the corresponding areas from the Mt. Wilson white light plate collection. This difference combined with the fact that the RGO areas are sunspot group areas leads to a shift of the area distribution towards higher values of $\langle A \rangle$ and smaller values of σ_A (Table 7.1) than derived from the Mt. Wilson dataset. The smaller value of σ_A results from the logarithmic nature of the distribution.

7.3.2 Total areas

Fig. 7.2 shows the distributions for the total spot areas, i.e. the sum of umbral and penumbral area. The log-normal fit matches both distributions rather well above the cut-off. However, both distributions differ even less than for the case where only the umbrae are considered (Fig. 7.1). Especially in the large area regime, the fits for both distributions are almost indistinguishable. Since every sunspot must have an umbra, it is not clear why the difference between the two distributions in Fig. 7.2 is smaller than in Fig. 7.1, unless it is an indication of the limits of the accuracy of the data. It may also be indicating that the decay law may be different for umbrae and sunspots.

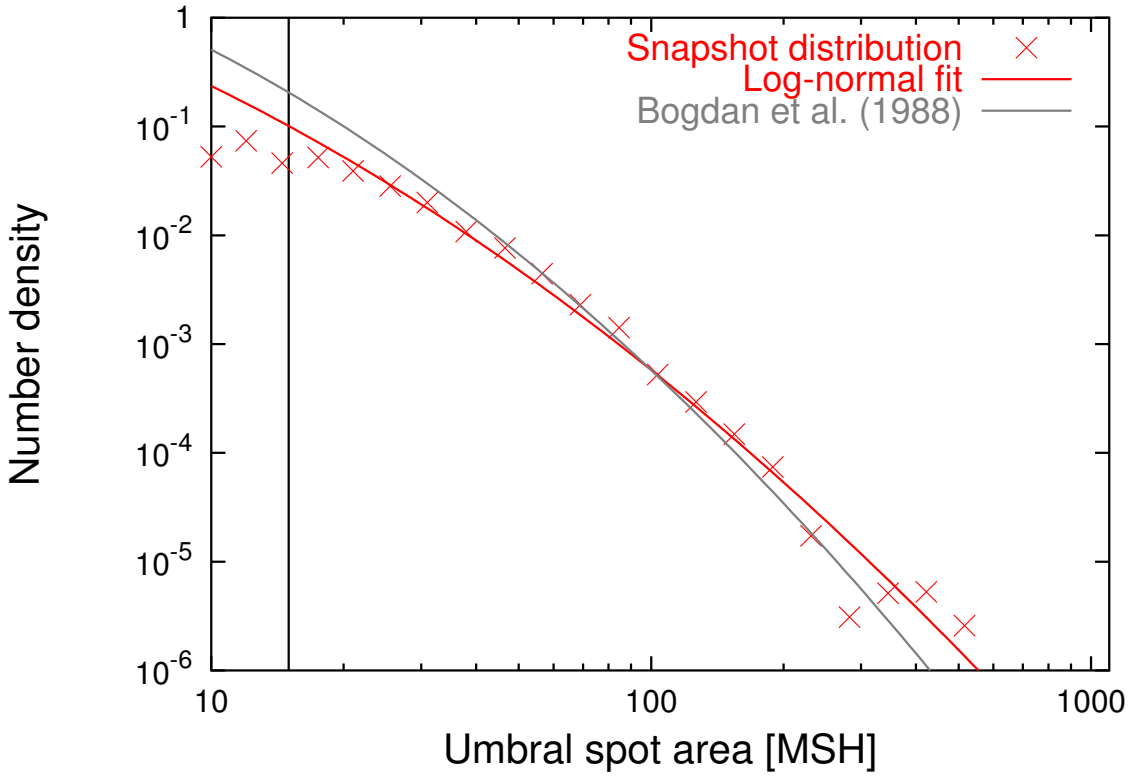

Figure 7.4: Snapshot distribution of umbral spot areas for single spots (*crosses*), fit to the data (*red line*) and the curve from Bogdan et al. (1988) (*grey line*).

7.3.3 Total area of single spots

In this part of the study, we have extracted only Greenwich sunspot groups of type 0, i.e. single spots (Fig. 7.3). In order to get a statistically significant dataset, we have to extend our longitudinal constraints to $\pm 60^\circ$ around disk center.

The difference between the snapshot and the maximum area distribution is more pronounced for total areas of single spots than for total areas of all sunspot groups. The difference in the two distributions can be explained by a similar argumentation as in Sect. 7.3.1. The maximum distribution dominates for large areas, whereas the snapshot distribution shows more counts for smaller areas due to the inclusion of different decay stages of the sunspots. The similarity between Figs. 7.3 and 7.1 suggests that the problem lies with Fig. 7.2. It may be that when determining the total area of sunspot groups, areas of the generally short-lived pores were included.

7.3.4 Umbral areas of single spots

Of special interest is the snapshot distribution of umbral areas of single spots (Fig. 7.4) because this can directly be compared to the results from Bogdan et al. (1988). The RGO dataset displays a significant flatter distribution than the Mt. Wilson data, i.e. the ratio of large umbrae to small umbrae is bigger for the RGO data. This systematic difference

Table 7.1: Overview of the log-normal fit parameters. Due to the normalization (7.1) there are only two free parameters $\langle A \rangle$ and σ_A.

Data Set	Method	$\langle A \rangle$	σ_A	Sunspots or Groups	Fig.
Mt. Wilson Umbrae	Bogdan et al.	0.62	3.80	24 615	7.4
Umbrae	Max. developement	11.8	2.55	3 966	7.1
Umbrae	Snapshot	12.0	2.24	31 411	7.1
Total area	Max. developement	62.2	2.45	3 926	7.2
Total area	Snapshot	58.6	2.49	34 562	7.2
Total area single spots	Max. developement	45.5	2.11	939	7.3
Total area single spots	Snapshot	30.2	2.14	15203	7.3
Umbral area single spots	Snapshot	0.27	6.19	11312	7.4
Model	Max. developement	11.8	2.55	807 771	7.5 a
Model	Snapshot				
	hourly	7.77	2.80	21 352 828	7.5 a
	daily	8.67	2.73	1 092 295	7.5 a
	3 days	9.89	2.69	525 605	7.5 a

between the data sets is an indication of a systematic difference between sunspots in groups of type 0 and other spots. The parameter $\langle A \rangle$ is roughly a factor of 2 smaller than in the corresponding Mt. Wilson data, while the width of the distribution is larger.

7.4 Modelling the snapshot distribution

7.4.1 Model description

We have developed a simple sunspot decay model that simulates the snapshot distribution resulting from a given maximum area distribution. One aim of this modelling effort is to find out to what extend it is possible to distinguish between decay laws from the difference between the maximum area and the snapshot area distributions. Another aim is to test if, with decay laws as published in the literature, both the maximum and snapshot area distributions must have the same functional form.

We consider two kinds of maximum development distributions: a lognormal distribution (7.2) and a power-law distribution of the general form

$$h(A) = v \cdot A^w \,. \tag{7.3}$$

The maximum area distributions are provided by a random number generator for the desired parameters v, w or $(\mathrm{d}N/\mathrm{d}A)_{\max}$, $\langle A \rangle$ and σ_A, respectively. We assume an emergence rate of 10 000 spots per day. The absolute number of emerging spots does not influence the results as they are normalized and this high number is chosen in order to obtain statistically significant distributions. The constant emergence rate is a reasonable approximation of the solar case during a small period of time, i.e a few months, which is the length of time over which we let the model run.

Once the spots have emerged they begin to decay immediately (the formation time of spots is short, i.e. hours (Solanki 2003), and is thus neglected in the model). Petrovay and van Driel-Gesztelyi (1997) showed that the decay rate of a sunspot is related to its radius r_{S} and thus is parabolic and not linear as was proposed in earlier works (e.g. Bumba, 1963). The quadratic decay is also favored by models that explain the erosion of a sunspot as magnetic flux loss at the spot boundary (Meyer et al. 1974). A universal decay law describing the erosion of a large sample of spots does not exist. Howard (1992) and Martínez Pillet et al. (1993) found that the sunspot decay rates are log-normally distributed. Combining the latter results, we implement a parabolic decay law of the form

$$A(t) = \left(\sqrt{A_0} - \frac{D}{\sqrt{A_0}} \left(t - t_0 \right) \right)^2 \tag{7.4}$$

and $A(t - t_0 > A_0/D) = 0$. The decay rates D are obtained from a random number generator providing a log-normal distribution with a mean $\mu = 1.75$ and a variance $\sigma^2 = 2$.

Combining the maximum area distribution with the decay law (Eq. 7.4) we can determine the resulting snapshot distribution. We simulate an interval of 100 days after an initialization time of 100 days in order to make sure that a reasonable mix of old, partly decayed spots and newly emerged spots is present. We take the fit parameters for the umbral maximum development distribution from Sect. 7.3 as the starting distribution of our model.

7.4.2 Results from the model

The resulting snapshot distributions for a quadratic decay law of the form Eq. (7.4) with log-normally distributed decay rates are derived for 3 different sampling times (Fig. 7.5 a).

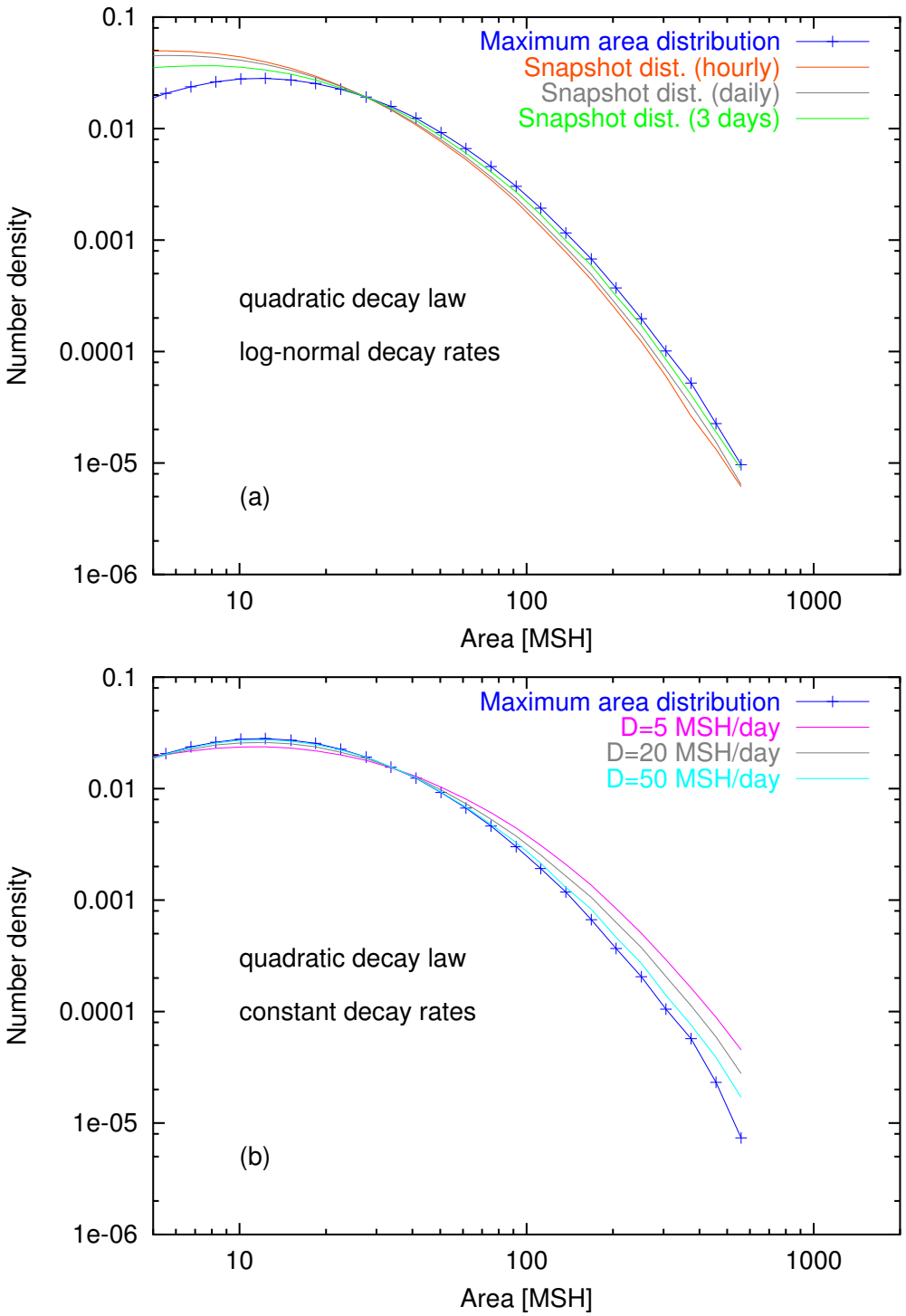

Figure 7.5: Results from the model for a quadratic decay-law for (a) log-normally distributed decay rates and sampling times of 1 hour, 1 day and 3 days and (b) for constant decay rates $D = 5$ MSH/day, $D = 20$ MSH/day and $D = 50$ MSH/day and a sampling time of 1 day.

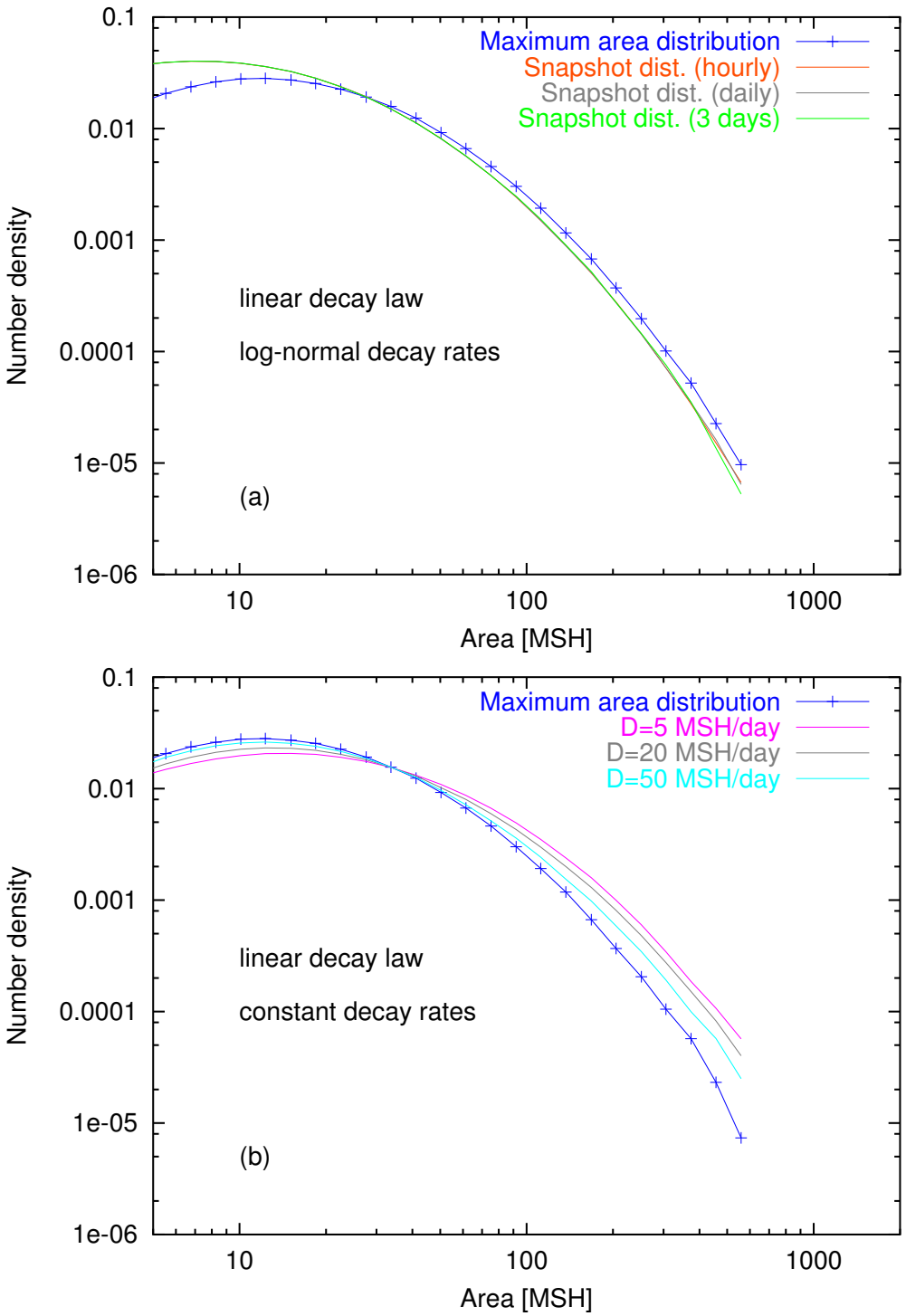

Figure 7.6: Results from the model for a linear decay-law for (a) log-normally distributed decay rates and sampling times of 1 hour, 1 day and 3 days and (b) for constant decay rates $D = 5$ MSH/day, $D = 20$ MSH/day and $D = 50$ MSH/day and a sampling time of 1 day

It is striking that the snapshot distributions can be fitted well by log-normal functions. A sampling rate of 1 day corresponds to the RGO dataset and thus can be compared with the results for umbral areas in Fig. 7.1. The modelled snapshot distribution matches quite well the observed snapshot distribution above the cut-off limit. Changing the sampling rate to 3 days, both distributions, maximum development and snapshot, merge closer together and become almost identical. The explanation therefore is, that the observing intervals become comparable to the lifetime of the spots which makes it at some stage impossible to distinguish between the two distributions. If, however, we were to increase the observing frequency to 1 hour, a sampling frequency provided by the MDI dataset, both distributions differ more from each other as more decay stages of the spots are included in the snapshot data. When considering such a short sampling interval the formation time of the spot group becomes important and has to be taken into account, which is not included in our model.

In the next step, we replace the log-normally distributed decay-rates in Eq. (7.4) by constant decay rates (Fig. 7.5 b). It is interesting that for all constant decay rates the snapshot distribution curves lie above the maximum area distribution for large areas. For a high decay rate (i.e. 50 MSH/day) both distribution curves merge closer together than for small decay rates (i.e. 5 MSH/day). This is understandable because a small decay rate affects more the smaller spots than the larger spots. A variability of the decay rates (log-normal distribution) thus seems necessary to yield the generally observed behaviour that the maximum area curve in general lies above the snapshot curve.

In order to see how the decay law affects the results, we replace (7.4) by a linear decay law of the form

$$A(t) = A_0 - D\,(t - t_0) \tag{7.5}$$

and $A(t - t_0 > A_0/D) = 0$. As for the case of the quadratic decay law, we once use log-normally distributed decay rates in Eq. (7.5) and investigate different sampling times (Fig. 7.6 a) and once we use different constant decay rates (Fig. 7.6 b). Qualitatively, a similar behaviour for both cases can be observed as in the case of a quadratic decay-law, i.e. for constant decay rates the snapshot distributions lie above the maximum area curve. When using log-normally distributed decay rates in the linear decay law (Eq. 7.5), the resulting snapshot curves for the three different sampling times are almost not distinguishable. We conclude from our model that it is not possible to distinguish between a linear and a quadratic decay-law by this analysis.

Of interest is to see if a power-law distribution of the maximum development areas would also lead to a log-normal snapshot distribution. A power-law size distribution with an exponent -2 has been found by Harvey (1993) for active regions using Kitt Peak magnetograms. Since active regions harbour sunspots, it might be worth testing if the maximum area distribution is similar to or very different from that of the host active regions. To this purpose we insert a maximum size distribution $\mathrm{d}N/\mathrm{d}A \sim A^{-2}$ in our model. This does not yield a log-normal snapshot distribution but rather something very close to a power-law. To make sure that this result is not an artefact of the special choice of the exponent of the power-law, we ran the same simulations with powers between -1.0 and -3.0. In all cases we can exclude a transformation of the power-law distribution for the maximum areas into a log-normal snapshot distribution.

7.5 Conclusion

The size distribution for both, umbral and total spot area, obtained from the snapshot method and the maximum area distribution have a pronounced, smooth log-normal shape above our lower cut-off limit. The results for the maximum development method show clearly that neither the umbral areas nor the total spot areas have a power-law distribution as one might expect from similar studies of active regions. Harvey and Zwaan (1993) found a size distribution of bipolar active regions $\sim A^{-2}$ where their study is equivalent to our maximum development method. When modelling the snapshot distribution from a given maximum development distribution via a quadratic decay of the spot areas, both distributions become more distinct with higher sampling frequencies. Log-normally distributed decay-rates seem to be necessary to model qualitatively the observed snapshot distributions. A linear decay law in our model yields qualitatively similar results as a quadratic decay-law making it impossible to distinguish between them by this analysis.

8 Comments and outlook

- In general, flux transport models assume a one-cell meridional flow. However, reports about a possible multi-cell meridional circulation, at least temporally, come from helioseismology (Haber et al. 2002). The influence of a two-cell meridional circulation in the flux transport model on the evolution of the large-scale magnetic field was investigated by McDonald and Dikpati (2004). As a result of the second meridional flow cell flux is advected away from the pole and flux from the active region belts is prevented from reaching the poles leading to a strong decrease of the polar fields.

- The parameter study (Sect. 4) provides a good understanding of the influence of solar cycle parameters on the global magnetic field. It would be of interest to simulate the evolution of the surface magnetic field for specific active stars using realistic parameters in the flux transport model. An attempt to simulate the magnetic field evolution of AB Dor has been made by Mackay et al. (2004).

- A potential field extrapolation from the surface field calculated with the flux transport model does not reproduce the historic open flux record when using only active regions as sources of new magnetic flux. A combination with the open flux of ephemeral regions improves the IMF modeling. In this thesis, we did this simply by adding the ER open flux obtained by a different model. It would be interesting to include ER as additional sources in the flux transport model in order to see if this also leads to an improved open flux simulation.

- Potential field methods need to be improved in order to yield a better agreement of the calculated open flux and the observed IMF. Once, when this is achieved, the sunspot record underlying the reconstruction could be extended even further back in time on the basis of the sunspot number, e.g. back to ~ 1650.

Bibliography

Altschuler, M. D., 1974, Magnetic Structure Responsible for Coronal Disturbances: Observations, in IAU Symp. 57: Coronal Disturbances, pp. 3–+

Altschuler, M. D., Newkirk, G., 1969, Magnetic Fields and the Structure of the Solar Corona. I: Methods of Calculating Coronal Fields, Sol. Phys., 9, 131–+

Balogh, A., Smith, E. J., 2001, The Heliospheric Magnetic Field at Solar Maximum: Ulysses Observations, Space Science Reviews, 97, 147–160

Baumann, I., Schmitt, D., Schüssler, M., Solanki, S. K., 2004, Evolution of the large-scale magnetic field on the solar surface: a parameter study, A&A, 426, 1075–1091

Berdyugina, S. V., Usoskin, I. G., 2003, Active longitudes in sunspot activity: Century scale persistence, A&A, 405, 1121–1128

Bogart, R. S., 1987, Large-scale motions on the Sun - an overview, Sol. Phys., 110, 23–34

Bogdan, T. J., Low, B. C., 1986, The three-dimensional structure of magnetostatic atmospheres. II - Modeling the large-scale corona, ApJ, 306, 271–283

Bogdan, T. J., Gilman, P. A., Lerche, I., Howard, R., 1988, Distribution of sunspot umbral areas - 1917-1982, ApJ, 327, 451–456

Bray, R. J., Loughhead, R. E., 1964, Sunspots, The International Astrophysics Series, London: Chapman & Hall, 1964

Bullard, E. C., Gellman, H., 1954, Homogeneous dynamos and terrestrial magnetism, Phil. Trans. Roy. Soc., A 247, 213–278

Bumba, V., 1963, Development of SPOT group areas in dependence on the local magnetic field, Bull. Astron. Inst. Czechoslovakia, 14, 91–+

Chapman, G. A., Cookson, A. M., Dobias, J. J., 1997, Solar Variability and the Relation of Facular to Sunspot Areas during Solar Cycle 22, ApJ, 482, 541–545

Choudhuri, A. R., Dikpati, M., 1999, On the large-scale diffuse magnetic field of the Sun - II.The Contribution of Active Regions, Sol. Phys., 184, 61–76

Crow, E. L., Shimizu, K. E., 1988, Lognormal Distributions: Theory and Applications, Dekker, New York

DeVore, C. R., Sheeley, N. R., 1987, Simulations of the Sun's polar magnetic fields during sunspot cycle 21, Sol. Phys., 108, 47–59

DeVore, C. R., Boris, J. P., Sheeley, N. R., 1984, The concentration of the large-scale solar magnetic field by a meridional surface flow, Sol. Phys., 92, 1–14

DeVore, C. R., Boris, J. P., Young, T. R., Sheeley, N. R., Harvey, K. L., 1985a, Numerical simulations of large-scale solar magnetic fields, Australian Journal of Physics, 38, 999–1007

DeVore, C. R., Sheeley, N. R., Boris, J. P., Young, T. R., Harvey, K. L., 1985b, Simulations of magnetic-flux transport in solar active regions, Sol. Phys., 102, 41–49

Dikpati, M., Choudhuri, A. R., 1994, The evolution of the Sun's poloidal field, A&A, 291, 975–989

Dikpati, M., de Toma, G., Gilman, P. A., Arge, C. N., White, O. R., 2004, Diagnostics of Polar Field Reversal in Solar Cycle 23 Using a Flux Transport Dynamo Model, ApJ, 601, 1136–1151

Duvall, T. L., 1979, Large-scale solar velocity fields, Sol. Phys., 63, 3–15

Elsasser, W. M., 1946, Induction Effects in Terrestrial Magnetism, Phys. Rev., 69, 106–116

Fisk, L. A., Schwadron, N. A., 2001, The Behavior of the Open Magnetic Field of the Sun, ApJ, 560, 425–438

Foukal, P., Lean, J., 1988, Magnetic modulation of solar luminosity by photospheric activity, ApJ, 328, 347–357

Haber, D. A., Hindman, B. W., Toomre, J., Bogart, R. S., Larsen, R. M., Hill, F., 2002, Evolving Submerged Meridional Circulation Cells within the Upper Convection Zone Revealed by Ring-Diagram Analysis, ApJ, 570, 855–864

Hale, G. E., Nicholson, S. B., 1925, The Law of Sun-Spot Polarity, ApJ, 62, 270–+

Hale, G. E., Ellerman, F., Nicholson, S. B., Joy, A. H., 1919, The Magnetic Polarity of Sun-Spots, ApJ, 49, 153–+

Harvey, K., 1993, Magnetic Bipoles on the Sun, Ph.D. thesis, Astron. Inst. Utrecht Univ.

Harvey, K. L., 1992, The Cyclic Behavior of Solar Activity, in ASP Conf. Ser. 27: The Solar Cycle, pp. 335–+

Harvey, K. L., Zwaan, C., 1993, Properties and emergence of bipolar active regions, Sol. Phys., 148, 85–118

Hathaway, D. H., 1996, Doppler Measurements of the Sun's Meridional Flow, ApJ, 460, 1027–+

Hathaway, D. H., Wilson, R. M., Reichmann, E. J., 1994, The shape of the sunspot cycle, Sol. Phys., 151, 177–190

Hoeksema, J. T., Wilcox, J. M., Scherrer, P. H., 1983, The structure of the heliospheric current sheet - 1978-1982, J. Geophys. Res., 88, 9910–9918

Howard, R. F., 1992, The growth and decay of sunspot groups, Sol. Phys., 137, 51–65

Kippenhahn, R., Möllenhoff, C., 1975, Elementare Plasmaphysik, Bibliogr. Inst., first edn.

Kopecký, M., Kuklin, G. V., Starkova, I. P., 1985, The visibility function and its effect on the observed characteristics of sunspot groups. I - Diagram of observational conditions of sunspot groups, Bull. Astron. Inst. Czechoslovakia, 36, 189–198

Krause, F., Rädler, K. H., 1980, Mean-Field Magnetohydrodynamics and Dynamo Theory, Akademie-Verlag Berlin, first edn.

Krivova, N. A., Solanki, S. K., 2004, Effect of spatial resolution on estimating the Sun's magnetic flux, A&A, 417, 1125–1132

Leighton, R. B., 1964, Transport of Magnetic Fields on the Sun., ApJ, 140, 1547–+

Lockwood, M., Stamper, R., Wild, M. N., 1999, A doubling of the Sun's coronal magnetic field during the past 100 years., Nature, 399, 437–439

Mackay, D. H., Priest, E. R., Lockwood, M., 2002a, The Evolution of the Sun's Open Magnetic Flux - I. A Single Bipole, Sol. Phys., 207, 291–308

Mackay, D. H., Priest, E. R., Lockwood, M., 2002b, The Evolution of the Sun's Open Magnetic Flux - II. Full Solar Cycle Simulations, Sol. Phys., 209, 287–309

Mackay, D. H., Jardine, M., Cameron, A. C., Donati, J.-F., Hussain, G. A. J., 2004, Polar caps on active stars: magnetic flux emergence and transport, MNRAS, 354, 737–752

Makarov, V. I., Tlatov, A. G., Sivaraman, K. R., 2003, Duration of Polar Activity Cycles and Their Relation to Sunspot Activity, Sol. Phys., 214, 41–54

Martínez Pillet, V., Moreno-Insertis, F., Vázquez, M., 1993, The distribution of sunspot decay rates, A&A, 274, 521–+

Martinez Pillet, V., Lites, B. W., Skumanich, A., 1997, Active Region Magnetic Fields. I. Plage Fields, ApJ, 474, 810–+

McDonald, E., Dikpati, M., 2004, Evolution of Large-scale Solar Magnetic Fields in the Presence of a Multi-cell Meridional Flow, American Astronomical Society Meeting Abstracts, 204, –+

McIntosh, P. S., 1981, The birth and evolution of sunspots - Observations, in The Physics of Sunspots, pp. 7–54, L. Cram, J.H. Thomas (Eds.), NSO, Sunspot, N.M.

Meyer, F., Schmidt, H. U., Wilson, P. R., Weiss, N. O., 1974, The growth and decay of sunspots, MNRAS, 169, 35–57

Mosher, J. M., 1977, The magnetic history of solar active regions, Ph.D. thesis, California Institute of technology

Nash, A. G., Sheeley, N. R., Wang, Y.-M., 1988, Mechanisms for the rigid rotation of coronal holes, Sol. Phys., 117, 359–389

Ossendrijver, M., 2003, The solar dynamo, A&A Rev., 11, 287–367

Pauluhn, A., Solanki, S. K., Rüedi, I., Landi, E., Schühle, U., 2000, Statistics of quiet Sun extreme ultraviolet intensities, A&A, 362, 737–745

Petrovay, K., van Driel-Gesztelyi, L., 1997, Making Sense of Sunspot Decay. I. Parabolic Decay Law and Gnevyshev-Waldmeier Relation, Sol. Phys., 176, 249–266

Pozrikidis, C., 1998, Numerical Computation in Science and Engineering, Oxford University Press, first edn.

Press, W. H., Flannery, B. P., Teukolsky, S. A., Vetterling, W. T., 1992, Numerical Recipes: The Art of Scientific Computing, Cambridge University Press, Cambridge (UK) and New York, 2nd edn., ISBN 0-521-43064-X

Priest, E. R., 1982, Solar Magnetohydrodynamics, D. Reidel Publishing Company, , Dordrecht, Holland, first edn.

Sakurai, T., 1982, Green's Function Methods for Potential Magnetic Fields, Sol. Phys., 76, 301–+

Schatten, K. H., 1972, Current Sheet Magnetic Model for the Solar Corona, in Solar Wind, pp. 44–+

Schatten, K. H., Wilcox, J. M., Ness, N. F., 1969, A model of interplanetary and coronal magnetic fields, Sol. Phys., 6, 442–455

Schrijver, C. J., 2001, Simulations of the Photospheric Magnetic Activity and Outer Atmospheric Radiative Losses of Cool Stars Based on Characteristics of the Solar Magnetic Field, ApJ, 547, 475–490

Schrijver, C. J., Harvey, K. L., 1994, The photospheric magnetic flux budget, Sol. Phys., 150, 1–2

Schrijver, C. J., Title, A., 2001, On the formation of polar spots in sun-like stars, ApJ, 551, 1099–1106

Schrijver, C. J., Title, A. M., van Ballegooijen, A. A., Hagenaar, H. J., Shine, R. A., 1997, Sustaining the Quiet Photospheric Network: The Balance of Flux Emergence, Fragmentation, Merging, and Cancellation, ApJ, 487, 424–+

Schrijver, C. J., DeRosa, M. L., Title, A. M., 2002, What Is Missing from Our Understanding of Long-Term Solar and Heliospheric Activity?, ApJ, 577, 1006–1012

Schüssler, M., Solanki, S. K., 1992, Why rapid rotators have polar spots, A&A, 264, L13–L16

Schüssler, M., Caligari, P., Ferriz-Mas, A., Solanki, S. K., Stix, M., 1996, Distribution of starspots on cool stars. I. Young and main sequence stars of $1M_{\odot}$., A&A, 314, 503–512

Schwabe, M., 1844, Sonnenbeobachtungen im Jahre 1843. Von Herrn Hofrath Schwabe in Dessau, Astronomische Nachrichten, 21, 233–+

Sheeley, N. R., DeVore, C. R., Boris, J. P., 1985, Simulations of the mean solar magnetic field during sunspot cycle 21, Sol. Phys., 98, 219–239

Slavin, J. A., Jungman, G., Smith, E. J., 1986, The interplanetary magnetic field during solar cycle 21 ISEE-3/ICE observations, Geophys. Res. Lett., 13, 513–516

Smith, E. J., Balogh, A., 1995, Ulysses observations of the radial magnetic field, Geophys. Res. Lett., 22, 3317–+

Snodgrass, H. B., 1983, Magnetic rotation of the solar photosphere, ApJ, 270, 288–299

Snodgrass, H. B., Dailey, S. B., 1996, Meridional Motions of Magnetic Features in the Solar Photosphere, Sol. Phys., 163, 21–42

Solanki, S. K., 1993, Smallscale Solar Magnetic Fields - an Overview, Space Science Reviews, 63, 1–+

Solanki, S. K., 2003, Sunspots: An overview, A&A Rev., 11, 153–286

Solanki, S. K., Schmidt, H. U., 1993, Are sunspot penumbrae deep or shallow?, A&A, 267, 287–291

Solanki, S. K., Schüssler, M., Fligge, M., 2000, Evolution of the Sun's large-scale magnetic field since the Maunder minimum , Nature, 408, 445–447

Solanki, S. K., Krivova, N. A., Schüssler, M., Fligge, M., 2002a, Search for a relationship between solar cycle amplitude and length, A&A, 396, 1029–1035

Solanki, S. K., Schüssler, M., Fligge, M., 2002b, Secular variation of the Sun's magnetic flux, A&A, 383, 706–712

Solanki, S. K., Usoskin, I. G., Kromer, B., Schüssler, M., Beer, J., 2004, Unusual activity of the Sun during recent decades compared to the previous 11,000 years, Nature, 431, 1084–1087

Stix, M., 1989, The Sun - An Introduction, Astronomy and Astrophysics Library (Springer Verlag), first edn.

Svalgaard, L., Duvall, T. L., Scherrer, P. H., 1978, The strength of the Sun's polar fields, Sol. Phys., 58, 225–239

Tannenbaum, B. S., 1967, Plasma Physics, McGraw-Hill Book Company, first edn.

Topka, K., Moore, R., Labonte, B. J., Howard, R., 1982, Evidence for a poleward meridional flow on the Sun, Sol. Phys., 79, 231–245

van Ballegooijen, A. A., Cartledge, N. P., Priest, E. R., 1998, Magnetic Flux Transport and the Formation of Filament Channels on the Sun, ApJ, 501, 866–881

Vilhu, O., Rucinski, S. M., 1983, Period-activity relations in close binaries, A&A, 127, 5–14

Wang, Y.-M., Sheeley, N. R., 1989, Average properties of bipolar magnetic regions during sunspot cycle 21, Sol. Phys., 124, 81–100

Wang, Y.-M., Sheeley, N. R., 1992, On potential field models of the solar corona, ApJ, 392, 310–319

Wang, Y.-M., Sheeley, N. R., 2002, Sunspot activity and the long-term variation of the Sun's open magnetic flux, Journal of Geophysical Research (Space Physics), 107, 10–1

Wang, Y.-M., Nash, A. G., Sheeley, N. R., 1989a, Evolution of the Sun's polar fields during sunspot cycle 21 - Poleward surges and long-term behavior, ApJ, 347, 529–539

Wang, Y.-M., Nash, A. G., Sheeley, N. R., 1989b, Magnetic flux transport on the Sun, Science, 245, 712–718

Wang, Y.-M., Lean, J., Sheeley, N. R., 2000a, The long-term variation of the Sun's open magnetic flux, Geophys. Res. Lett., 27, 505–508

Wang, Y.-M., Sheeley, N. R., J., Lean, J., 2000b, Understanding the evolution of the Sun's open magnetic flux, Geophys. Res. Lett., 27, 621–624

Wang, Y.-M., Lean, J., Sheeley, N. R., 2002, Role of a Variable Meridional Flow in the Secular Evolution of the Sun's Polar Fields and Open Flux, ApJ, 577, L53–L57

Zhao, X., Hoeksema, J. T., 1994, A coronal magnetic field model with horizontal volume and sheet currents, Sol. Phys., 151, 91–105

Zhao, X., Hoeksema, J. T., 1995, Prediction of the interplanetary magnetic field strength, J. Geophys. Res., 100, 19–33

Acknowledgements

Die vorliegende Arbeit wurde am Max-Planck-Institut für Sonnensystemforschung in Kaltenburg-Lindau angefertigt.

Mein besonderer Dank gilt Herrn Prof. Dr. Sami K. Solanki für die Ermöglichung dieser Arbeit und der Bereitstellung eines sehr interessanten Forschungsthemas.

Bedanken möchte ich mich bei Herrn Prof. Dr. Franz Kneer für die Übernahme der Betreuung seitens der Universität Göttingen.

Weiter gilt mein besonderer Dank den Herren Prof. Dr. Manfred Schüssler und Dr. habil. Dieter Schmitt für die große Unterstützung, Geduld und anregenden Diskussionen zu meiner Doktorarbeit.

Mein größter Dank jedoch gilt meinen Eltern welche mich während meines Werdegangs immer größtmöglich unterstützt und beraten haben.

Curriculum Vitae

2. August 1975	geboren in Lauf an der Pegnitz
Eltern	Klaus Baumann Ingrid Baumann, geb. Roth
Staatsbürgerschaft	deutsch

Schulbildung

09/1982 - 07/1986	Grundschule in Eckental-Eschenau
09/1986 - 06/1995	Math.-nat. Zweig am staatlichen Gymnasium in Lauf a.d. Peg.
06/1995	Abschluß Abitur

Wehrersatzdienst

08/1995 - 08/1996	Sonderschule der Blindeninstitutsstiftung in Rückersdorf

Studium

10/1996 - 02/2002	Fachrichtung Physik an der Friedrich-Alexander-Universität Erlangen-Nürnberg
07/1998	Vordiplomprüfung
10/1998 - 03/1999	Fachrichtung Physik an der Universidad de Cantabria Santander / Spanien
10/1999 - 03/2000	Fachrichtung Physik an der Universidad de Coimbra / Portugal
11/2000 - 11/2001	Diplomarbeit am Institut für Theoretische Physik II, Erlangen „Dichteabhängige kinetische Terme in der Skyrme-Kraft”
02/2002	Diplomprüfung
03/2002 - 03/2005	Doktorarbeit ”Magnetic Flux Transport on the Sun”
	Während dieser Zeit Tätigkeit als wissenschaftlicher Mitarbeiter am Max-Planck-Institut für Sonnensystemforschung in Katlenburg-Lindau